

9. SITE 1238¹

Shipboard Scientific Party²

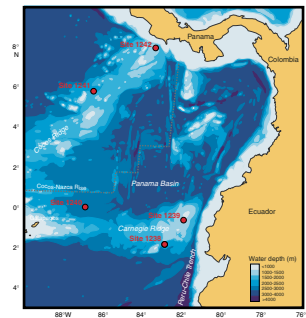
INTRODUCTION

Site 1238 (proposed Site CAR-2C) is located at 1°52.310'S, 82°46.934'W ~200 km off the coast of Ecuador (Fig. F1). On the southern flank of Carnegie Ridge at 2203 m water depth, the site is situated roughly in the middle of a bench that slopes gently to the south (Fig. F2). This portion of Carnegie Ridge is just outboard of the Peru-Chile Trench, where subduction is consuming the volcanic seamounts produced by the Galapagos hotspot (Lonsdale and Klitgord, 1978). From south of Sarmiento Ridge (~7°S), where water depths are >4000 m, the seafloor steps up in a series of southwest-trending ridges and reaches the main scarp of Carnegie Ridge ~20 km north of Site 1238. Basement at Site 1238 likely consists of basalt formed at the Galapagos hotspot at ~11–13 Ma, but it might also be oceanic crust formed at the Galapagos Rift at ~16–18 Ma (Lonsdale and Klitgord, 1978).

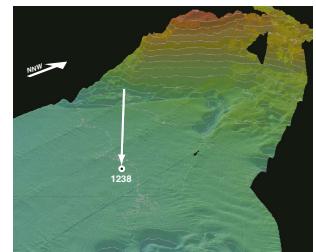
The region of Site 1238 has a relatively uniform pelagic sediment drape of 400–500 m on gently sloping topography. Seismic profiles (Fig. F3) reveal well-stratified sediments on reflective crust. Expected sediments are diatom-nannofossil ooze, with some intervals of diatom ooze (Kemp et al., 1995) and ash layers (Ledbetter, 1985). The steep basaltic flanks of Carnegie Ridge are mostly bare rock, suggesting some downslope transport of sediment (Fig. F2). The southern end of the sedimented ramp reveals rough bathymetry just to the north of a prominent seamount, indicative of erosion, slumping, or other deformation of the sediment column. At the top of the ramp, a disturbed zone, perhaps a detachment feature, is present near the volcanic scarp. These features may suggest that a giant sediment package including the area of Site 1238 was displaced by slumping or creeping downslope.

A tectonic backtrack path on the Nazca plate (Pisias et al., 1995) moves Site 1238 about 600 km westward and slightly to the south relative to a fixed South America (and probably to shallower depths—note

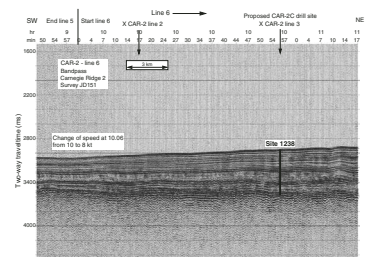
F1. Sites 1238–1242 and regional bathymetry, p. 27.



F2. High-resolution swath bathymetry, p. 28.



F3. Seismic profile at Site 1238, p. 29.



¹Examples of how to reference the whole or part of this volume.
²Shipboard Scientific Party addresses.

possible sea level terraces on the ridge north of Site 1238 in Fig. F2) to a position just south of the Galapagos hotspot ~12 m.y. ago (Fig. F4).

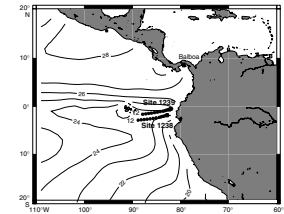
Today, Site 1238 is situated under the eastern reaches of the equatorial cool tongue in an open-ocean upwelling system near the equator (Fig. F5). Nutrient-rich waters of the Equatorial Undercurrent (EUC) surface here and along the coast of Peru and Ecuador (Ocean Climate Laboratory, 1999), and nitrate and phosphate are not fully utilized by the phytoplankton in spite of high production (Fig. F6). Here, a limited supply of micronutrients such as iron, for which the EUC is a major source, may play an important role as a regulator of production (Murray et al., 1994).

The site is likely to record changes in upwelling and biological production, as well as long-term changes in upper-ocean temperature and pycnocline depth. The surface-ocean properties of the eastern equatorial Pacific are sensitive to interannual to decadal oscillations that are strongly controlled by El Niño Southern Oscillations (ENSO) (Cane, 1986) as well as to Pleistocene climate fluctuations (Pisias and Mix, 1997; Mix et al., 1999; Lea et al., 2000; Beaufort et al., 2001). Site 1238's tectonic backtrack to the west is subparallel to the equator, so it is likely that the site resided within the highly productive and climatically sensitive region south of the equator throughout its history.

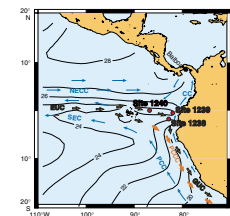
Plate tectonic backtrack locations can be used to predict general features of paleoceanographic change at Site 1238, under the assumptions that the modern overall conditions in the region remain constant through time and that the only change in the system is drift of the site location relative to this fixed oceanographic background (Fig. F7). In this analysis, we ignore changes in the position of the continental margin through time, which may be significant in the region of northern South America and the Central American Isthmus. Sampling of modern oceanographic atlas values at the paleosite locations suggests that from 2 to 3 Ma, sea-surface temperatures at Site 1238 may have been slightly (~1°C) cooler than today, but that at greater ages the site warms gradually as it backtracks across the South Equatorial Current. Salinities increase monotonically at greater ages, as the site backtracks gradually away from the equator and the eastern boundary. Pycnocline depth is relatively stable along the backtrack path, at values of 20–25 m. Sea-surface nutrient concentrations of silicate, phosphate, and nitrate all increase significantly from 0 to 2 Ma but are relatively stable on the Site 1238 backtrack path prior to 2 Ma. In contrast to nutrients, primary productivity is highest within the past 2 m.y. and declines gradually at greater ages as the site backtracks away from the eastern margin. In the absence of other regional changes, we would expect that both biogenic and terrigenous sediment accumulation rates at Site 1238 would be relatively high at younger ages, when the site was located closer to both the eastern boundary and the equator. Significant deviations from these general trends, if detected in the sediment cores, would imply changes in regional oceanographic conditions, or errors in the tectonic backtrack model.

The modern water depth of Site 1238 is ideal to monitor Pacific Central Water (PCW) south of Carnegie Ridge, roughly at the sill depth of the Panama Basin (Tsuchiya and Talley, 1998). The water mass enters the Peru Basin from the west, around the Galapagos platform and through fracture zones in the East Pacific Rise, and is characterized by relatively low oxygen and salinity and high nutrients (Fig. F8). Near the equator, the EUC brings nutrient-rich waters at a few hundred meters depth from the western Pacific to the eastern boundary region, where

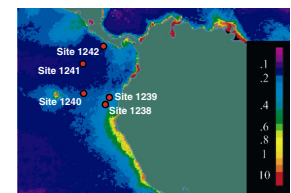
F4. Tectonic backtrack of Site 1238, p. 30.



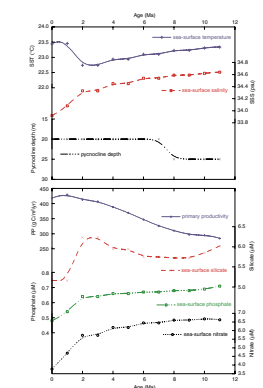
F5. Upper-ocean features off Peru and northern Chile, p. 31.



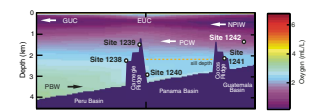
F6. Chlorophyll distributions in surface waters, p. 32.



F7. Modern ocean properties at backtrack locations of Site 1238, p. 33.



F8. Meridional cross section of water masses, p. 34.



they are upwelled to the surface. Oxygen-depleted intermediate waters (remnants of North Pacific Intermediate Water) enter the region from the north at depths of a few hundred to 1000 m, but they are mostly limited to the Northern Hemisphere. In the Southern Hemisphere, remnants of low-salinity Antarctic Intermediate Water are present in the upper 1000 m but are not detected in oxygen concentrations because of strong biological overprints. Below 3 km depth, and thus below the sill depth of the Panama Basin (~2000 m), is Peru Basin Water. This water mass enters the region carrying a weak influence of Circumpolar Deep Water as a relatively low-nutrient, high-oxygen water mass.

The primary objectives at Site 1238 were to provide a continuous sedimentary sequence of Quaternary to Miocene age (as old as ~12–18 Ma) to

1. Assess Neogene history of near-surface water masses, including the eastern reaches of the equatorial cold tongue, upwelling, and paleoproductivity off Ecuador;
2. Monitor temporal and vertical fluctuations of PCW at the sill depth of entry into Panama Basin (shallower sill depth in older interval); and
3. Monitor changes in the occurrence and frequency of volcanic ashes, which might be associated with major uplift phases of the northern Andes.

OPERATIONS

After leaving Peruvian waters, the vessel proceeded to a rendezvous point in the Gulf of Guayaquil, Ecuador, to pick up Juan Carlos Tapia, the Ecuadorian observer, and an Ocean Drilling Program (ODP) engineer, Dean Ferrell. Because of limited accommodations, the Peruvian observer, Robert Herrera, could not remain on the ship. The Bell 206B III helicopter chartered by the Ecuadorian agent had limited range and lacked radar (it used a Global Positioning System receiver for navigation). The vessel was therefore required to divert course and wait on a location no farther than 20 mi from land (south of Salinas; 2.5°S, 81.0°W; 100 m bathymetric contour). The vessel entered Ecuadorian waters at 1515 hr on 4 May 2002 and by 0730 hr on 5 May was positioned 2 mi south of the rendezvous location. The 889-nmi transit required 77.5 hr at an average speed of 11.5 kt. The helicopter landed at 0922 hr and left the *JOIDES Resolution* at 0946 hr.

After a transit of 114 nmi to the west-northwest, the vessel reached Site 1238 (proposed Site CAR-2C) by 2005 hr on 5 May. The 3.5-kHz precision depth recorder (PDR) was used as a final check of site characteristics by comparison to pre-cruise survey data.

Hole 1238A

After the drill string was deployed to a depth of 2209 meters below rig floor (mbrf), Hole 1238A was initiated with the advanced piston corer (APC) at 0150 hr on 6 May. The seafloor depth was estimated at 2213.5 mbrf by the amount of recovery in the first core (3.9 m shallower than the corrected PDR depth). Piston coring advanced to 90.5 meters below seafloor (mbsf), where a stuck core barrel (Core 10H) required drilling over to release the barrel from the sediment. The next piston core barrel came free with an excess force of 60 klb. Cores 12H

through 21H (100.0–195.0 mbsf) had to be drilled over. Piston coring in the hole was terminated when the last piston Core 22H (195.0–204.5 mbsf) did not achieve a full stroke. The cores were oriented starting with 3H. Downhole temperature measurements were taken with the APC temperature (APCT) tool as listed in Table T1. Most of the cores were odoriferous (H₂S) and were stored on the catwalk rack after splitting to degas, which reduced the smell of H₂S in the laboratory stack. Headspace measurements on the cores yielded trace amounts of methane (<100 ppm) and ethane (<3 ppm). No higher hydrocarbon compounds were detected. The nonmagnetic core barrel was deployed on even-numbered cores (Table T1). The APC cored 204.5 m and recovered 211.7 m (recovery = 103.5%).

The hole was deepened with the extended core barrel (XCB) from 204.5 to 430.6 mbsf, where refusal was encountered when the last core (Core 46X) required 105 min to advance 7.7 m in a chert and chalk sequence. The XCB cored 226.1 m and recovered 198.1 m (87.6% of the interval). The total recovery for the hole was 409.8 m (recovery = 95.2%) (Table T1).

Logging

The hole was flushed with 30 bbl of sepiolite mud and then displaced with 200 bbl of 8.9-lb/gal sepiolite mud in preparation for logging. The bit was placed at the logging depth of 99.4 mbsf, and logging began at 0100 hr on 8 May. The triple combination (triple combo) tool string with the Lamont-Doherty Earth Observatory (LDEO) Multi-Sensor Spectral Gamma Ray Tool (MGT) on top was deployed first and then followed by the Formation MicroScanner (FMS)-sonic tool string. One pass with the triple combo was conducted from total depth (429 mbsf) to the mudline, followed by one full pass from 430 mbsf to the bit and one repeat pass from 167 mbsf to the seafloor with the LDEO MGT. The two subsequent passes with the FMS-sonic tool string also reached the bottom of the hole. Hole conditions were unusually smooth, and the hole diameter ranged in size from 11.5 to 14.5 in (29–37 cm). The General Purpose Inclinator Tool (GPIT) accelerometer logs showed increasing deviation from vertical in the hole below 170 mbsf, reaching 6.5° at the base.

All tools gave excellent results because of the good hole conditions. Logging was completed by 1945 hr on 8 May, and the bit was pulled free of the seafloor at 1940 hr on 8 May.

Hole 1238B

The vessel was offset 10 m east of Hole 1238A. Prior to coring, a bottom water temperature measurement was obtained with the APCT tool with the bit positioned just above the seafloor. All temperature measurements combined at this site indicated a high thermal gradient of ~12.7°C/100 m. To obtain the desired stratigraphic overlap with the first hole, the bit was then situated at 2212.0 mbrf, and Hole 1238B was initiated with the APC at 2103 hr. The core barrel was full and, consequently, the seafloor depth from the previous hole was applied to this hole (2213.5 mbrf). Piston coring deepened the hole to 201.0 mbsf. The interval 46.0–49.0 mbsf was drilled to optimize recovery of cores by offsetting with those recovered in Hole 1238A. A total of 198.0 m was cored and 209.5 m was recovered (recovery = 105.8%) (Table T1). The core barrels containing Cores 9H, 14H, 15H, and 17H through 21H

T1. Operations summary, Site 1238, p. 76.

were drilled over (see also Table T3, p. 144, in the “Leg 202 Summary” chapter). The nonmagnetic core barrel was deployed on odd-numbered cores (Table T1). The nonmagnetic core barrel was not used after this to prevent possible damage to hardware as a consequence of the drilling-over process. The cores were oriented starting with Core 3H. The bit was pulled free of the seafloor at 1605 hr on 9 May.

Hole 1238C

The vessel was moved 10 m east, and Hole 1238C initiated with the APC at 1647 hr on 9 May. The bit was positioned at a depth of 2206 mbrf. The seafloor depth calculated from the recovery of the mudline core was 2214.5 mbrf. Piston coring deepened the hole to 162.5 mbsf to ensure the recovery of a complete stratigraphic section. Two intervals were drilled without coring to maintain the proper overlap with data from the previous two holes (39.0–42.0 and 108–110.5 mbsf). Cores were oriented starting with Core 4H. The nonmagnetic core barrel was deployed on even-numbered cores up to Core 14H. Three stuck core barrels had to be drilled over (Cores 15H, 17H, and 18H). The cored interval was 162.5 m, with 167.9 m recovered (recovery = 103.3%) (Table T1).

The vessel was secured for the transit and left location at 1200 hr on 10 May.

COMPOSITE SECTION

We built a meters composite depth (mcd) scale to Section 202-1238A-46X-1 (0.00–466.97 mcd) and a splice (as defined in “Composite Section,” p. 4, in the “Explanatory Notes” chapter) that documents complete recovery for the upper 225.52 mcd. The splice ranges from the top of Core 202-1238B-1H to the bottom of Section 202-1238B-22H-7 (0.00–225.52 mcd) (Tables T2, T3). All APC cores can be correlated to the splice at Site 1238.

The mcd scale and the splice are based on the stratigraphic correlation of whole-core Oregon State University Fast Track magnetic susceptibility measurements (OSUS-MS) collected at 5-cm intervals with a 10-s integration (Fig. F9; Tables T4, T5, T6). Tie points (Table T3) were then used to construct representative spliced records for multisensor track magnetic susceptibility (MST-MS), gamma ray attenuation (GRA) bulk density, natural gamma radiation (NGR) (Fig. F10), and color reflectance (L^* , a^* , and b^*) data (Fig. F11). Magnetic susceptibility was the most useful tool for stratigraphic correlation.

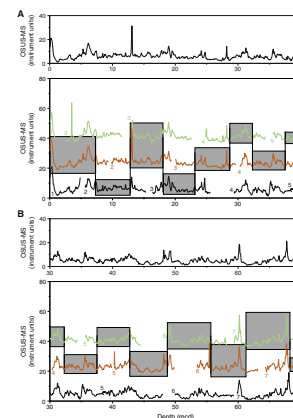
We assumed that the uppermost sediment (the “mudline”) in Core 202-1238B-1H was the sediment/water interface. A mudline was recovered in all three holes and this helped to confirm the fidelity of the top of the recovered section. Core 202-1238B-1H, the “anchor” in the composite depth scale, is the only core with depths that are the same on the mbsf and mcd scales. From this anchor we worked downhole, correlating records on a core-by-core basis.

A comparison of the mcd and mbsf depth scales (Fig. F12) shows that the mcd scale is on average 10% longer than the mbsf scale. Because the growth factor of 1.10 in the APC interval was constant and there were no obvious lithologic changes in the recovered section, we decided to place the XCB cores on an mcd scale by assuming a growth factor of 1.10 applies to the XCB cores from Hole 1238A (Fig. F12).

T2. Composite depth scale, p. 78.

T3. Splice tie points, p. 80.

F9. OSUS-MS vs. mcd, p. 35.

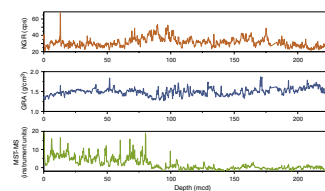


T4. OSUS-MS measurements, Hole 1238A, p. 81.

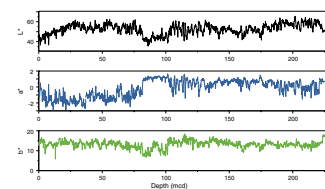
T5. OSUS-MS measurements, Hole 1238B, p. 82.

T6. OSUS-MS measurements, Hole 1238C p. 83.

F10. Smoothed spliced records of NGR, GRA density, and MST-MS, p. 41.



F11. Smoothed spliced records of L^* , a^* , and b^* , p. 42.



In order to facilitate the calculation of mass accumulation rates (MARs), we provide corrected meters composite depth (cmcd) in Table T2 and in Table T3 for depths within the composite section.

Logging operations at Site 1238 produced records of borehole density and natural gamma radiation that could be correlated to GRA density and NGR measurements in sediments from Hole 1238A (Fig. F13). An equivalent log depth (eld) (see “Composite Section,” p. 4, in the “Explanatory Notes” chapter) scale was produced using these correlations. This scale accounts for differential stretching and squeezing within cores as well as for the gaps between cores and is the most accurate depth scale for sediments below the spliced section and above Core 202-1238A-42X (225.52–422.13 mcd), where core recovery falls significantly. The Site 1238 eld file (see the “Supplementary Material” contents list) allows the application of the eld scale to sample depths in either the mbsf or mcd scale using the Sagan software package available from the Borehole Research Group at LDEO.

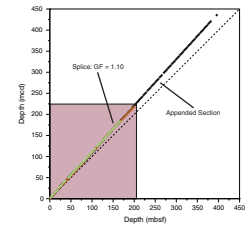
LITHOSTRATIGRAPHY

A 424.7-m-thick (467.3 mcd) sediment sequence dating back to the middle Miocene (~11 Ma) was recovered from three holes at Site 1238. One lithologic unit divided into two subunits was defined at Site 1238 (Fig. F14). Subunit IA spans the upper ~400 m of the sequence and primarily contains bioturbated nannofossil ooze, diatom nannofossil ooze, and nannofossil diatom ooze with varying abundance of clay and foraminifers (Fig. F15). Intervals of distinct light and dark banding on a meter scale are present throughout this subunit. Several ash layers are present within the upper ~300 m, including the regionally correlative ash layer L (230 ka) (Bowles et al., 1973; Ninkovich and Shackleton, 1975). Magnetic susceptibility is highly variable from ~0 to 80 mcd (Pleistocene and uppermost Pliocene). A gradual downhole decrease accompanied by lower-amplitude variability at depths from ~80 to 105 mcd and low values from ~105 to 400 mcd may be associated with decreased terrigenous input, increased biogenic input, or diagenetic dissolution of magnetic minerals deposited prior to the large Pleistocene glacial events.

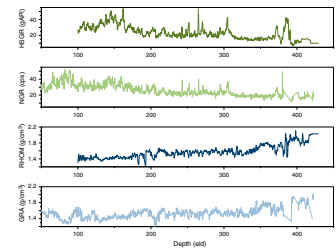
Subunit IB occupies the base of the sequence (~400–467 mcd) and is characterized by increased lithification and diagenesis. This subunit contains partially lithified diatom and nannofossil oozes interbedded with chalk and occasional chert horizons. The presence of chert and micrite indicates significant opal and carbonate diagenesis, respectively. Magnetic susceptibility increases downhole in Subunit IB toward basaltic basement. Increasing lithification is shown by increasing bulk density and decreasing porosity near the top of the subunit.

Overall, the alternating diatom and nannofossil ooze lithologies at this site reflect a moderate- to high-productivity pelagic setting. Evidence from total organic carbon (TOC) measurements, estimates of MAR, and the abundance of organic pigments indicate an interval of relatively high productivity from ~2 to 8 Ma as compared to the Pleistocene interval. Orbital-scale variability in this sequence is evidenced by rhythmic meter-scale light/dark banding in the sediment and preliminary time series analysis of magnetic susceptibility, GRA bulk density, and lightness measurements.

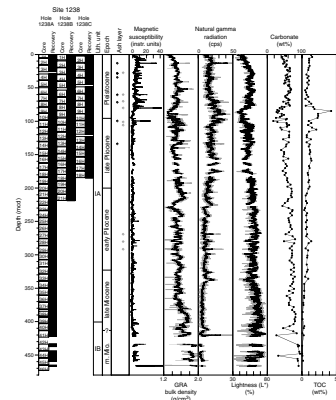
F12. A comparison of the mbsf and mcd scales, p. 43.



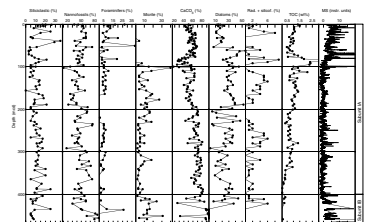
F13. A comparison of logging and core data, p. 44.



F14. Lithostratigraphic summary, Site 1238, p. 45.



F15. Major components, Hole 1238A, p. 46.



Description of Lithologic Unit

Unit I

Intervals: Cores 202-1238A-1H through 46X; Cores 202-1238B-1H through 21H; and Cores 202-1238C-1H through 18H
 Depths: 0.0–467.3 mcd; Hole 1238A: 0.0–424.7 mbsf; Hole 1238B: 0.0–201.5 mbsf; and Hole 1238C: 0.0–168.0 mbsf
 Age: Holocene to late Miocene (0 to <12 Ma)

A single lithologic unit, Unit I, is defined and divided into two subunits (Table T7) on the basis of visual core description, smear slide analysis, thin section examination, color reflectance, X-ray diffraction (XRD) analysis, NGR, moisture and density (MAD), and GRA bulk density measurements. Subunit IA contains interbedded nannofossil ooze, diatom nannofossil ooze, and lesser amounts of diatom ooze. Subunit IB is characterized by significant lithification and diagenetic alteration of biogenic oozes that, prior to diagenesis, were probably similar to those that are present in Subunit IA.

Subunit IA

Intervals: Cores 202-1238A-1H through 39X; Cores 202-1238B-1H through 21H; and Cores 202-1238C-1H through 18H
 Depths: 0.0–402.4 mcd; Hole 1238A: 0.0–365.5 mbsf; Hole 1238B: 0.0–201.5 mbsf; and Hole 1238C: 0.0–168.0 mbsf
 Age: Holocene to late Miocene (0 to ~7 Ma)

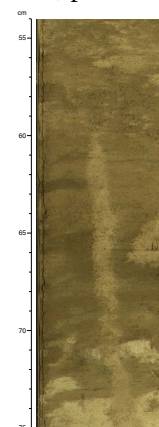
Subunit IA contains interbedded nannofossil and diatom oozes. Minor components include foraminifers, radiolarians, silicoflagellates, clay, micrite, and pyrite. The sediment color varies gradationally between olive, olive gray, light olive gray, and light gray. Mottling, color banding, and burrow traces, particularly *Zoophycos*, are common to pervasive (Fig. F16). Hydrogen sulfide gas was released when the cores were split. Small horizontal fissures caused by degassing are present throughout the three holes. Several ash layers are present in the upper ~300 m of this subunit (Table T8; Fig. F14).

The major lithologies of Subunit IA are nannofossil ooze, diatom nannofossil ooze, and diatom ooze. Transitions between nannofossil and diatom-rich oozes occur on a meter to decimeter scale. Several intervals of rhythmic meter-scale banding between light nannofossil-rich and dark diatom-rich sediment are present throughout Subunit IA (Fig. F17A). Physical properties measurements within these intervals also show the same meter-scale cyclicity (Fig. F17B).

The biogenic oozes in Subunit IA contain varying proportions of calcareous nannofossils, diatoms, foraminifers, radiolarians, silicoflagellates, micrite, and siliciclastic components. Nannofossil abundance ranges from ~10% to 75% in Subunit IA, with a pronounced minimum at 100 mcd that is accompanied by lower carbonate contents (Fig. F15). A generally increasing trend in nannofossil abundance from ~100 to 400 mcd coincides with a gradual increase in CaCO₃. Diatom abundances range from ~15% to 20% in the upper 50 m and then approaches a broad maximum of 30%–50% between 50 and 200 mcd. Below ~200 mcd, diatom abundance becomes more variable, with generally lower values (Fig. F15). Foraminifers are more abundant in the upper ~100 m, approaching maximum values of ~40%. At depths >100 mcd, foraminifer abundance decreases. Radiolarians and silico-

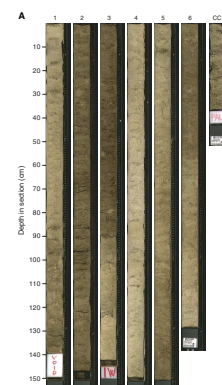
T7. Lithologic Unit I, p. 84.

F16. Vertical burrow from bioturbated interval, p. 47.



T8. Ash layers, p. 85.

F17. Dark and light banding showing meter-scale cyclicity, p. 48.



flagellates are present in amounts of a few percent throughout most of Subunit IA.

Siliciclastic content is highly variable and primarily fluctuates around ~10% throughout Subunit IA (Fig. F15). Clay minerals constitute ~90%–100% of the siliciclastic fraction. Small amounts of feldspars, amphiboles, mica, and pyroxenes are present throughout the subunit. Authigenic components include micrite and pyrite. Micrite-rich intervals (~95–110 and ~155–190 mcd) are often associated with lower nannofossil abundance (Fig. F15). Pyrite is present in minor abundances (up to 5%) throughout the subunit, typically as infill in diatoms and foraminifer tests.

Seventeen ash layers were found in Subunit IA, ten of which are correlative between holes (Table T8; Fig. F14). The ash layers in this subunit range in thickness from 1 to 20 cm and are typically light to dark gray with sharp basal contacts and diffuse upper contacts (Fig. F18). Ash patches often appear just below the ash layers, suggesting bioturbation, although some reworked features may have resulted from the coring and splitting process. The ash layers are composed mainly of silt- to sand-sized clear volcanic glass shards, including unaltered platy and vesicular glass, and, less commonly, palagonite. The most common associated mineralogical components include feldspars, biotite, hornblende, pyroxenes, and pyrite, indicating an andesitic source. Minor amounts (0%–4%) of volcanic glass are also disseminated throughout the sediment of this subunit.

Magnetic susceptibility is relatively high, with larger-amplitude variations from ~0 to 100 mcd. Lower volumes and lower-amplitude variations mark the interval from ~100 to 400 mcd (Fig. F14). GRA and MAD bulk densities are well correlated to each other ($r^2 = 0.85$) (Fig. F19). An increase in bulk density from ~0 to 30 mcd is accompanied by a decrease in porosity that is likely related to compaction, dehydration, and increasing carbonate contents (Figs. F14, F19).

In the a^* - b^* color space, all color measurements at Site 1238 plot in the “yellow” ($b^* > 0$) domain (Fig. F20). The relatively carbonate-poor interval from ~80 to 102 mcd, which has low lightness values (Fig. F16), still lies in the “yellow” domain but is shifted in the a^* - b^* space to values of $a^* > 0$ (Fig. F20). The sediment hue in this subunit is extremely homogeneous (i.e., the ratio of a^* to b^* is constant). Predictive relationships between color reflectance (a^* , b^* , and L^*) and carbonate and TOC via multiple linear regression are relatively weak (i.e., $r^2 = \sim 0.6$ for each component), reflecting the complexity of the sediment matrix that contains biogenic silica and other chromophores.

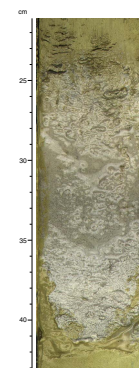
Organic pigment absorption features are detectable at 410, 510, 560, and 650 nm in reflectance spectra for sediment of the lower part of Subunit IA (~100–400 mcd). The strongest absorption feature at 650 nm, which is due to chlorins (i.e., chlorophyll-related pigments), persists throughout the sediment column and is most pronounced between ~75 and 200 mcd (Fig. F21).

Subunit IB

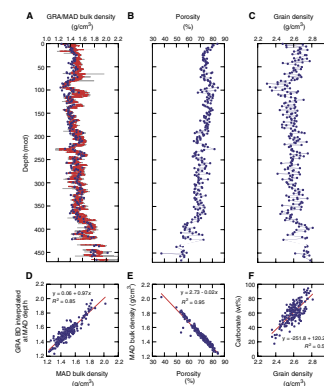
Interval: Cores 202-1238A-40X through 46X
Depths: 402.4–467.3 mcd and 365.5–424.7 mbsf
Age: late Miocene to middle Miocene (~7 to <12 Ma)

Subunit IB contains upper to middle Miocene partially lithified biogenic oozes interbedded with chalk and chert. The sediment color ranges

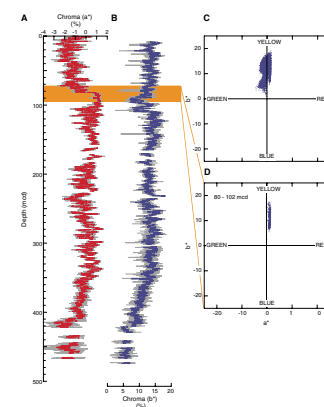
F18. Proposed ash layer L, p. 50.



F19. Physical properties measurements, Site 1238, p. 51.



F20. Color measurements, Site 1238, p. 52.



from light gray to white with occasional light-green and purplish gray bands.

The dominant lithologies of Subunit IB are diatom-bearing nannofossil ooze, nannofossil diatom ooze with micrite, and nannofossil ooze (Table T7). Diatoms, radiolarians, and silicoflagellates are relatively abundant within the upper half of Subunit IB and disappear below ~430 mcd. The lower part of the subunit is dominated by nannofossils (up to ~80%). Micrite abundance is generally higher than in the overlying subunit and fluctuates between ~10% and 30% (Fig. F15).

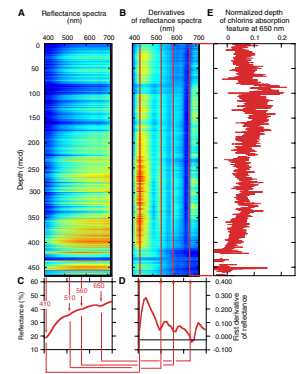
Minor lithologies in Subunit IB include chalk and chert. The first occurrence of chalk (Fig. F22A) is at ~430 mcd, coincident with the disappearance of siliceous microfossils. Thin sections of the chalk show abundant foraminifers, many of which are pyritized. Nannofossils are rare to absent, and radiolarians and diatoms are present. Chalcedony is also observed in the thin sections, often as infill associated with foraminifer tests. XRD analysis of the chalk from Sample 202-1238-42X-1, 23–24 cm, shows a high calcite content (~80%–90%) with smaller trydimite (opal-CT) and quartz peaks (Fig. F22B). The quartz peak may be associated with the chalcedony, and the trydimite peak suggests a modest contribution from biogenic silica. Distinct chert horizons are present at the base of Subunit IB in Section 202-1238-46X-1 (Fig. F23).

From the top of Subunit IB (~400 mcd), magnetic susceptibility increases downcore toward basaltic basement (Fig. F14). A lithification-related decrease in porosity and an associated increase in bulk and grain density begin at ~430 mcd, where chalk first occurs, and persist throughout the remainder of Subunit IB (Fig. F19).

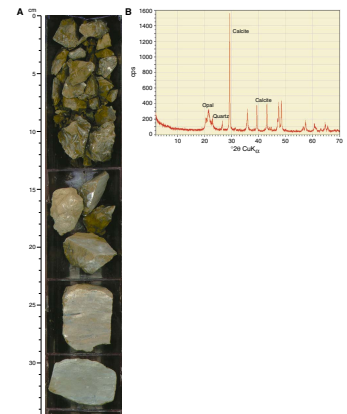
Interpretation and Depositional History

Site 1238 lies within an active upwelling zone and is characterized by rapidly accumulating nannofossil and diatom oozes. Changes in upwelling and the supply of nutrients, as well as carbonate dissolution, may be reflected in the varying predominance of siliceous vs. calcareous primary producers throughout Subunit 1A. In general, siliceous microfossils and organic carbon concentrations increase from ~8 to 1 Ma, whereas carbonate concentrations decrease. Mass accumulation rates of biogenic components display a maximum between ~6.5 and 3.5 Ma, suggesting a phase of high productivity from the late Miocene to mid-Pliocene (see “Age Model and Mass Accumulation Rates,” p. 23). The influence of siliceous sediment deposition increases, especially after 4 Ma, culminating in a maximum between ~2 and 1 Ma, an interval that again is marked by increased mass accumulation rates in biogenic components. A significant change in sediment deposition accompanies the mid-Pleistocene climate deterioration at ~1 Ma. The interval of the last 1 m.y. is marked by low MARs associated with a strong decrease in siliceous microfossil and organic carbon concentrations and an increase in carbonate contents. This inference of high productivity, based on the abundance of siliceous sediments, is consistent with organic carbon driving sulfate reduction, which occurs throughout the upper ~400 m of this sequence, but never to completion (see “Geochemistry,” p. 17). The sediments offer no evidence for episodes of anoxia, based on the continuous presence of burrows and other bioturbation features. The long-term evolution in biogenic productivity does not reflect the predicted changes in productivity that may result from the eastward paleodrift of Site 1238 toward the coastal upwelling region off Ecuador (see “Introduction,” p. 1). The paleodrift of Site 1238 toward its modern lo-

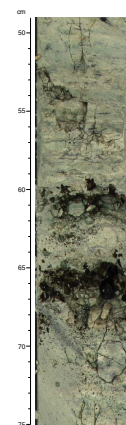
F21. Sequential depth plots and derivatives, Site 1238, p. 53.



F22. Photo and XRD plot of chalk, p. 54.



F23. Chalk interbedded with chert horizons, p. 55.



cation would suggest an increase in productivity over the last 10 m.y. Thus, the documented variability in productivity may reflect changes in upwelling and nutrients that are driven by changes in oceanography rather than resulting from plate tectonic movement of the site location.

Preservation of carbonate and siliceous microfossils remains good for the majority of this interval. Persistent mottling, gradational color transitions, abundant burrows, and *Zoophycos* traces all indicate vigorous bioturbation associated with a robust benthic ecosystem supported by generally high organic carbon flux to the seafloor.

Magnetic susceptibility changes from a baseline with negligible values and little change (0 ± 2 instrument units) in the Pliocene interval to increasingly higher values (~ 5 – 10 instrument units) and larger-amplitude variability in the Pleistocene interval (Fig. F14). This shift begins at ~ 90 mcd and continues through the upper Pleistocene sediment sequence, suggesting a possible link to the intensification of the mid-Pleistocene global glaciation, which is marked by the onset of predominant 100-k.y. climate cycles.

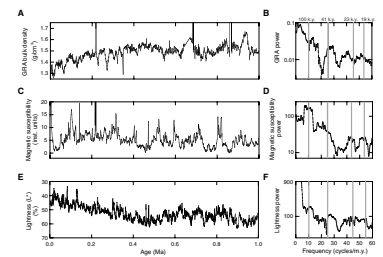
Time series analysis on magnetic susceptibility, GRA bulk density, and lightness measurements for the uppermost portion (0.0–58.2 mcd) of the sequence at Site 1238 (representing ~ 0 – 1 Ma) using a preliminary biostratigraphic age model shows significant power in and around orbital frequency bands associated with eccentricity, obliquity, and precession (Fig. F24) and thus may be related to glacial-interglacial changes in the relative supplies of biogenic and terrigenous material. These preliminary results are based on linear sedimentation rates (LSRs) interpolated between limited biostratigraphic datums and warrant further analysis once better age control is established.

Higher susceptibility values in the uppermost portion of this sequence may be explained by increased input of fine-grained magnetic minerals associated with a terrigenous component, because small changes in terrigenous content would be proportionally significant in the biogenically dominated sediment of Subunit IA. Decreased input of biogenic material in this interval would also result in higher magnetic susceptibility. Based on preliminary biostratigraphic estimates across this interval, there is no evidence for a significant change in sedimentation rate that would accompany increased terrigenous or biogenic input. Another possible explanation for this change is related to the abundance and dissolution of magnetic minerals. Diagenetic dissolution of magnetic minerals below this interval, related to a higher concentration of TOC and therefore a more reducing sedimentary environment, would yield lower magnetic susceptibility at depths below ~ 90 – 100 mcd.

Although variations in the bulk density are largely controlled by carbonate content at this site, the average bulk density in Subunit IA is lower than at previous sites (e.g., by ~ 0.2 g/cm³ relative to Site 1236, where carbonate was present in a proportion $>95\%$). Porosity in this subunit is also significantly higher than at previous sites (i.e., by $\sim 10\%$ relative to Site 1236, which contained abundant calcium carbonate). The relatively high proportion of biogenic silica at Site 1238 is likely responsible for both the density and porosity differences. Biogenic silica, which has a grain density of 2.0 g/cm³ (diatoms), has a rigid, open structure that tends to keep pore spaces open (Silva et al., 1976).

Volcanic ash deposition began in the late Miocene at Site 1238 and increased in frequency during the last 2 m.y. The accessory mineral composition of ashes at Site 1238 suggests an andesitic volcanic source, most likely from explosive eruptions in northern South America, Cen-

F24. Time series analysis results based on biostratigraphic age model, p. 56.



tral America, and southern Mexico (Ledbetter, 1985). An ash layer containing 80%–90% clear, platy glass with feldspars, hornblende, biotite, and pyroxene, which we infer to be the ash layer L of Bowles et al. (1973) and Ninkovich and Shackleton (1975), is present at 13.15 mcd in this sequence. Based on its distribution in eastern tropical Pacific marine sediments, Ninkovich and Shackleton (1975) hypothesized a volcanic source in northern South America for this ash layer. This ash is observed in all three holes and is consistently 15–20 cm thick at this site (Fig. F17), which is thicker than any other ash layer L deposits recorded in the eastern tropical Pacific from 10°S to 5°N (Ninkovich and Shackleton, 1975). The age of ash layer L is ~230 ka (Ninkovich and Shackleton, 1975), suggesting a late Pleistocene sedimentation rate of 5–6 cm/k.y., which is consistent with the preliminary age model (see “Age Model and Mass Accumulation Rates,” p. 23) at this site.

Postdepositional Diagenesis

The presence of partially to completely lithified biogenic material and the increase in authigenic components such as micrite and chalcedony at the base of the sequence recovered at Site 1238 suggests significant postdepositional diagenetic alteration. Recrystallized calcium carbonate in the form of micrite is present at Site 1238 from ~100 mcd to the base of the sequence. Micrite is typically observed in association with the nannofossils that are the major constituents of the oozes at this site. The abundance of micrite increases during periods of diminished nannofossil and increased siliceous microfossil abundances. An increase in productivity, as suggested by higher TOC and biogenic silica (diatom abundance), likely results in dissolution of biogenic calcite and subsequent authigenic precipitation, which is consistent with pore water alkalinity and calcium profiles (see “Interstitial Water Geochemistry,” p. 18, in “Geochemistry”).

Light green and purplish gray banding and mottling in Subunit IB are present from ~430 mcd to the base of the sequence. Pyrite abundance within this interval ranged from ~2% to 4%. Previously described similar color banding in carbonate oozes on the Ontong Java Plateau (ODP Leg 130) was associated with Fe-bearing clays, some of which contained Fe sulfides, such as pyrite, depending on local redox conditions (Lind et al., 1993).

At the base of this sequence (~400–470 mcd), the presence of chert and chalcedony provides significant evidence for opal diagenesis. The dissolution of biogenic silica occurs throughout the sequence, but recrystallization is greater at depth, perhaps as a result of warmer ambient temperatures here (see “Geochemistry,” p. 17). Below ~430 mcd, the sediment is depleted in biogenic silica but contains chalcedony infill and discrete chert nodules. The chalcedony- and chert-bearing intervals correspond to a large decrease in pore water silicate (see “Geochemistry,” p. 17), which suggests complete dissolution of siliceous microfossils and subsequent migration of dissolved silica in the pore water to sites of reprecipitation. If the thermal gradient remains constant, this diagenetic boundary will likely remain fixed relative to the seafloor but will migrate upward from basement as more sediment is deposited.

BIOSTRATIGRAPHY

The 420-m-thick interval recovered at Site 1238 includes Quaternary–middle Miocene sediments. A well-constrained biostratigraphy is provided by the various microfossil groups (Table T9; Fig. F43). The section comprises a continuous 350-m-thick expanded sequence from the Pleistocene–uppermost Miocene (to ~6.6 Ma) and a ~75-m-thick condensed upper–middle Miocene sequence. A Miocene nannofossil assemblage, which includes *Coccolithus miopelagicus* and the absence of *Cycli-cargolithus floridanus* in the deepest sample (202-1238A-46X-CC), suggests a basal age of 10.4–11.6 Ma. Planktonic foraminifers suggest a basal age of 11.68–13.18 Ma. This would result in extremely low sedimentation rates or a hiatus in the lowermost interval below ~420 mcd.

Calcareous nannofossils are generally abundant throughout the section, with good to moderate preservation except in the lower Pleistocene and middle Miocene (Cores 202-1238A-11H and 45X, respectively), in which nannofossils are rare and calcium carbonate contents are low (Fig. F25).

Planktonic and benthic foraminifers are common to abundant, except in two intervals (90–160 mcd and 330–460 mcd) where abundance decreases markedly. In contrast, radiolarians are abundant in these intervals. Preservation of foraminifers is good to moderate, except in the lower part of Hole 1238A. Benthic/planktonic foraminifer ratios generally increase downhole with ~1% benthic foraminifers down to 100 mcd, ~20% between 100 and 330 mcd, and ~50% or more below 330 mcd (Fig. F25).

Diatoms are common to abundant throughout the Pleistocene, Pliocene, and the upper half of the upper Miocene (~8–9 m.y.) (Fig. F25). Below Core 202-1238A-42X (~430 mcd), the lower half of the upper Miocene is barren of siliceous microfossils, except for rare fragments replaced by pyrite within the siliceous chalk in Cores 42X and 43X (~430–440 mcd).

Calcareous Nannofossils

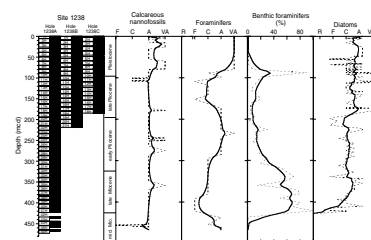
Calcareous nannofossils are abundant and well to moderately preserved in all the samples examined (Table T10). Minor to moderate dissolution of nannofossils is evident where siliceous microfossils are highly abundant. Overgrowths on nannofossils are only minor. Presumably because of the high abundance of the siliceous microfossils, some traditional index nannofossil species, particularly some discoaster and ceratolith species, are rare or absent. However, discoaster abundance varies, probably indicating significant fluctuations in upwelling intensity.

The generally low abundance or the absence of some index species and the frequent reworking of nannofossils in the upper upper Miocene–lower Pliocene compromised the stratigraphic resolution to some extent. Nevertheless, a moderate-resolution nannofossil biostratigraphy has been established for the entire section. Nannofossil biostratigraphy suggests that the section spans a time interval from 0 to ~11 Ma and that the sequence is complete without any detectable hiatuses or sediment slumps.

Virtually all the well-known Pleistocene nannofossil events have been located within an uncertainty of ~1.5 m. These events are the beginning of the acme of *Emiliana huxleyi* (0.08 Ma), between Samples

T9. Age-depth control points, p. 86.

F25. Calcareous nannofossils, benthic foraminifers, and diatoms, p. 57.



T10. Distribution of calcareous nannofossils, p. 88.

202-1238A-1H-2, 75 cm (2.25 mcd), and 1H-3, 75 cm (3.75 mcd); the first occurrence (FO) of *E. huxleyi* (0.26 Ma), between Samples 2H-4, 75 cm (10.88 mcd), and 2H-5, 75 cm (12.39 mcd); the last occurrence (LO) of *Pseudoemiliania lacunosa* (0.46 Ma), between Samples 3H-CC, 14 cm (25.86 mcd), and 4H-1, 75 cm (30.05 mcd); the LO of *Reticulofenestra asanoi* (0.88 Ma), between Samples 6H-1, 75 cm (50.6 mcd), and 6H-2, 75 cm (52.11 mcd); the FO of *R. asanoi* (1.08 Ma), between Samples 7H-5, 75 cm (66.58 mcd), and 7H-6, 75 cm (68.09 mcd); the LO of large *Gephyrocapsa* spp. (1.24 Ma), between Samples 7H-6, 75 cm (68.09 mcd), and 7H-CC, 1 cm (68.95 mcd); the FO of large *Gephyrocapsa* spp. (1.45 Ma), between Samples 8H-5, 75 cm (76.79 mcd), and 8H-6, 75 cm (78.3 mcd); the LO of *Calcidiscus macintyreii* (1.59 Ma), between Samples 9H-3, 75 cm (81.68 mcd), and 9H-4, 75 cm (83.19 mcd); and the FO of medium *Gephyrocapsa* spp. (1.67 Ma), between Samples 11H-1, 75 cm (99.65 mcd), and 11H-2, 75 cm (101.2 mcd).

The youngest Pliocene nannofossil datum, the LO of *Discoaster brouweri* (1.96 Ma), is difficult to place precisely because of some reworking of the species into the Pleistocene. It is tentatively placed here between Samples 202-1238A-11H-6, 75 cm (107.2 mcd), and 11H-7, 40 cm (108.3 mcd), based mainly on the higher abundance of the species from the latter sample downhole. The LO of *Discoaster pentaradiatus* (2.44 Ma), between Samples 202-1238A-13H-3, 75 cm (124 mcd), and 13H-4, 75 cm (125.5 mcd), and the LO of *Discoaster surculus* (2.61 Ma), between Samples 13H-5, 75 cm (127 mcd), and 13H-6, 75 cm (128.6 mcd), also have some small uncertainties because of the relatively low abundance of discoasters in this part of the section. The LO of *Reticulofenestra pseudoumbilicus* (3.8 Ma) is placed between Samples 202-1238A-20H-CC (204.1 mcd) and 21H-CC (214.5 mbsf) based on the common occurrence of the species from the latter sample downhole. The generally rare presence of the species in a number of samples above this level are considered reworked because *Sphenolithus abies* is also very rare and *P. lacunosa* is found as deep as Sample 202-1238A-21H-CC.

The youngest Miocene datum, the LO of *Discoaster quinqueramus* (5.56 Ma), could not be determined at this site because of persistent reworking of nannofossils in the upper Miocene. This reworking problem can be seen by the presence of *Ceratolithus* sp. with *D. quinqueramus* in several samples in Cores 202-1238A-23X and 24X. The FO of the *Ceratolithus* genus is known to be at 5.0 Ma, and thus, the two species should not be present together. On the other hand, the very rare and sporadic *Ceratolithus* sp. does not allow a reliable use of its FO as a datum at the site.

A reliable late Miocene datum, the top of the *R. pseudoumbilicus* (>7 μm) absence interval (6.8 Ma), is located between Samples 202-1238A-38X-3, 75 cm (385.62 mcd), and 38X-6, 75 cm (390.2 mcd). The bottom of the *R. pseudoumbilicus* (>7 μm) absence interval (8.85 Ma) is placed between Samples 202-1238A-41X-4, 75 cm (418.96 mcd), and 41X-5, 75 cm (420.47 mcd). The oldest nannofossil datum determined at the site, the LO of *C. miopelagicus* (10.4 Ma), lies between Samples 202-1238A-45X-1, 75 cm (455.70 mcd), and 45X-2, 75 cm (457.20 mcd). The onset of siliceous sediment at the site at ~9 Ma (within Core 202-1238A-42X) perhaps signals a large change in wind-driven upwelling, caused by major uplift of the Andes or a change in regional oceanic nutrient budgets. The deepest sample (202-1238A-46X-CC) contains a Miocene nannofossil assemblage without *C. floridanus*. The latter species is generally ubiquitous in Miocene sediment older than 11.6 Ma. This suggests a basal age of 10.4–11.6 Ma at the site.

Planktonic Foraminifers

Planktonic foraminifers are generally abundant and well preserved in the upper part of Hole 1238A (mudline to Sample 202-1238A-9H-CC; 0–87.89 mcd). Below this depth, abundance and preservation vary markedly and the relative proportion of radiolarians and benthic foraminifers in the residue generally increases (Table T11; Fig. F25). Abundance decreases and preservation deteriorates significantly, particularly in two intervals between Samples 202-1238A-9H-CC and 15H-CC (87.89–152.15 mcd) and between Samples 37X-CC and 46X-CC (380.99–466.95 mcd). Near the base of Hole 1238A (Samples 202-1238A-43X-CC to 45X-CC; 437.44–466.95 mcd), recrystallized overgrowths frequently obscure test features.

Diversity is quite low overall, and assemblages tend to be dominated by upwelling taxa, such as *Neogloboquadrina dutertrei* or *Neogloboquadrina pachyderma*. Standard marker species are present throughout samples from the upper part of Hole 1238A and can be used to establish a preliminary biostratigraphy for the Pleistocene–Pliocene interval (Cores 202-1238A-1H to 17H; 5.01–173.29 mcd). However, few datums are available between Cores 202-1238A-18H and 41X (183.47–422.17 mcd) to interpret and constrain the biostratigraphy of the lower Pliocene–upper Miocene interval. The foraminiferal assemblage within this interval contains some blackened tests with mud infills that may indicate reworking. Two reliable datums between Samples 202-1238A-41X-CC and 46X-CC (422.17–466.95 mcd) indicate an age between 11.68 and 13.42 Ma for the base of Hole 1238A.

The well-preserved Pleistocene–late Pliocene planktonic foraminiferal assemblage includes *Globigerina bulloides*, *Globigerina quinqueloba*, *Globigerinita glutinata*, *Globigerinoides ruber*, *Globorotalia menardii*, *Globorotalia scitula*, *Globorotalia tumida*, *N. dutertrei*, *N. pachyderma*, *Orbulina universa*, and *Sphaeroidinella dehiscens*. The LO of *G. ruber* (pink) is placed between Samples 202-1238A-1H-CC and 2H-CC (5.01–15.56 mcd), and an age younger than 0.12 Ma can be assigned to the overlying section (upper Pleistocene Subzone Pt1b of Berggren et al., 1995) (Fig. F25; also see Fig. F12, p. 63, in the “Explanatory Notes” chapter). The FO of *G. ruber* pink is recognized between Samples 202-1238A-2H-CC and 3H-CC (15.56–25.86 mcd), and an age between 0.12 and 0.40 Ma is attributed to the interval between the FO and LO of this species. An additional datum for Subzone Pt1b is provided by the FO of *Globorotalia hirsuta* (0.45 Ma) between Samples 202-1238A-3H-CC and 4H-CC (25.86–38.84 mcd).

The boundary between upper Pleistocene Subzone Pt1b and lower Pleistocene Subzone Pt1a is marked by the LO of *Globorotalia tosaensis* (0.65 Ma; Zone Pl5), which can be placed between Samples 202-1238A-4H-CC and 5H-CC (38.84–48.24 mcd). Three other useful datums indicating Subzone Pt1a are the LO of *Globigerinoides obliquus* (1.30 Ma), which is present between Samples 202-1238A-5H-CC and 6H-CC (48.24–59.78 mcd), and the LOs of *Pulleniatina finalis* (1.40 Ma) and *Neogloboquadrina acostaensis* (1.58 Ma), which can be identified between Samples 6H-CC and 7H-CC (59.78–68.95 mcd).

The Pliocene/Pleistocene boundary could not be recognized because of the absence of the standard zonal markers. However, the LO of *P. finalis* (2.04 Ma), between Samples 202-1238A-9H-CC and 10H-CC (87.89–98.20 mcd), indicates upper Pliocene Zone Pl6. The LO of *Globorotalia pseudomiocenica* (2.30 Ma), between Samples 202-1238A-10H-CC and 11H-CC (98.20–108.68 mcd), identifies the boundary be-

T11. Distribution of planktonic foraminifers, p. 90.

tween Zones Pl6 and Pl5. The LO of *Globorotalia margaritae* (3.58 Ma), between Samples 202-1238A-15H-CC and 16H-CC (152.15–162.10 mcd), marks the base of upper Pliocene Zone Pl3. Two useful markers for lower Pliocene Zone Pl2 are the LO of *Pulleniatina primalis* (3.65 Ma) and the LO of *G. margaritae* common (3.96 Ma), between Samples 202-1238A-16H-CC and 17H-CC (162.10–173.29 mcd). The FO of *Globorotalia puncticulata* (4.50 Ma), identified between Samples 202-1238A-28X-CC and 29X-CC (285.26–294.43 mcd), indicates Subzone Pl1b.

The Pliocene/Miocene boundary can be approximated by the FO of *G. margaritae* (6.09 Ma), between Samples 202-1238A-34H-CC and 35H-CC (349.48–359.96 mcd), which indicates uppermost Miocene Zone M14. The LO of *Globorotalia fohsi* s.l. (11.68 Ma), between Samples 202-1238A-41X-CC and 43X-CC (422.17–437.44 mcd), provides some useful age control in the lower part of Hole 1238A and points to much lower sedimentation rates or a hiatus in the lower upper Miocene and upper middle Miocene. The FOs of *G. fohsi* s.l. and *Globorotalia robusta* (13.42 and 13.18 Ma, respectively) cannot be identified, as both taxa are present in the lowermost sample recovered from Hole 1238A (Sample 202-1238A-46X-CC; 466.95 mcd).

Benthic Foraminifers

The abundance and preservation of benthic foraminifers vary markedly in Hole 1238A (Table T11). The percentage of benthic foraminifers relative to total foraminifers is initially low (1% or less between the mudline and Sample 202-1238A-9H-CC; 0–87.89 mcd), then it fluctuates significantly between Cores 10X and 41X (98.20–422.17 mcd), reaching 99% in Sample 41X-CC (422.17 mcd). At depths below 422.17 mcd, benthic foraminifers represent only 1%–3% of the total foraminiferal assemblage. The Pleistocene–late Miocene assemblage is characterized by *Cibicidoides mundulus*, *Globocassidulina subglobosa*, *Globobulimina affinis*, *Globobulimina pyrula*, *Gyroidinoides soldanii*, *Laticarinina pauperata*, *Melonis affinis*, *Melonis pompilioides*, *Oridorsalis umbonatus*, *Planulina wuellerstorfi*, *Pullenia bulloides*, *Pyrgo murrhina*, *Pyrgo serrata*, *Uvigerina peregrina*, and *Vulvulina spinosa*.

Preliminary shipboard studies do not permit us to evaluate whether the changes in benthic foraminiferal abundance reflect variations in test accumulation rates (related to fluctuations in surface productivity) or stem from a preservation bias. However, changes in assemblage composition are apparent (although not quantified during shipboard study), particularly in the relative proportion of high productivity indicators such as *Bulimina*, *Globobulimina*, and *Uvigerina*, which suggest temporal changes in food resources at the seafloor, probably related to shifts in upwelling intensity and circulation patterns.

Diatoms

All core catcher samples from Hole 1238A were analyzed, as well as smear slides of some additional layers from the split cores. Diatom abundance and preservation vary from sample to sample, but diatoms are generally common to abundant (Fig. F25) and moderate to poorly preserved and very fragmented in the samples examined between Cores 202-1238A-1H and 41X. Sample 202-1238A-42X-CC contained chert, and the sequence below Core 43X through the bottom of the hole was barren of diatoms. Diatom assemblages in most samples vary from those dominated by *Thalassiothrix* and *Thalassionema* species to those

dominated by *Azpeitia nodulifer*. Diatoms recovered from Site 1238 represent a continuous stratigraphic interval from the Holocene *Fragilariopsis doliolus* Zone to the late Miocene *Nitzschia porteri* Zone. Diatom biostratigraphy suggests that the sequence is complete with no detectable hiatuses (Table T12). However, the generally low abundance of some index species and the frequent reworking of older diatoms in the lower Pliocene–upper Miocene interval compromises the stratigraphic resolution to some extent and requires much more detailed shore-based work.

The mid-Pleistocene diatom datums, LOs of *Nitzschia reinholdii* (0.62 Ma) and of *N. fossilis* (0.70 Ma), are difficult to place precisely because of the rare and sporadic occurrences of those species. We have recognized the following reliable Pleistocene diatom datums. The LO of *Rhizosolenia matuyamai* (1.05 Ma) is placed between Samples 202-1238A-6H-4, 75 cm, and 6H-4, 100 cm (55.13–55.38 mcd); the FO of *R. matuyamai* (1.18 Ma) is recognized between Samples 202-1238A-7H-4, 75 cm, and 7H-5, 75 cm (65.07–66.58 mcd); the LO *Rhizosolenia praebergonii* var. *robusta* (1.73 Ma) is doubtful but may be placed between Samples 202-1238A-9H-2, 75 cm, and 9H-3, 75 cm (80.16–81.67 mcd); and the FO of *F. doliolus* is probably placed between Samples 202-1238B-11H-CC and 12-1, 75 cm (108.68–109.6 mcd).

The following late Pliocene diatom datums were recognized as follows: The LO of *Thalassiosira convexa* s.l. (2.41 Ma) is placed between Samples 202-1238A-12H-2, 75 cm, and 12H-3, 75 cm (111.11–112.6 mcd). The LO of *Nitzschia jouseae* (2.77 Ma) occurs between Samples 202-1238A-14H-4, 75 cm, and 14H-5, 75 cm (136.23–137.7 mcd). The FO of *R. praebergonii* s.l. (3.17 Ma) is placed between Samples 202-1238A-18H-2, 75 cm, and 18H-3, 75 cm (175.75–177.3 mcd). The FO of *T. convexa* var. *convexa* (3.81 Ma) occurs between Samples 202-1238A-22H-5, 75 cm, and 22H-CC (222.55–225.8 mcd).

The FO of *N. jouseae* (5.12 Ma) was recognized between Samples 202-1238A-29X-3, 75 cm, and 30X-3, 75 cm (290.73–301 mcd). The LO of *Nitzschia cylindrica* (4.88 Ma), is placed between Samples 202-1238A-28X-3, 75 cm, and 29X-3, 75 cm (279.82–290.4 mcd).

For the late Miocene, given the presence of reworked forms, the stratigraphic model is mainly based on FO datums but LOs have also been considered when in accordance with recognized FOs. The LO of *Thalassiosira miocenica* (5.84 Ma) was recognized between Samples 202-1238A-33X-3, 75 cm, and 34X-3, 75 cm (332.87–343.4 mcd). The LO of *Nitzschia miocenica* (6.08 Ma) was placed between Samples 202-1238A-34X-6, 75 cm, and 35X-1, 75 cm (347.95–351). The LO of *Thalassiosira praeconvexa* (6.18 Ma) was tentatively recognized between Samples 202-1238A-35X-CC and 36X-CC (359.76–370.5 mcd). The FO of *T. miocenica* (6.55 Ma) was placed between Samples 202-1238A-36X-CC and 37X-CC (370.29–380.9 mcd). The FO of *T. convexa* (6.57 Ma) is tentatively placed between Samples 202-1238A-36X-CC and 38X-CC (370.29–391.5 mcd). The LO of the *Rossiella praepaleacea* group (6.54 Ma) and the FO of *T. praeconvexa* (6.71 Ma) may be placed between Samples 202-1238A-37X-CC and 38X-CC (380.85–391.5 mcd). The FO of *N. miocenica* (7.30 Ma) is recognized between Samples 202-1238A-38X-CC and 39X-CC (391.51–402.3 mcd). The LO of *Actinocclus ellipticus* var. *javanicus* (7.79 Ma) is probably placed between Samples 202-1238A-40X-CC and 41X-CC (412.85–422.2 mcd).

The siliceous microfossil assemblage from Samples 202-1238A-41X-6, 75 cm, to 41X-CC (421.97–422.17 mcd), is characterized by the presence of the heavily silicified diatom *Coscionodiscus marginatus*, and the

T12. Distribution of diatoms,
p. 92.

common presence of radiolarians. No age diagnostic diatom species have been observed, but the common presence of *C. marginatus* has been previously noted within the *N. porteri* Zone (7.30–8.23 Ma) and the upper portion of the *Coscinodiscus plicatus* Zone (equivalent to *Thalassiosira yabei* Zone; 8.23–9.76 Ma) (see Fig. F12, p. 63, in the “Explanatory Notes” chapter) at Site 495 (Jousé et al., 1982).

PALEOMAGNETISM

Natural Remanent Magnetization

The natural remanent magnetization (NRM) of archive half sections was initially measured and then remeasured after alternating-field (AF) demagnetization at selected levels. Sections obviously affected by drilling disturbance were not measured. Cores 202-1238A-1H through 8H were demagnetized at peak fields of 20 and 25 mT. Cores 202-1238A-9H through 46X and Holes 1238B and 1238C were demagnetized at peak fields of 25 mT.

Initial NRM intensities ranged from 10^{-2} to 10^{-4} A/m (Fig. F26). Below 200 mcd in Hole 1238A, the XCB cores have a low average but highly variable intensities possibly as a result of coring disturbance (Fig. F26). Cyclic variability in NRM intensity within the uppermost 100 mcd (Fig. F26) may at least be partially related to the alternating use of the nonmagnetic and normal steel (magnetic) core barrels (Fig. F27) (see Lund et al., this volume). After AF demagnetization at peak fields of 25 mT (Fig. F26), a one order of magnitude decrease in intensity was observed for the upper 50 mcd that increases to ~1.5 orders of magnitude below. Additionally, both the initial and demagnetized NRM lose ~95% of their initial intensity within the first meter of sediment (Fig. F28). The downcore changes in NRM intensity reflect the creation and/or destruction of magnetic phases as a response to biogenic, depositional, or diagenetic causes.

Directional Variability

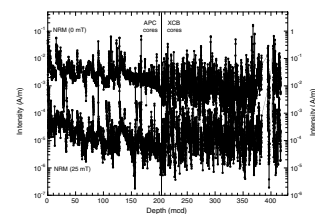
As observed at the previous sites, inclinations prior to AF demagnetization are steeply positive, reflecting the effect of the drill string magnetic field. Within the upper 40 mcd, AF demagnetization at 25 mT removes much of the drill string overprint and inclinations are close to the expected axial dipole inclination for this site (-3.7°) (Fig. F29). Below 40 mcd, steep positive inclination are observed even after 25 mT AF demagnetization, suggesting that much of the overprint remains (Fig. F29). The paleomagnetic data do not clearly record any polarity reversals, and therefore, no shipboard magnetic stratigraphy is available for this site.

GEOCHEMISTRY

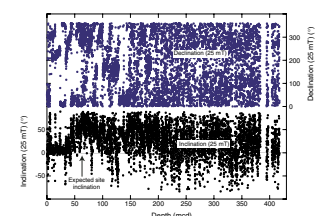
Sediment Gases

Concentrations of headspace gases were routinely monitored in Hole 1238A sediments according to shipboard safety and pollution prevention considerations. Very low amounts of methane were first detected in a headspace gas sample at 10.1 mcd (Fig. F30; Table T13). At greater

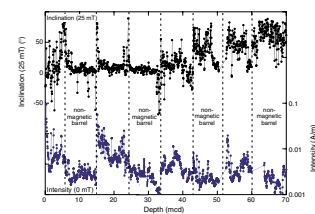
F26. NRM intensity before and after AF demagnetization, p. 58.



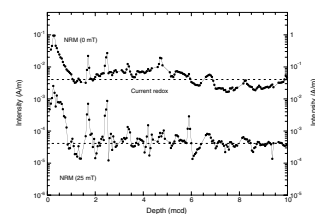
F27. Inclinations and declinations after AF demagnetization, p. 59.



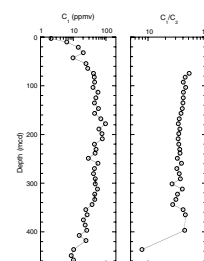
F28. Inclination after AF demagnetization and NRM intensity, p. 60.



F29. NRM before and after AF demagnetization for the upper 10 mcd of Hole 1238A, p. 61.



F30. Headspace methane and C_1/C_2 ratios vs. depth, p. 62.



T13. Headspace methane concentrations and C_1/C_2 ratios in sediments, p. 96.

depths, methane increased smoothly, reaching a maximum of >60 ppmv (and always <100 ppmv) from 167.9 to 209.0 mcd. Methane concentrations decreased downhole to ~10 ppmv at the bottom of the hole. Very small amounts of ethane were detected, and no detectable higher molecular weight hydrocarbons were observed. Low methane concentrations indicate that this gas probably originates from in situ fermentation (methanogenesis) of the organic matter buried in the sediments (Claypool and Kvenvolden, 1983).

Interstitial Water Geochemistry

We collected 33 interstitial water samples from Hole 1238A. Chemical gradients at this site (Table T14; Fig. F31) reflect the influence of organic matter oxidation, the dissolution of biogenic silica and its re-precipitation in authigenic phases, the effects of authigenic calcite precipitation, and the diffusive influence of basalt alteration processes. The dissolved silicate profile shows a pronounced difference from lithologic Subunit IA to Subunit IB.

Chlorinity increases from 552 mM at 3.0 mcd to >560 mM from 32.3 to 301.7 mcd then decreases to 544 mM at 457.9 mcd (Fig. F31). Salinity, measured refractively as total dissolved solids, ranges from 32 to 34 (Table T14). Sodium concentrations measured by inductively coupled plasma–atomic emission spectrophotometry averaged 1% lower than those estimated by charge balance reported here (Table T14). Sodium concentrations parallel chlorinity, with a total range from 468 to 492 mM.

Organic matter diagenesis, driven by microbially mediated oxidation reactions, influences the interstitial water chemistry. Sulfate reduction occurs but does not go to complete disappearance of sulfate, indicating that the rate of labile organic matter supply is not sufficient to exhaust the sulfate supply. Sulfate decreases from 26.8 mM at 3.0 mcd to generally <10 mM by 74.5 mcd, coincident with the top of the organic carbon-rich zone from 78.6 to 94.9 mcd. The relatively wide depth range of sulfate reduction resulted in noticeable hydrogen sulfide in interstitial water samples and in sediments on splitting. Sulfate values are lower in Subunit IB.

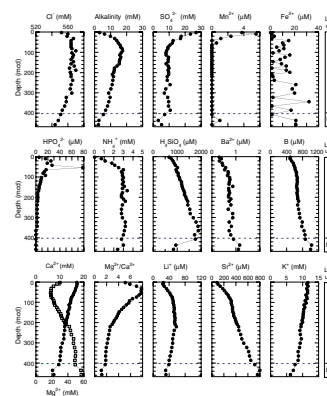
Alkalinity increases from 31 mM near the seafloor to >17 mM from 82.4 to 92.6 mcd, consistent with alkalinity generation from sulfate reduction, then declines to 6.9 mM at 386.3 mcd and to values as low as 2.3 mM at 457.9 mcd. The decline in upper sediments is primarily the result of authigenic carbonate precipitation, based on the calcium profile changes, whereas the deepest decline is also likely from the influence of basalt alteration reactions at depth.

Dissolved manganese has a sharp subsurface maximum up to 5.5 μM at 10.1 mcd, indicative of suboxic oxidation of organic carbon by manganese reduction, then decreases to consistently below the detection limit (0.01 μM) by 64.3 mcd. Dissolved iron has a complex profile with depth, with multiple peaks >10–20 μM .

Phosphate concentrations increase from 5.2 μM at 3.0 mcd to >15 μM from 9.5 to 64.3 mcd. A sharp 1-point maximum of 78 μM at 54.3 mcd is analytically robust but may be an artifact related to the acidification of the samples required to deal with the presence of hydrogen sulfide and/or the possible release of scavenged phosphate from fine particles. Ammonium concentrations increase from below the detection limit (0.4 mM) at 3.0 mcd to an average of 3 mM from 82.4 to 386.3 mcd, with a small decrease at the base of Subunit IB (Fig. F31). The in-

T14. Interstitial water geochemical data, p. 97.

F31. Interstitial water geochemical data, p. 63.



creases in phosphate and ammonium result from the oxidation of organic matter.

Dissolved silicate increases from 668 μM at 3.0 mcd to >1800 μM from 344.1 to 365.2 mcd, with a small decrease in silicate concentration coincident with the depth interval over which silicification of the sediment was first noted (see “**Postdepositional Diagenesis**,” p. 11, in “Lithostratigraphy”). The increase in dissolved silicate with increasing depth is consistent with temperature-controlled solubility for biogenic opal in this site. Silicate concentrations decrease markedly in Subunit IB to <1000 μM as a consequence of the formation of chert and its diagenetic predecessors observed in the sediment and log data.

Barium concentrations increase from 0.3 μM at 3.0 mcd to 0.8 μM at 386.3 mcd, with higher values in the base of Subunit IB with increasing sulfate depletion. This suggests that the dissolution of barite, driven by the decrease in sulfate, influences barium concentrations. Boron concentrations increase from 490 μM at 3.0 mcd to 836 μM at 386.3 mcd and then to >1000 μM from 436.3 to 457.9 mcd.

Calcium decreases from 10.0 mM at 3.0 mcd to 6.1 mM at 54.3 mcd, then increases to 16.3 mM at 386.3 mcd, with a steeper increase with depth in Subunit IB. The shallow part of this profile is controlled by authigenic calcite precipitation driven by the alkalinity increase, and the deeper portion reflects the diffusive influence of basalt alteration. Magnesium is dominated by the diffusive influence of basalt alteration reactions at depth, with Mg decreasing from 51.2 mM at 3.0 mcd to 30.3 mM at 386.3 mcd, followed by a steeper decline with depth in Subunit IB. Magnesium/calcium ratios increase from 5.1 at 3.0 mcd to 7.8 from 32.3 to 54.3 mcd, then decrease to 1.9 by 386.3 mcd and to values as low as 1.1–1.2 in the base of Subunit IB (Fig. F31). The increase in magnesium/calcium in the shallower sediments, driven by the decrease in calcium, indicates that calcite precipitation is the dominant authigenic mineralization reaction. Below this zone, the increase in calcium (~3.3 mM/100 m) is correlated to the decrease in magnesium (approximately –4.9 mM/100 m), consistent with control of these profiles by the diffusive influence of basalt alteration reactions.

Lithium concentrations increase from 26 μM at 3.0 mcd to ≥ 50 μM from 92.6 to 259.3 mcd then decrease to 31–32 μM from 436.3 to 457.9 mcd. The middepth maximum requires a source of lithium from the sediments, whereas basement alteration reactions at low temperatures are a sink for lithium. Strontium concentrations increase steadily from 87 μM at 3.0 mcd to >750 μM from 436.3 to 457.9 mcd. This profile does not resemble those dominated by the influence of biogenic calcite recrystallization at depths of tens to hundreds of meters but does indicate a source of dissolved strontium at depth at this site. Potassium decreases from 11.7 mM at 3.0 mcd to 6.2 mM at 457.9 mcd. Low-temperature basalt alteration reactions are a sink for dissolved potassium, and this profile can be explained by the diffusive influence of basalt alteration reactions.

Sedimentary Inorganic Carbon, Organic Carbon, Nitrogen, Sulfur, and Uranium Concentrations

Inorganic carbon (IC), total carbon (TC), total nitrogen (TN), and total sulfur (TS) were determined on sediment samples from Hole 1238A (Table T15). Organic matter carbon/nitrogen ratios were employed to characterize the organic matter.

T15. IC, CaCO_3 , TC, TOC, TN, and TS concentrations, and TOC/TN ratios in sediments, p. 98.

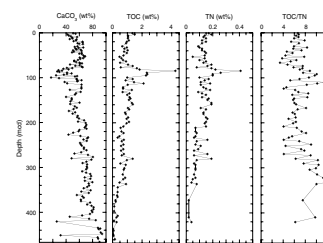
Calcium carbonate concentrations range between 17.4 and 94.3 wt% (average = 60.3 wt%) (Table T15; Fig. F32). Calcium carbonate concentrations increase gradually with depth with meter-scale variations as large as 10–20 wt% throughout. These variations may reflect the productivity of calcareous organisms relative to the siliceous organisms or changes in preservation. Today, the site lies well above the regional lysocline. However, significant local dissolution here may occur in response to organic carbon degradation. One reason for the long-term change in calcium carbonate may be the tectonic migration of the site toward more coastal conditions with a greater delivery of terrigenous material diluting biogenic components. Calcium carbonate concentrations are at a minimum, with values generally <60 wt% from 78.3 to 112.6 mcd. This large drop is associated with an increase in diatom abundance during this interval (see “Diatoms,” p. 15, in “Biostratigraphy”). Again, the combined influences of production and dissolution may be responsible. At depths >400 mcd, some individual samples have low calcium carbonate concentrations.

TOC concentrations range between values near detection limit and 4.3 wt% (average = 0.9 wt%) (Table T15; Fig. F32). The TOC and calcium carbonate profiles correlate inversely. TOC concentrations show a general decrease with depth, with values decreasing from ~1.5 wt% in the upper 4 m to <0.1 wt% at the bottom and small variations of ~0.5 wt% throughout the record. TOC concentrations reach a maximum with values generally >1.5 wt% from 78.6 to 112.6 mcd, with the TOC maximum corresponding to the calcium carbonate minimum.

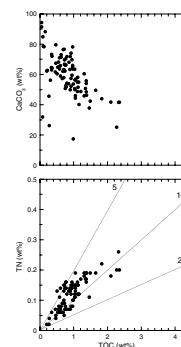
TOC/TN ratios vary from 3.4 to 11.8 (Table T15; Fig. F32). TOC/TN ratios average 7.1, a value typical of unaltered algal material (Borodovskiy, 1965; Emerson and Hedges, 1988; Meyers, 1997), and most of the samples have TOC/TN ratios <9 (Fig. F33). A large change in land-derived organic matter input is excluded, since TOC/TN variations are small compared to TOC content variations, for instance, in the interval where TOC is very high. Changes observed in the organic carbon contents should result from the combination of productivity, preservation of the organic matter, and dilution by calcium carbonate.

The redox conditions in the sediments at the time of deposition can be inferred from the variations in concentration of redox-sensitive components, such as sulfur and uranium. TS concentrations range between 0.1 and 1.4 wt% (average = 0.4 wt%) (Table T15). Higher TS contents are detected in the interval where TOC content is the highest. This could be attributed to the formation of pyrite during the microbial degradation of organic matter by sulfate reduction, possibly driven by an increase in labile organic matter input to the sediment. The uranium profile is derived from the natural gamma ray activity signal measured during downhole logging operations (see “Natural Gamma Radiation,” p. 22, in “Downhole Measurements”). Uranium is a conservative element, soluble in seawater as U(VI) (unreactive uranyl carbonate complex) and insoluble when reduced to U(IV). Uranium is supplied to the pore water by diffusion from the overlying water. It precipitates as an authigenic phase (uraninite; UO_2) at or just below the depth of iron oxide reduction during organic matter diagenesis (Barnes and Cochran, 1990; Klinkhammer and Palmer, 1991). Therefore, sedimentary uranium is a good indicator of suboxic conditions in the sediments. A comparison of U contents and TOC contents at Site 1238 shows a good correlation between the two records (see Fig. F42), indicating more reducing (suboxic) conditions in the sediments when (labile) organic matter input to the sediment increased. Again, this supports an inter-

F32. $CaCO_3$, TOC, and TN concentrations, and TOC/TN ratios in sediments, p. 64.



F33. $CaCO_3$ vs. TOC and TN vs. TOC, p. 65.



pretation that high concentrations of organic matter are driven by productivity rather than dilution or preservation.

DOWNHOLE MEASUREMENTS

Logging Operations

Downhole logging was performed in Hole 1238A after it had been drilled to a depth of 430.6 mbsf with a 11.438-in APC/XCB drill bit (see “Operations,” p. 1, in the “Explanatory Notes” chapter) and displaced with sepiolite mud, and the pipe initially was set at 99.4 mbsf. Two tool string configurations were run, the triple combo-MGT and the FMS-sonic (see “Downhole Measurements,” p. 36, in the “Explanatory Notes” chapter). No problems were encountered while logging, and all passes reached the base of the hole. Details of the intervals logged with each tool configuration, together with the position of the drill bit, are shown in Figure F34. During each pass, the pipe was pulled to 84 mbsf to allow the upper unit to be logged. The Dipole Sonic Imager (DSI) on the FMS-sonic was run in P&S (middle frequency), lower dipole (low frequency), and first motion detection (FMD) modes. Weather was excellent and the sea state was calm with peak heave <2 m. The wireline heave compensator was used throughout the logging operations.

Results/Data Quality

The caliper data show that the borehole was relatively smooth and varied between 11.5 and 15 in (Fig. F35), resulting in excellent data from the density, porosity, and FMS tools that require good borehole contact. Although the hole deviation increased with depth, reaching 6.5° at the base, FMS pad contact was not affected and the images were good from the base of the hole to 117 mbsf, where the calipers were closed. Downhole log-derived densities mirror the downhole porosities (Fig. F36). Natural gamma radiation measurements are highly reproducible between tools and passes and also closely match the core-derived natural gamma radiation record from Hole 1238A (Figs. F35, F37, F38). Sonic velocities were also generally good and reproduced well between passes, apart from the interval between 387 and 410 mbsf, where the main pass should be used (Fig. F36).

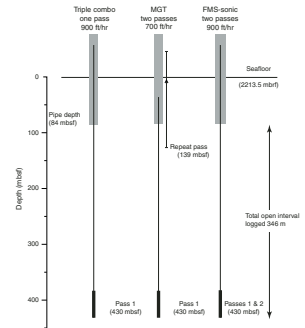
Logging Units

Three logging units have been defined using porosity, density, resistivity, and sonic velocity, which show coherent downhole shifts associated with changes in formation lithology, competence, and lithification.

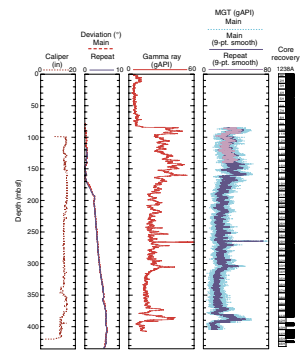
Logging Unit 1 (Base of Pipe [84 mbsf] to 209 mbsf)

Throughout this unit, the mean values of velocity, resistivity, and density are relatively low, whereas porosity remains high. Sonic velocities and densities increase slightly with depth through this interval, most likely because of sediment compaction. Formation NGR is relatively high and variable within this unit. Density and porosity values show subtle but regular fluctuations throughout this interval, which are

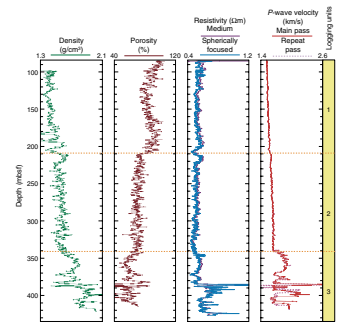
F34. Logging tool string deployments, p. 66.



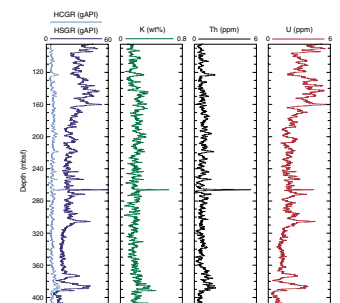
F35. Caliper, deviation, and gamma ray records, p. 67.



F36. Density, porosity, sonic velocity, and resistivity data, p. 68.



F37. Total and spectral gamma ray data, p. 69.



most likely associated with the nannofossil to diatom ooze oscillations observed in the cores (see “[Lithostratigraphy](#),” p. 6).

Logging Unit 2 (209–341 mbsf)

At ~209 mbsf, mean velocities and densities increase stepwise while mean porosities decrease, marking the boundary between logging Units 1 and 2. This shift suggests an increase in sediment consolidation/lithification at this depth and is within the interval covered by the first XCB core. Sonic velocities within this unit continue to increase gradually with depth, whereas mean resistivity, porosity, and density values show no trends with depth and have variance similar to that in logging Unit 1. Color banding on the FMS images occurs on a scale similar to the density changes attributed to nannofossil/diatom oscillations (Fig. [F39](#)).

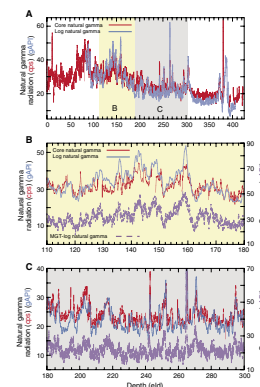
Logging Unit 3 (341 mbsf to Base of Hole)

The increase in mean and variance of sonic velocity, resistivity, and density (and the attendant decrease in porosity) at 341 mbsf marks the top of logging Unit 3. In addition, a number of strong spikes in resistivity, sonic velocity, and density (porosity minima) punctuate logging Unit 3, occurring first at ~345 mbsf and with increased frequency below the most pronounced event at ~386 mbsf (Fig. [F40](#)). This mean rise in resistivity and velocity implies a general increase in formation lithification below ~341 mbsf, near the lithologic Subunit IA/IB boundary, which marks the ooze to chalk transition (see “[Lithostratigraphy](#),” p. 6). The most pronounced spikes in physical properties are likely caused by particularly well cemented or lithified layers. Indeed, the most prominent spike in physical properties occurs within the depth range of Core 202-1239A-42X (384.5–394 mbsf), where coring was difficult and recovery was only 34 cm of well-lithified chalk (see “[Operations](#),” p. 3, and “[Lithostratigraphy](#),” p. 6). The statically normalized FMS image from the same interval shows a series of highly lithified (resistive) beds separated by centimeter- to decimeter-thick layers of less lithified (resistive) material (Fig. [F41](#)). The attendant decrease in pore water silicate concentrations (see “[Geochemistry](#),” p. 17) with increased lithification suggests that sediment diagenesis drives the physical property changes in Logging Unit 3.

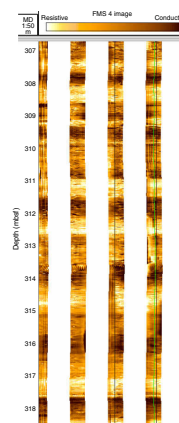
Natural Gamma Radiation

The NGR activity in Hole 1238A shows significant meter-scale variability superimposed upon a general decrease with depth (Figs. [F35](#), [F37](#), [F38](#)). The spectral gamma results from the Hostile Environment Gamma Ray Sonde (HNGS) tool (Fig. [F37](#)) show low, regularly varying Th and K activity throughout the sequence. In contrast, the U activity and variability is much greater, increasing significantly between 120 and 160 mbsf and again near the top of the open sequence (~95 mbsf) to the bit (84 mbsf), where the tool enters the pipe and gamma rays are attenuated. The high U activity dominates the total gamma ray activity of the sediments. The strong correlation between U and TOC measured in the cores (Fig. [F42](#)) indicates that changes in organic matter rather than terrigenous input has controlled sediment gamma ray activity at Site 1238 since the late Miocene (see “[Geochemistry](#),” p. 17).

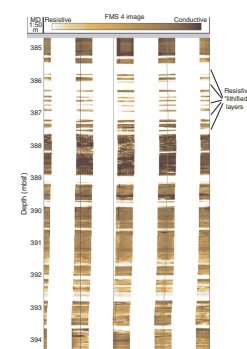
F38. Downhole and core gamma ray vs. eld, p. 70.



F39. FMS image illustrating meter-scale banding, p. 71.



F40. FMS image showing the resistive, well-lithified beds, p. 72.



at younger ages would be predicted by the eastward tectonic drift toward the continental margin (see **“Introduction,”** p. 1). At ages <3 Ma (<150 mcd), however, the rates drop rather abruptly and remain lower from 3 to 1 Ma, and this decrease is not predicted by tectonics. During the last 1 m.y. (<56 mcd), the MAR decreased further, whereas the LSR slightly increased. The divergence of LSR and MAR since 1 Ma can be explained by increased siliciclastic (clay) input during that time, decreasing overburden in the top section, and the associated increase in porosity (see Figs. **F15, F19**).

The broad peak in carbonate MARs from 7 to 3 Ma likely represent changes in the productivity of calcareous organisms because a similar peak at ~7 to 5 Ma is present within the records of other Leg 202 sites (see Figs. **F20**, p. 95, and **F34**, p. 109, in the “Leg Summary” chapter) and is known from other equatorial Pacific sites where it is interpreted as a production signal (Farrell et al., 1995; Pisias et al., 1995).

REFERENCES

- Barnes, C.E., and Cochran, J.K., 1990. Uranium removal in oceanic sediments and the oceanic U balance. *Earth Planet. Sci. Lett.*, 97:94–101.
- Beaufort, L., Garidel-Thoron, T., Mix, A.C., and Pisias, N.G., 2001. ENSO-like forcing on oceanic primary production during the late Pleistocene. *Science*, 293:2440–2444.
- Behrenfeld, M.J., Randerson, J.T., McClain, C.R., Feldman, G.C., Los, S.O., Tucker, C.J., Falkowski, P.G., Field, C.B., Frouin, R., Esaias, W.E., Kolber, D.D., and Pollack, N.H., 2001. Biospheric primary production during and ENSO transition. *Science*, 291:2594–2597.
- Berggren, W.A., Kent, D.V., Swisher, C.C., III, and Aubry, M.-P., 1995. A revised Cenozoic geochronology and chronostratigraphy. In Berggren, W.A., Kent, D.V., Aubry, M.-P., and Hardenbol, J. (Eds.), *Geochronology, Time Scales and Global Stratigraphic Correlation*. Spec. Publ.—SEPM, 54:129–212.
- Bordovskiy, O.K., 1965. Accumulation and transformation of organic substances in marine sediment, 2. Sources of organic matter in marine basins. *Mar. Geol.*, 3:5–31.
- Bowles, F.A., Jack, R.N., and Carmichael, I.S.E., 1973. Investigation of deep-sea volcanic ash layers from Equatorial Pacific cores. *Geol. Soc. Am. Bull.*, 84:2371–2388.
- Cane, M.A., 1986. El Niño. *Annu. Rev. Earth Planet. Sci.*, 14:43–70.
- Claypool, G.E., and Kvenvolden, K.A., 1983. Methane and other hydrocarbon gases in marine sediment. *Annu. Rev. Earth Planet. Sci.*, 11:299–327.
- Duncan, R.A., and Hargraves, R.B., 1984. Plate tectonic evolution of the Caribbean region in the mantle reference frame. In Bonini, W.E., Hargraves, R.B., and Shagam, R. (Eds.), *The Caribbean-South American Plate Boundary and Regional Tectonics*. Mem.—Geol. Soc. Am., 162:81–94.
- Emerson, S., and Hedges, J.I., 1988. Processes controlling the organic carbon content of open ocean sediments. *Paleoceanography*, 3:621–634.
- Farrell, J.W., Raffi, I., Janecek, T.C., Murray, D.W., Levitan, M., Dadey, K.A., Emeis, K.-C., Lyle, M., Flores, J.-A., and Hovan, S., 1995. Late Neogene sedimentation patterns in the eastern equatorial Pacific. In Pisias, N.G., Mayer, L.A., Janecek, T.R., Palmer-Julson, A., and van Andel, T.H. (Eds.), *Proc. ODP, Sci. Results*, 138: College Station, TX (Ocean Drilling Program), 717–756.
- Jousé, A.P., Kazarina, G.H., and Mukhina, V.V., 1982. Distribution of diatoms in Pliocene and Pleistocene deposits from the middle America trench off Guatemala. In Aubouin, J., von Huene, R., et al., *Init. Repts. DSDP*, 67: Washington (U.S. Govt. Printing Office), 455–471.
- Kemp, A.E.S., Baldauf, J.G., and Pearce, R.B., 1995. Origins and paleoceanographic significance of laminated diatom ooze from the eastern equatorial Pacific Ocean. In Pisias, N.G., Mayer, L.A., Janecek, T.R., Palmer-Julson, A., and van Andel, T.H. (Eds.), *Proc. ODP, Sci. Results*, 138: College Station, TX (Ocean Drilling Program), 641–645.
- Klinkhammer, G.P., and Palmer, M.R., 1991. Uranium in the oceans: where it goes and why. *Geochim. Cosmochim. Acta*, 55:1799–1806.
- Lea, D.W., Pak, D.K., and Spero, H.J., 2000. Climate impact of late Quaternary equatorial Pacific sea surface temperature variations. *Science*, 289:1719–1724.
- Ledbetter, M.T., 1985. Tephrochronology of marine tephra adjacent to Central America. *Geol. Soc. Am. Bull.*, 96:77–82.
- Lind, I.L., Janecek, T.R., Krissek, L.A., Prentice, M.L., and Stax, R., 1993. Color bands in Ontong Java Plateau carbonate oozes and chalks. In Berger, W.H., Kroenke, L.W., Mayer, L.A., et al., *Proc. ODP, Sci. Results*, 130: College Station, TX (Ocean Drilling Program), 453–470.
- Lonsdale, P., and Klitgord, K.D., 1978. Structure and tectonic history of the eastern Panama Basin. *Geol. Soc. Am. Bull.*, 89:981–999.

- Lyle, M., Liberty, L., Mix, A., Pisias, N., Goldfinger, C., Hulett, D., Janik, A., 2000. *Site Survey Data Package 5: Site Surveys for ODP Leg 201 from the NEMO-3 Cruise, in Support of Proposal 465: Southeast Pacific Paleoceanographic Transects*. CGISS Tech. Rpt. 2000-06, Boise State University.
- Meyers, P.A., 1997. Organic geochemical proxies of paleoceanographic, paleolimnologic, and paleoclimatic processes. *Org. Geochem.*, 27:213–250.
- Mix, A.C., Morey, A.E., Pisias, N.G., and Hostetler, S., 1999. Foraminiferal faunal estimates of paleotemperatures: circumventing the no-analog problems yields cool ice-age tropics. *Paleoceanography*, 14:350–359.
- Mix, A.C., Pisias, N.G., Goldfinger, C., Lyle, M., Liberty, L., Janik, A., Hebbeln, D., Wefer, G., and Lamy, F., 2000. *Southeast Pacific Paleoceanographic Transects, Site Survey Data Package 4: NEMO Expedition, Leg III, R/V Melville, May–June 2000*: Corvallis (Oregon State Univ.).
- Murray, J.W., Barber, R.T., Roman, M.R., Bacon, M.P., and Feely, R.A., 1994. Physical and biological controls on carbon cycling in the equatorial Pacific. *Science*, 266:58–65.
- Ninkovich, D., and Shackleton, N.J., 1975. Distribution, stratigraphic position and age of ash layer L, in the Panama Basin region. *Earth Planet. Sci. Lett.*, 27:20–34.
- Ocean Climate Laboratory, 1999. *World Ocean Atlas 1998 (WOA98)* [CD-ROM]. Available from: National Climatic Data Center, Asheville NC 28801-5001, USA.
- Pisias, N.G., Mayer, L.A., and Mix, A.C., 1995. Paleoceanography of the eastern equatorial Pacific during the Neogene: synthesis of Leg 138 drilling results. In Pisias, N.G., Mayer, L.A., Janecek, T.R., Palmer-Julson, A., and van Andel, T.H. (Eds.), *Proc. ODP, Sci. Results*, 138: College Station, TX (Ocean Drilling Program), 5–21.
- Pisias, N.G., and Mix, A.C., 1997. Spatial and temporal oceanographic variability of the eastern equatorial Pacific during the late Pleistocene: evidence from radiolaria microfossils. *Paleoceanography*, 12:381–393.
- Silva, A.J., Hollister, C.D., Laine, E.P., and Beverly, B., 1976. Geotechnical properties of the northern Bermuda Rise. *Mar. Geotechnol.*, 1:195–232.
- Strub, P.T., Mesias, J.M., Montecino, V., Rutllant, J., and Salinas, S., 1998. Coastal ocean circulation off western South America. In Robinson, A.R., and Brink, K.H. (Eds.), *The Sea* (Vol. 11): *Coastal Oceans*: New York (Wiley), 273–313.
- Tsuchiya, M., and Talley, L.D., 1998. A Pacific hydrographic section at 88°W: water-property distribution. *J. Geophys. Res.*, 103:12899–12918.

Figure F1. Locations of Sites 1238–1242 and regional bathymetry of Carnegie Ridge.

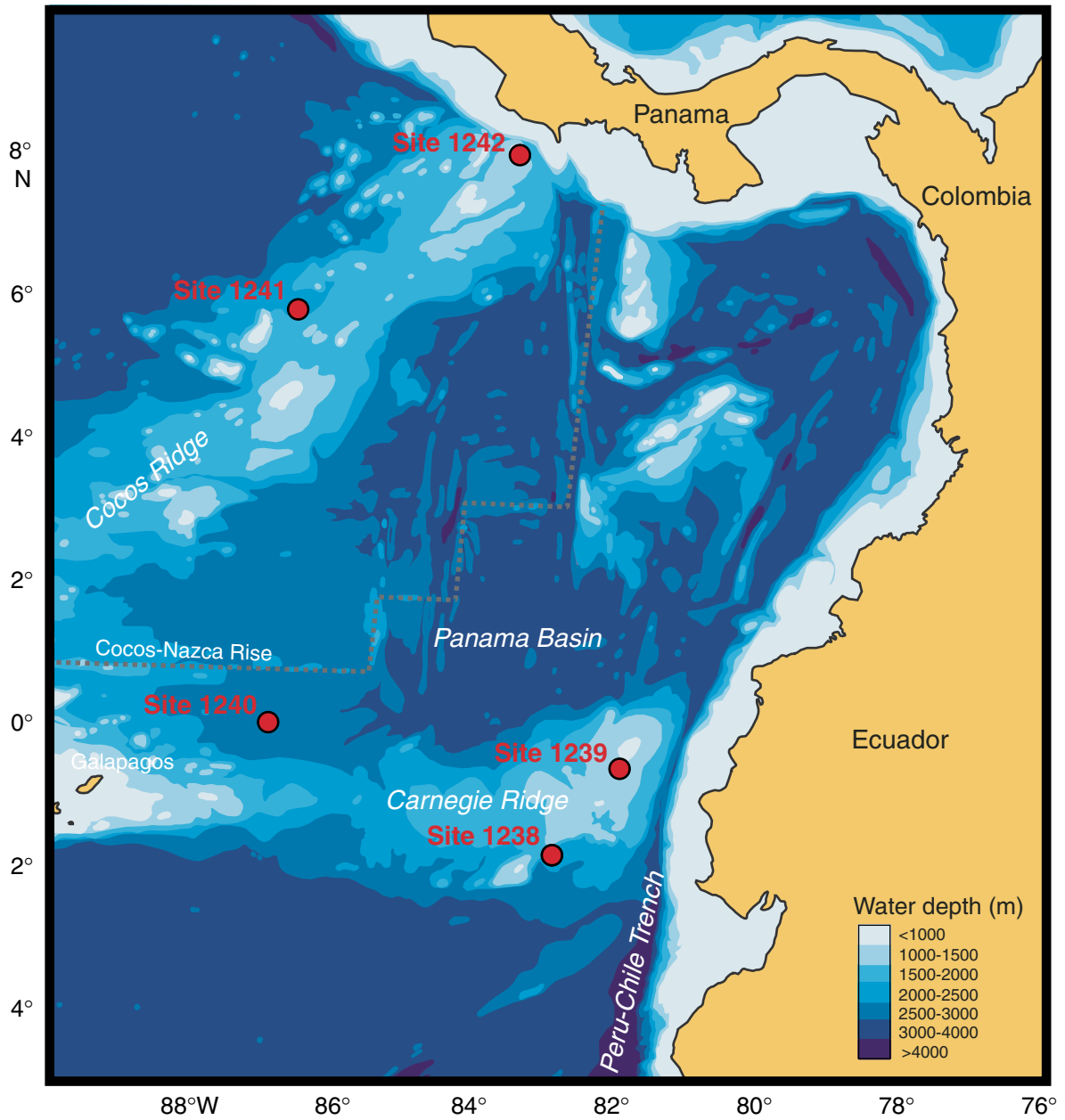


Figure F2. High-resolution swath bathymetry, illustrated in an oblique view (Mix et al., 2000). The sedimented ramp covers an area of ~40 km (northwest-southeast) × ~30 km (southwest-northeast).

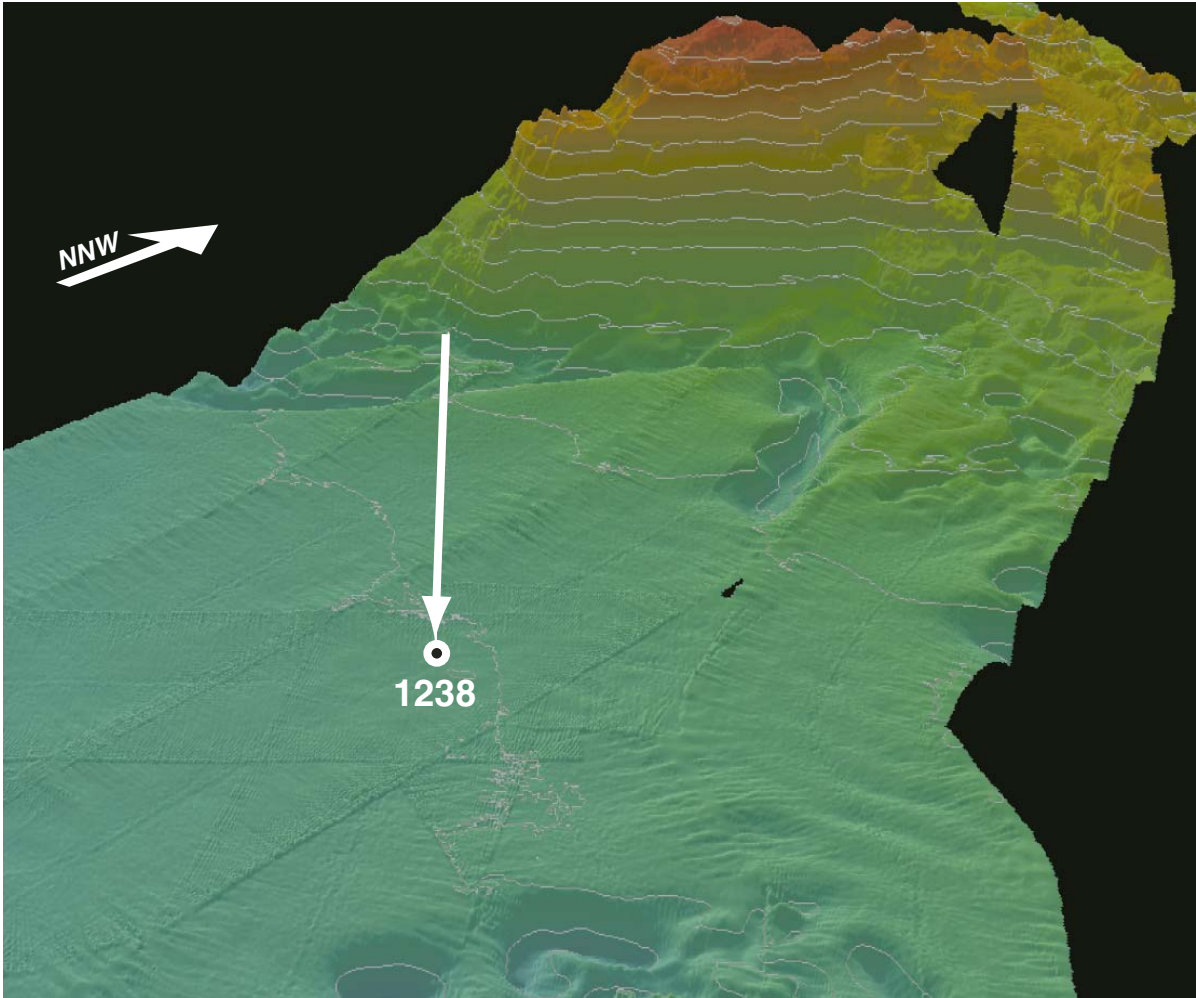


Figure F3. Seismic profile at Site 1238 (*Melville, NEMO-3, CAR-2, line 6, JD151; two 150-in³ generator injector guns; Lyle et al., 2000*).

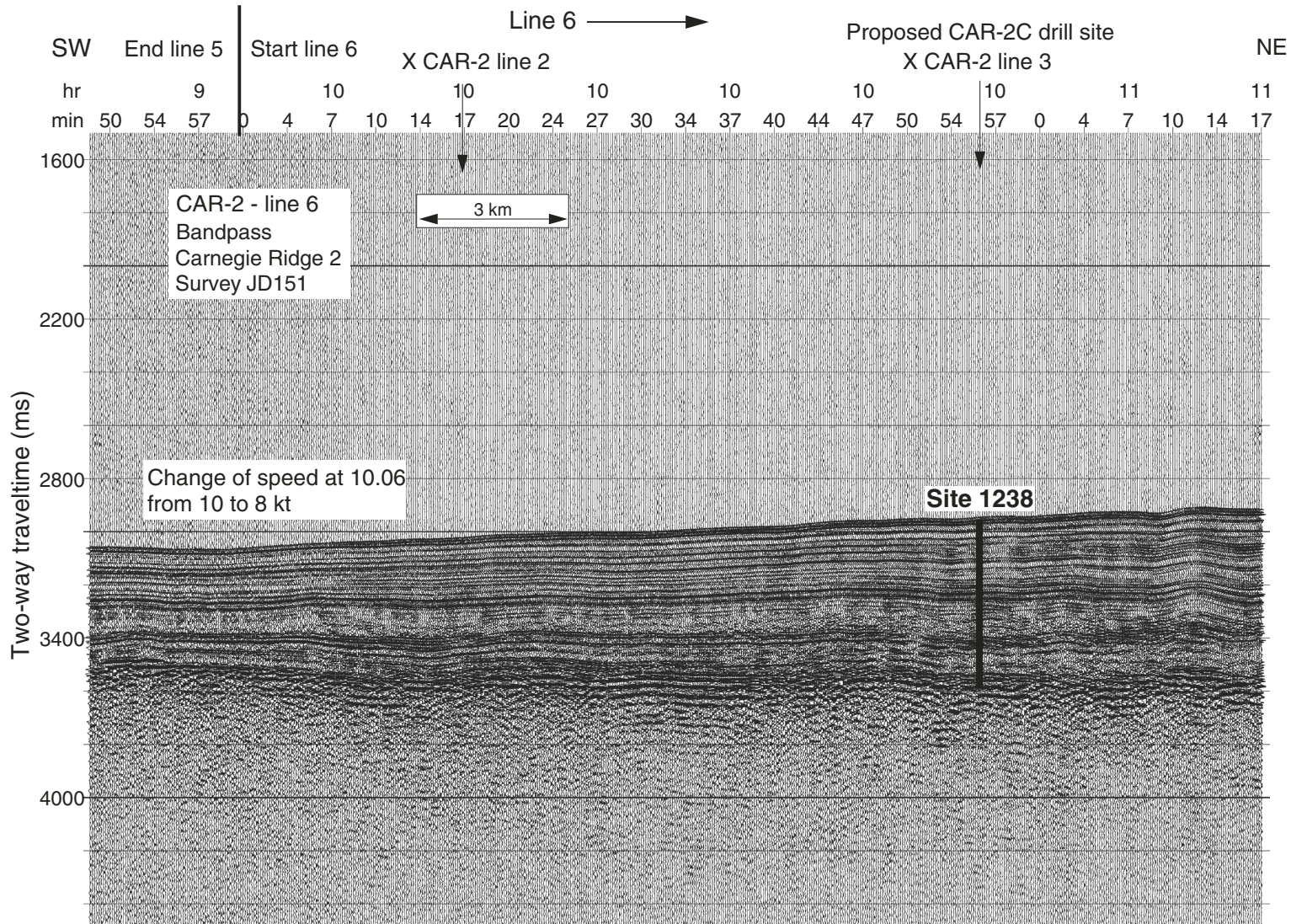


Figure F4. Tectonic backtrack of Site 1238, relative to a fixed South America. Poles of rotation are from Duncan and Hargraves (1984) and Pias et al. (1995). The dotted path represents position of sites in million-year increments. Numbers note the age (in millions of years) of changes in rate or direction of drift. Contours of modern mean annual sea-surface temperature are superimposed (Ocean Climate Laboratory, 1999).

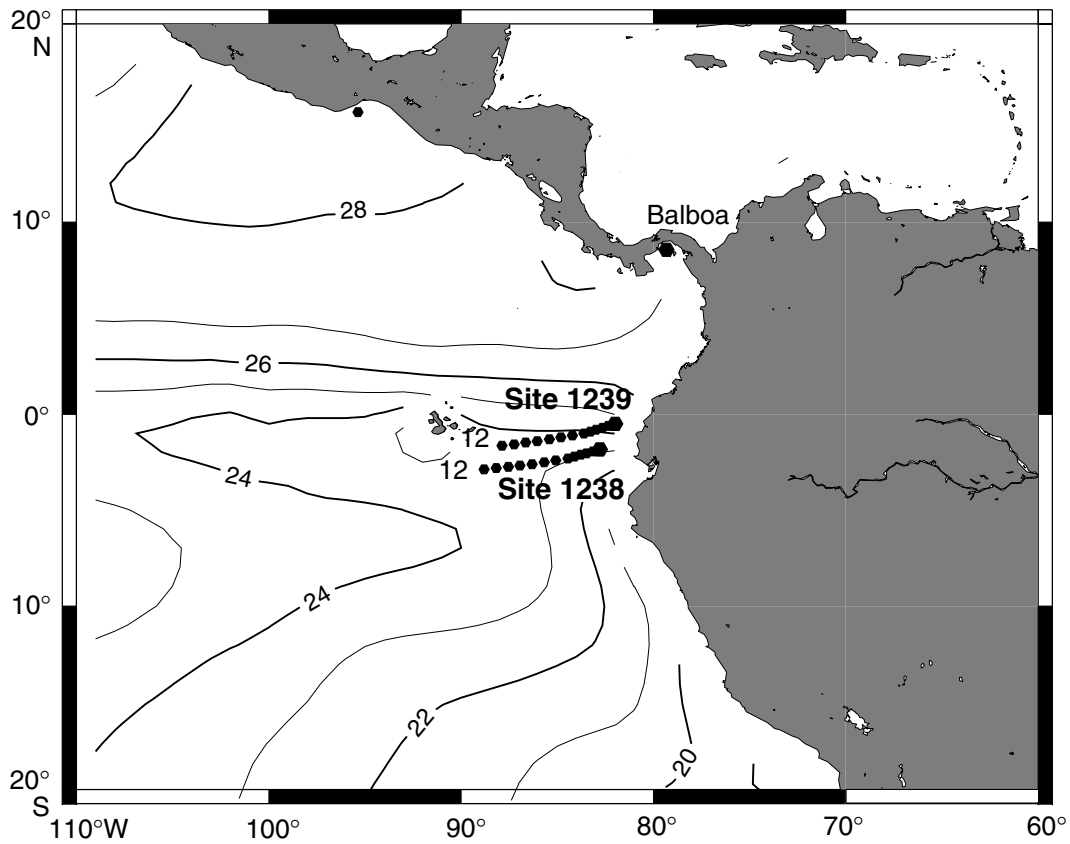


Figure F5. Upper-ocean features off Peru and northern Chile during Southern Hemisphere winter (after Strub et al., 1998). SEC = South Equatorial Current, NECC = North Equatorial Countercurrent, EUC = Equatorial Undercurrent, PCC = Peru-Chile Current, PCCC = Peru-Chile Countercurrent, CC = Coastal Current, GUC = Gunther Undercurrent. Modern mean annual sea-surface temperatures (SSTs) (in degrees Celsius, after Ocean Climate Laboratory, 1999).

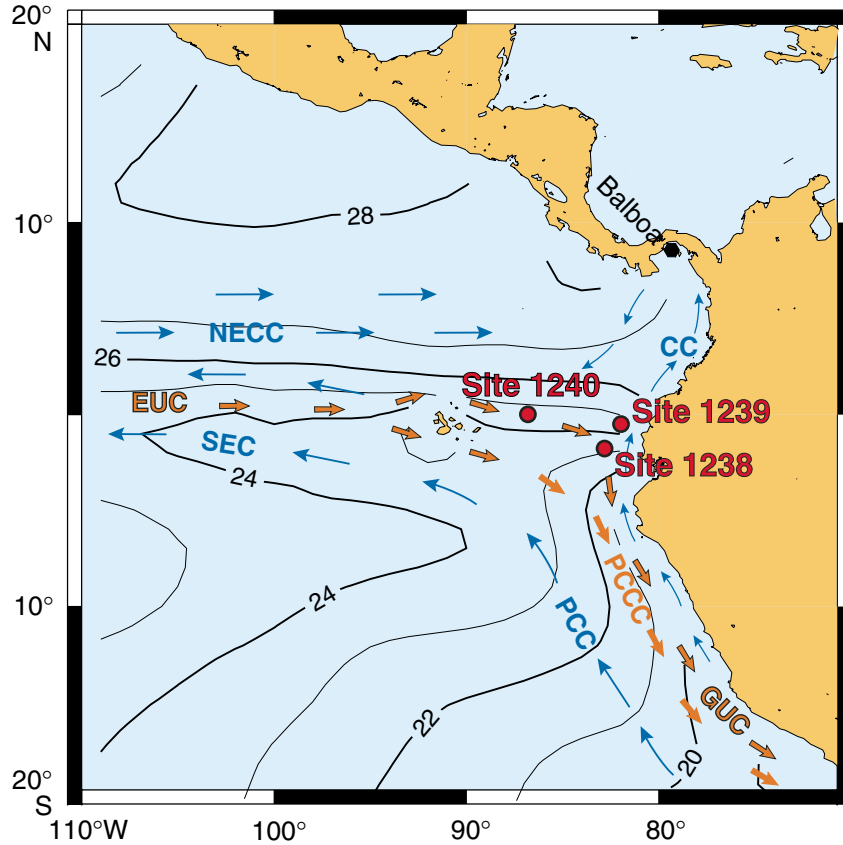


Figure F6. Chlorophyll distributions in surface waters of the equatorial Pacific, based on satellite color data, reveal that Site 1238 is now within the highly productive upwelling system off Ecuador.

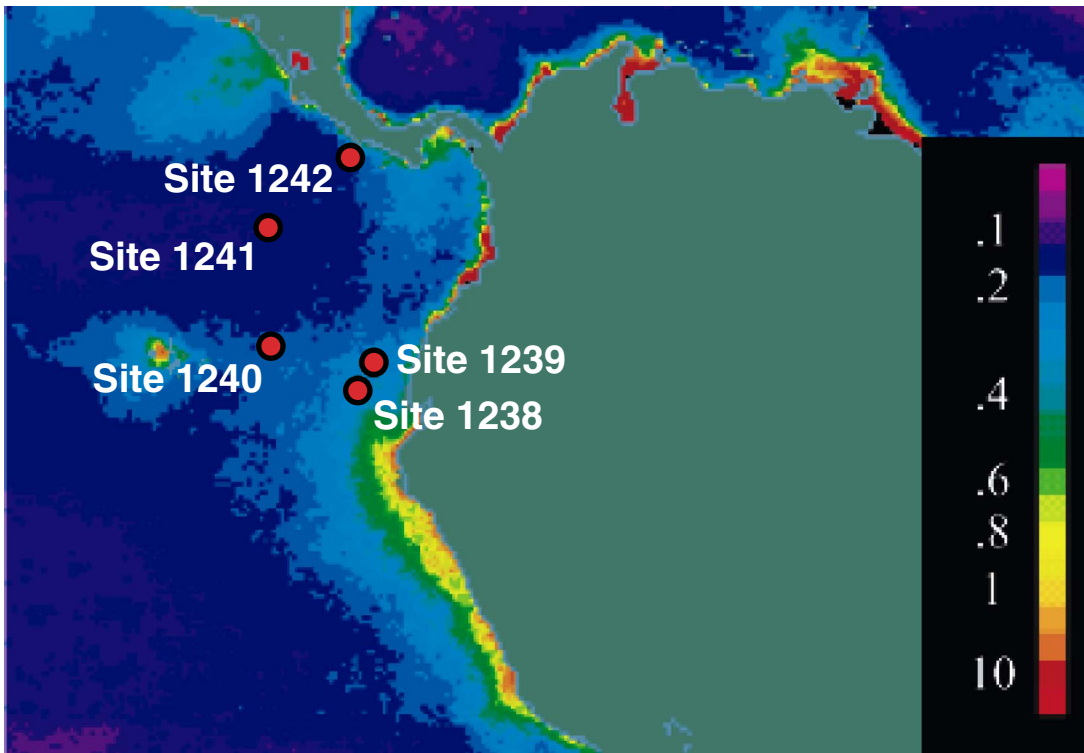


Figure F7. Modern annual-average properties of the upper ocean at paleolocations of Site 1238, based on plate tectonic backtracking and an assumption of no temporal changes in regional oceanic properties. Atlas data on physical and chemical properties are from WOA98 (Ocean Climate Laboratory, 1999). Primary productivity (PP) is from satellite measurements of sea-surface color (Behrenfeld et al., 2001). Pycnocline depth is calculated to the nearest 5 m, based on the shallowest maximum in the vertical density gradient. Symbols are average values extracted from the nearest 1° latitude-longitude box in each atlas. Lines = smoothed trends of each property along the backtrack path. SST = sea-surface temperature, SSS = sea-surface salinity.

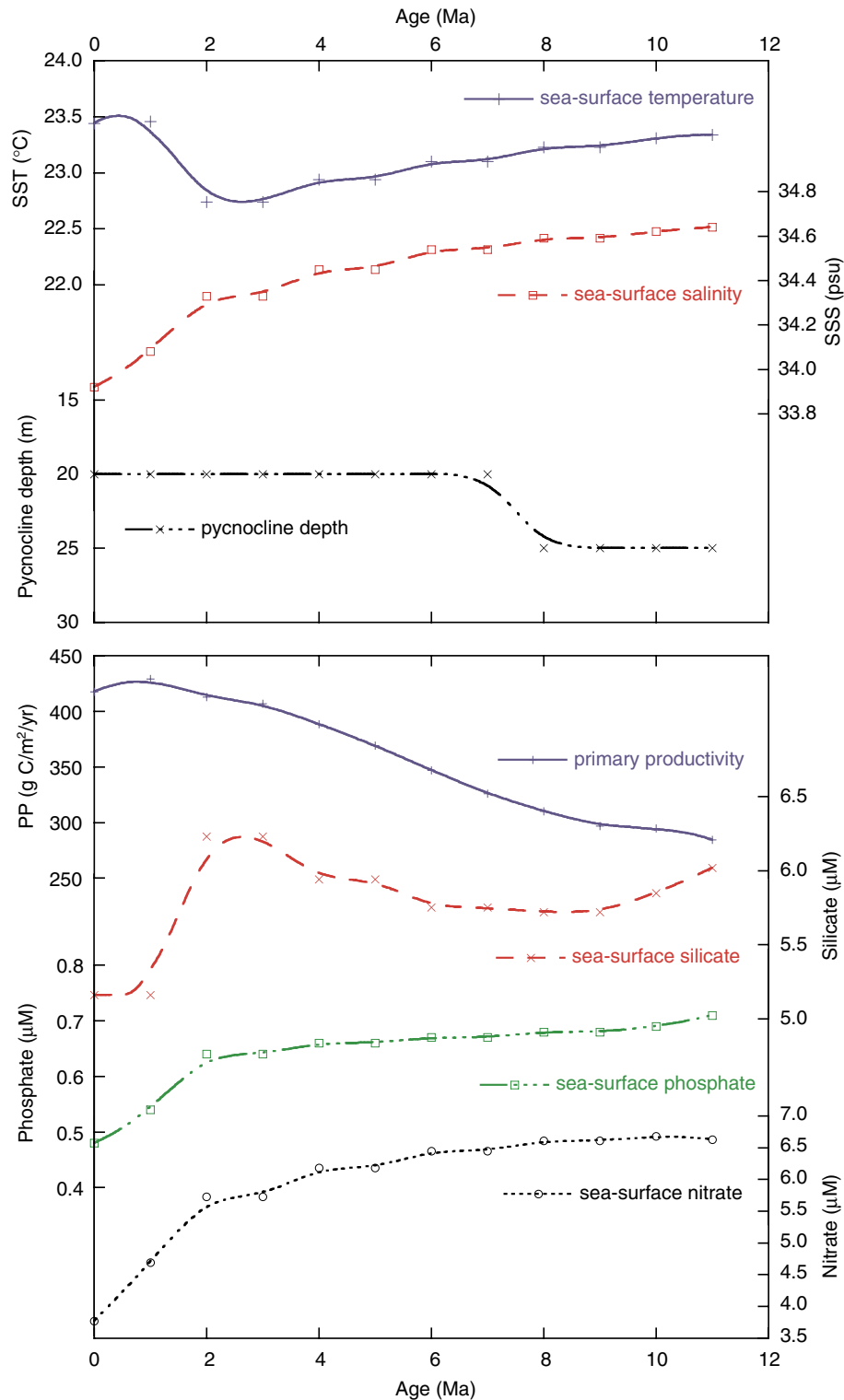


Figure F8. Meridional cross section of water masses, characterized by dissolved oxygen concentrations in the southeast Pacific (Ocean Climate Laboratory, 1999). GUC = Gunther Undercurrent, EUC = Equatorial Undercurrent, NPIW = North Pacific Intermediate Water, PCW = Pacific Central Water, PBW = Peru Basin Water.

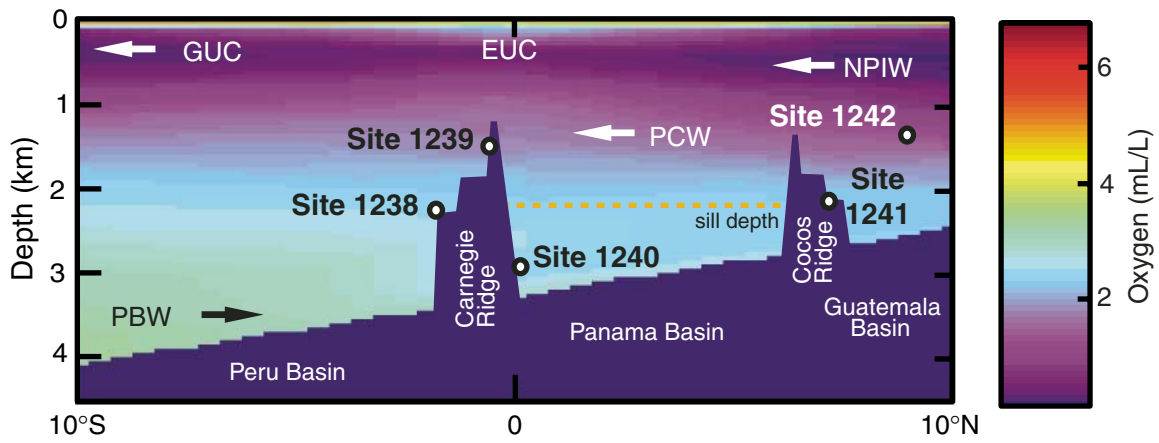


Figure F9. OSU Fast Track magnetic susceptibility data (OSUS-MS) vs. mcd for the spliced record and Holes 1238A, 1238B, and 1238C. Gray boxes indicate the portions of cores that are in the splice. A. 0–40 mcd. B. 30–70 mcd. (Continued on next five pages.)

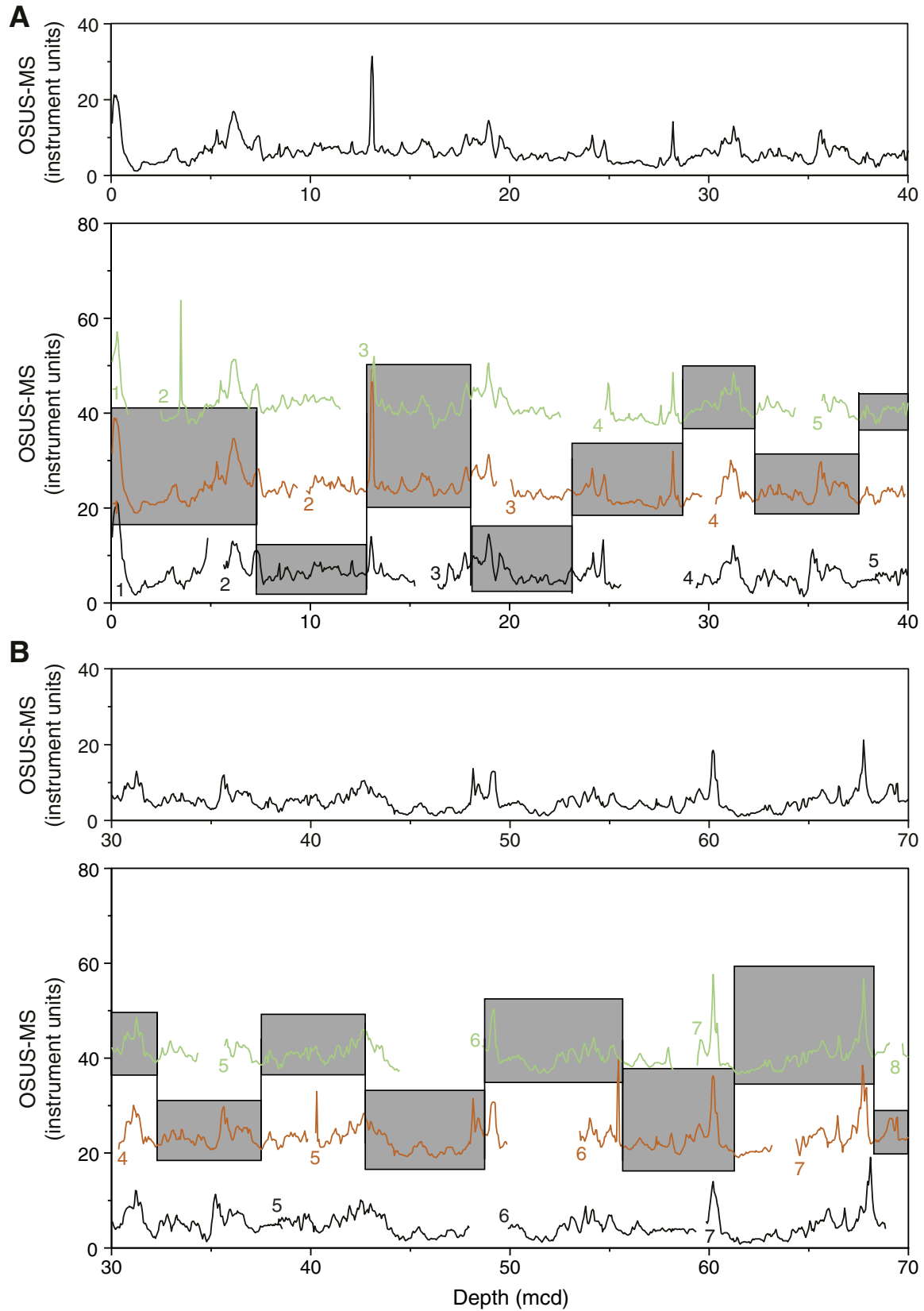


Figure F9 (continued). C. 60–100 mcd. D. 90–130 mcd.

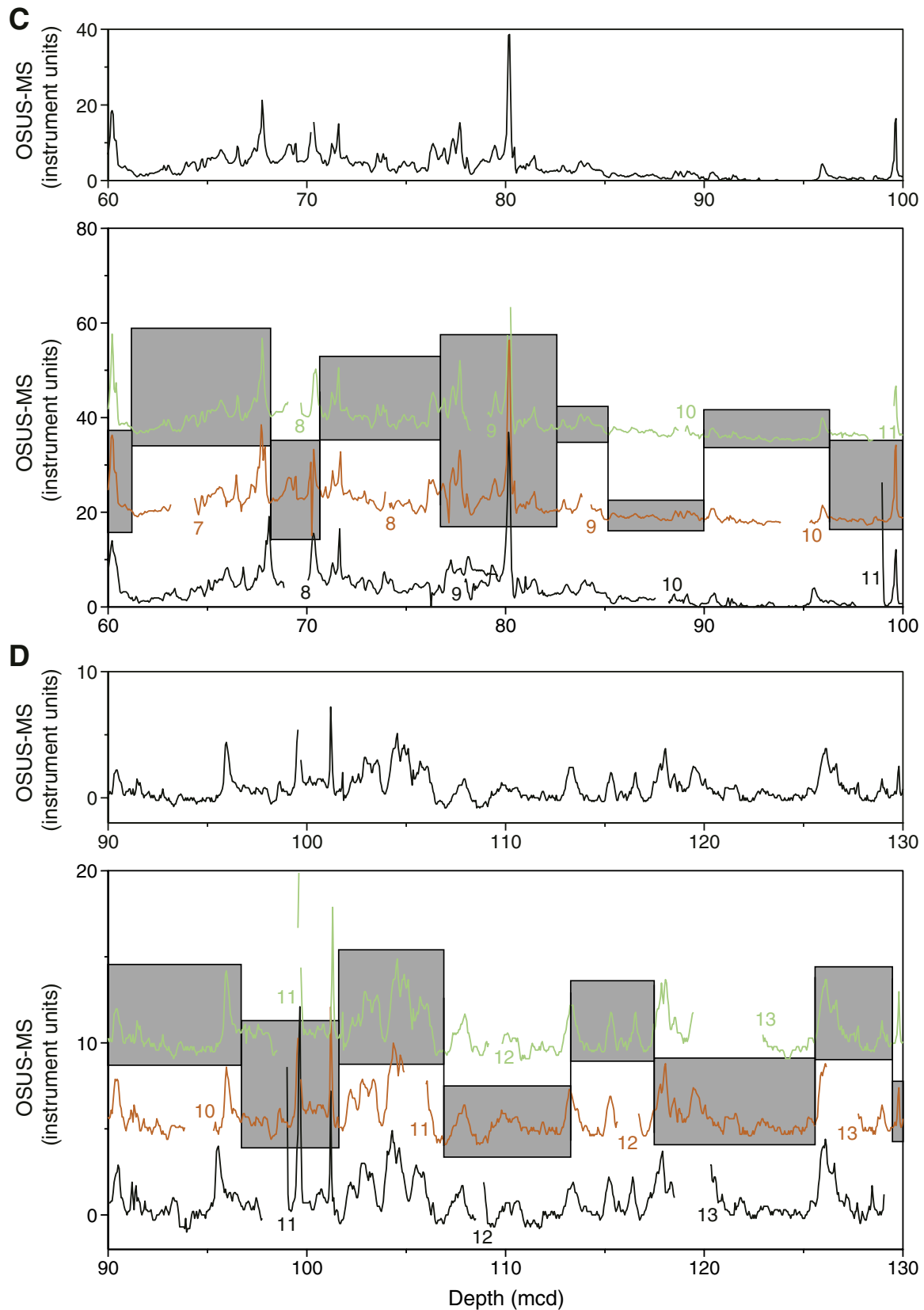


Figure F9 (continued). E. 120–160 mcd. F. 150–190 mcd.

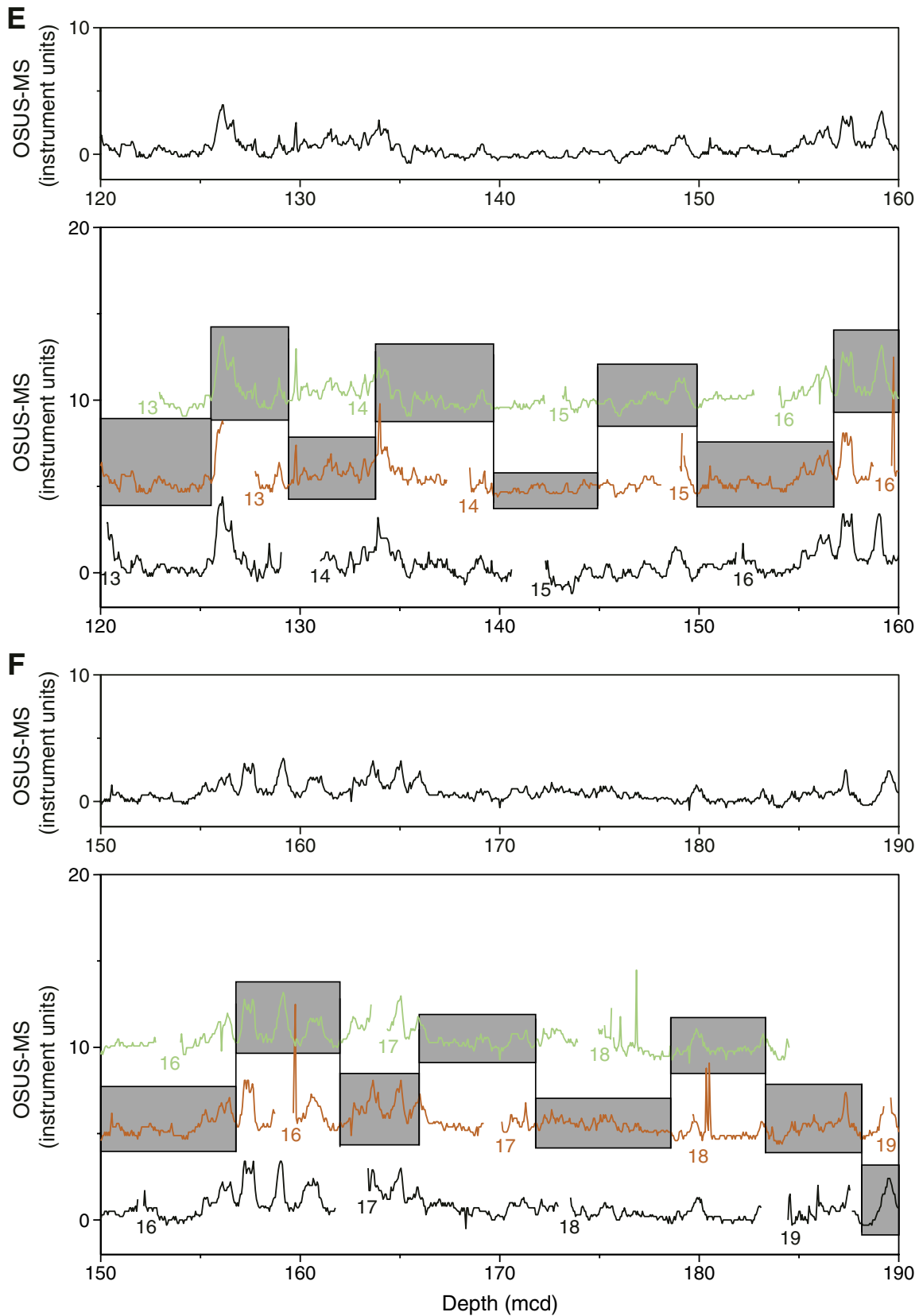


Figure F9 (continued). G. 180–220 mcd. H. 210–250 mcd.

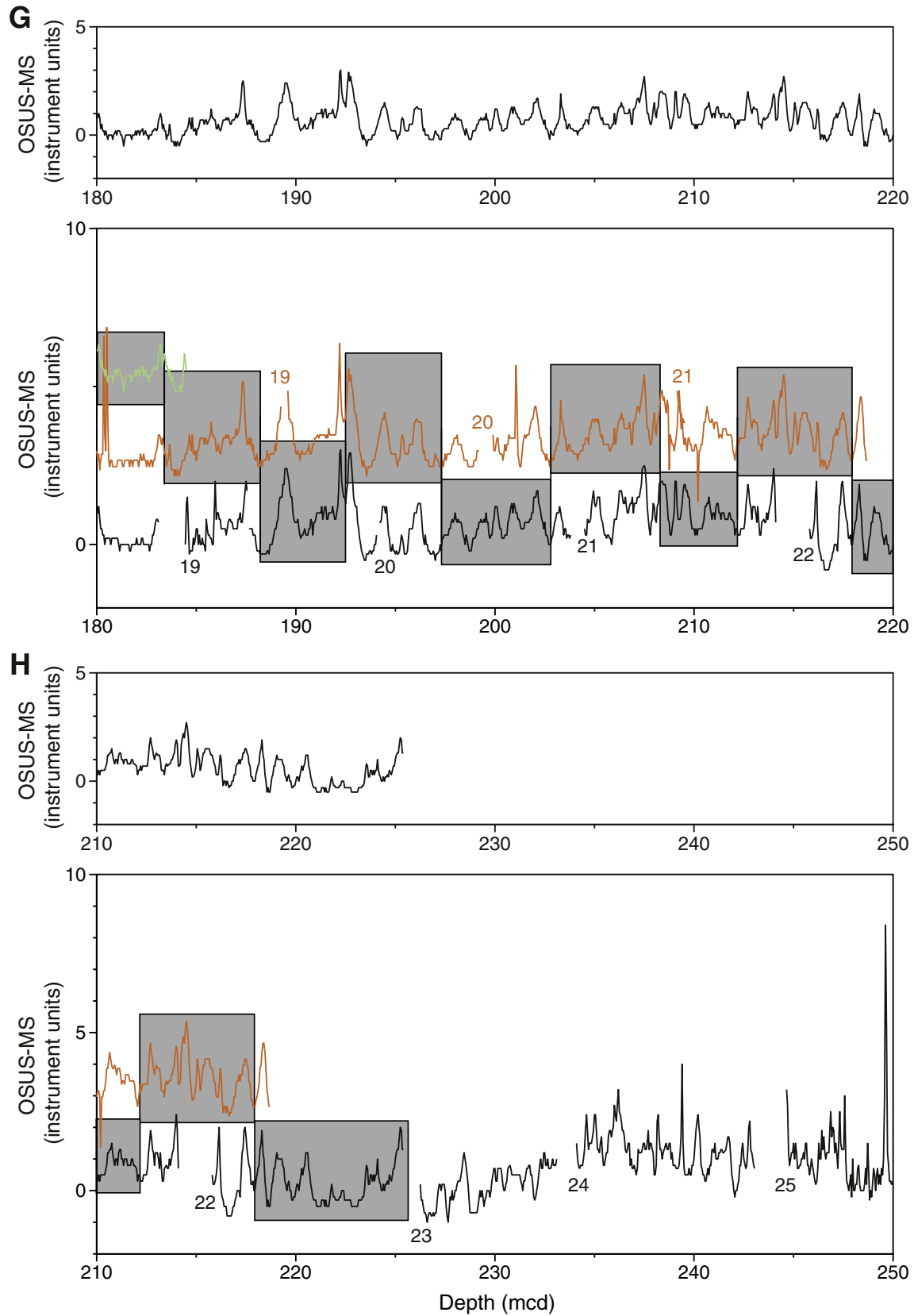


Figure F9 (continued). I. 240–280 mcd. J. 270–310 mcd. K. 300–340 mcd.

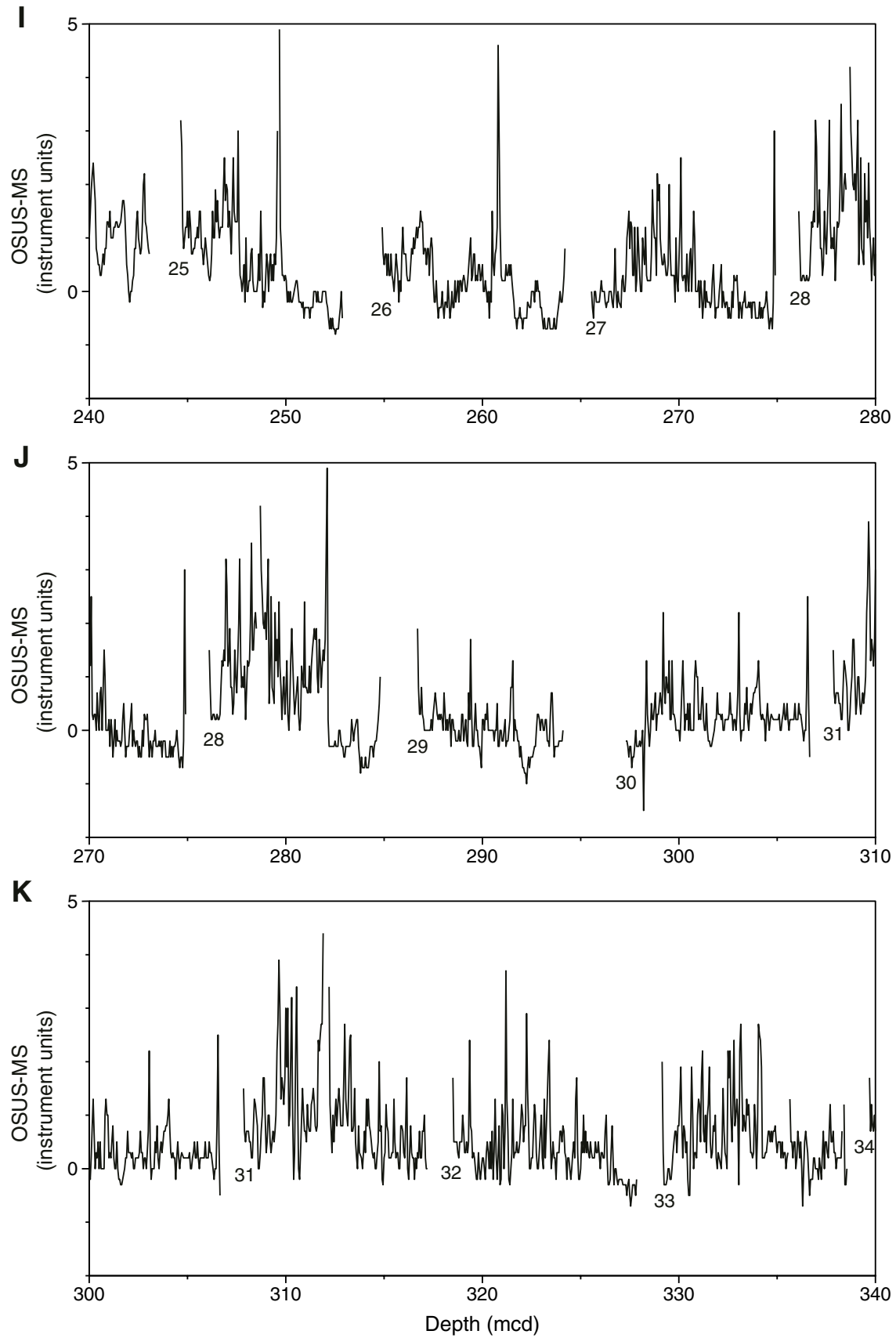


Figure F9 (continued). L. 330–370 mcd. M. 360–400 mcd. N. 390–430 mcd.

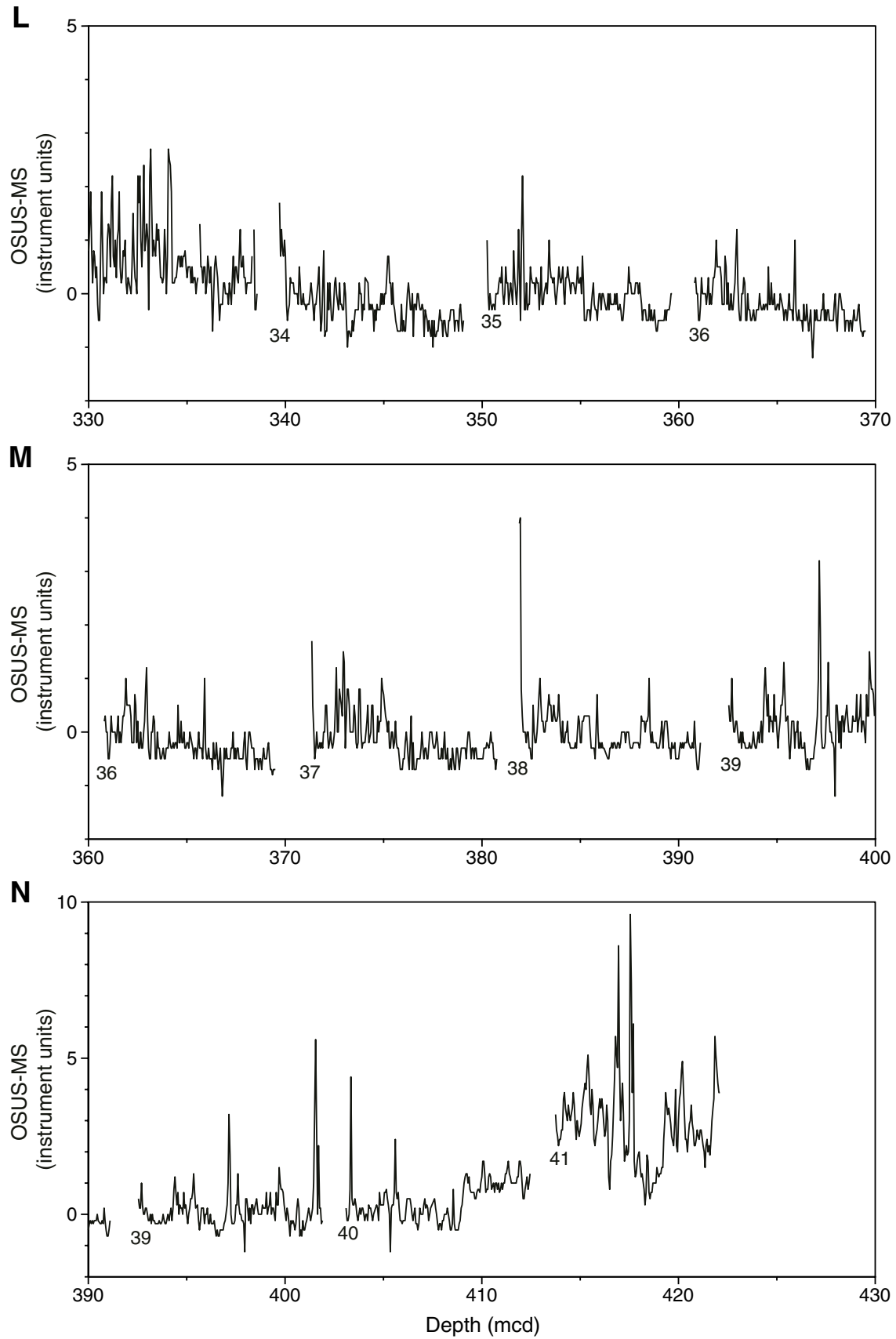


Figure F10. Smoothed (9-point Gaussian) spliced records of natural gamma radiation (NGR), gamma ray attenuation (GRA) bulk density, and magnetic susceptibility (MST-MS) for Site 1238.

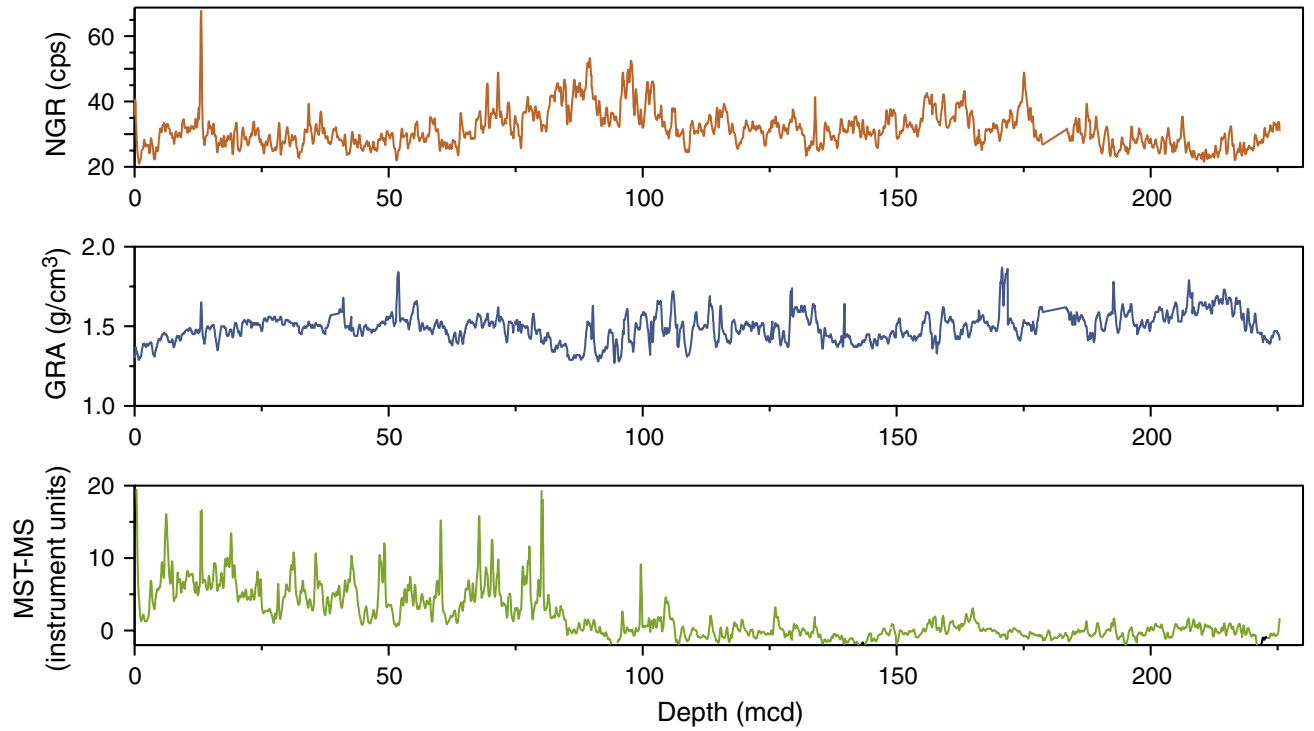


Figure F11. Smoothed (9-point Gaussian) spliced records of color reflectance from Site 1238: L^* , a^* , and b^* .

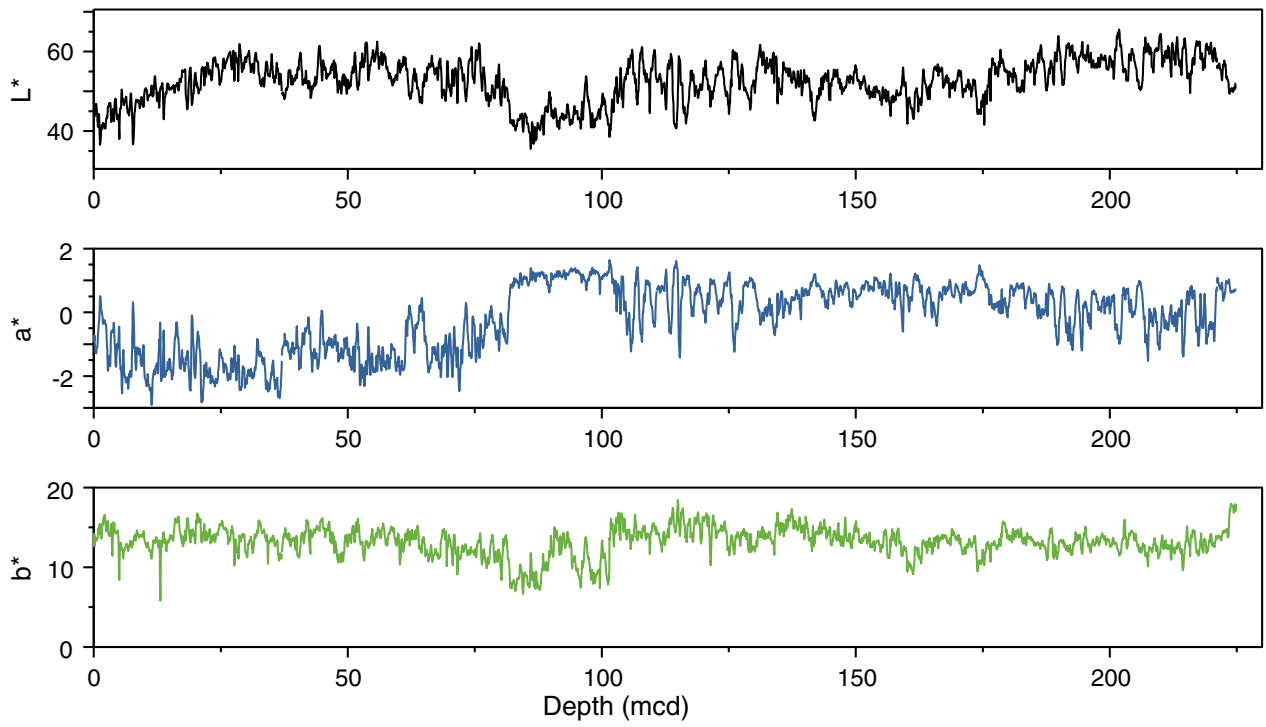


Figure F12. A comparison of the drillers depth (mbsf) and meters composite depth (mcd) scales in Holes 1238A through 1238C. On average, mcd is 10% greater than mbsf. The 1:1 (mbsf:mcd) line is also shown for comparison. GF = growth factor.

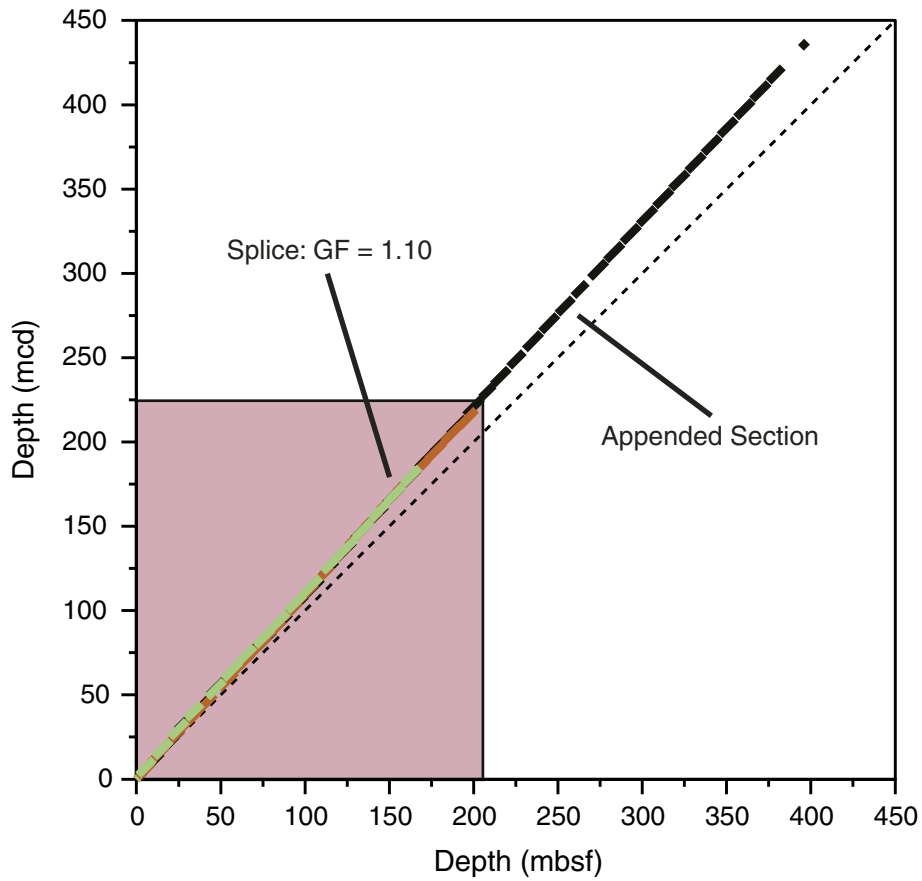


Figure F13. A comparison in Hole 1238A of downhole natural gamma radiation (HSGR) with whole-core natural gamma radiation (NGR) and of downhole log bulk density (RHOM) with hole core gamma ray attenuation (GRA) bulk density. Log and core data are placed on the equivalent log depth (eld) scale for comparison.

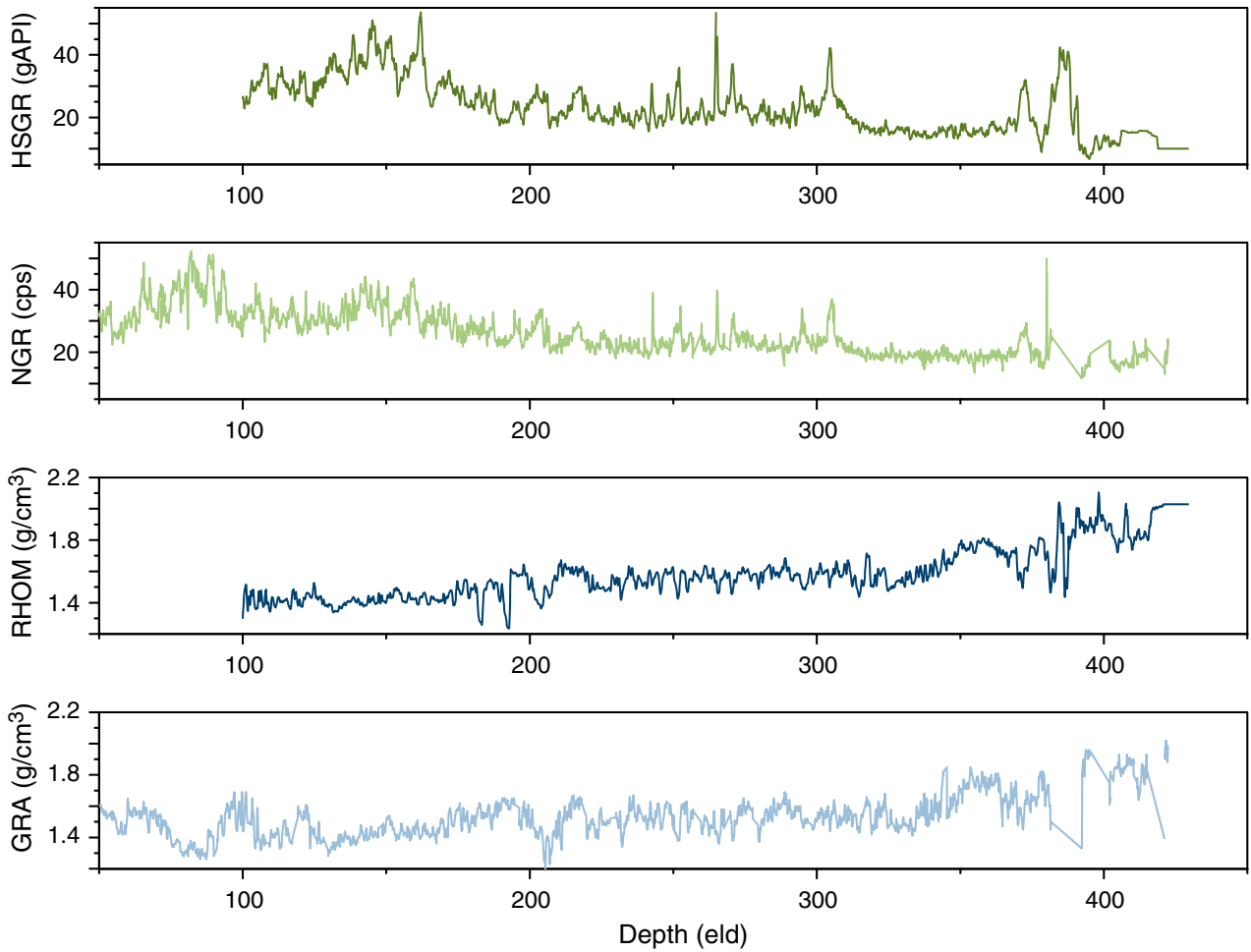


Figure F14. Core recovery, lithostratigraphic subunits, age, ash layers, magnetic susceptibility, gamma ray attenuation (GRA) bulk density, natural gamma radiation, color reflectance (L*), calcium carbonate (CaCO₃), and total organic carbon (TOC) of recovered sediments from Site 1238. Gray lines show the original data, and dark lines are 50-point smoothing averages of the original data. Diamonds denote the presence of ash layers. Black diamonds = ash layers identified in more than one hole, gray diamonds = ash layers found in a single hole. instr. = instrument.

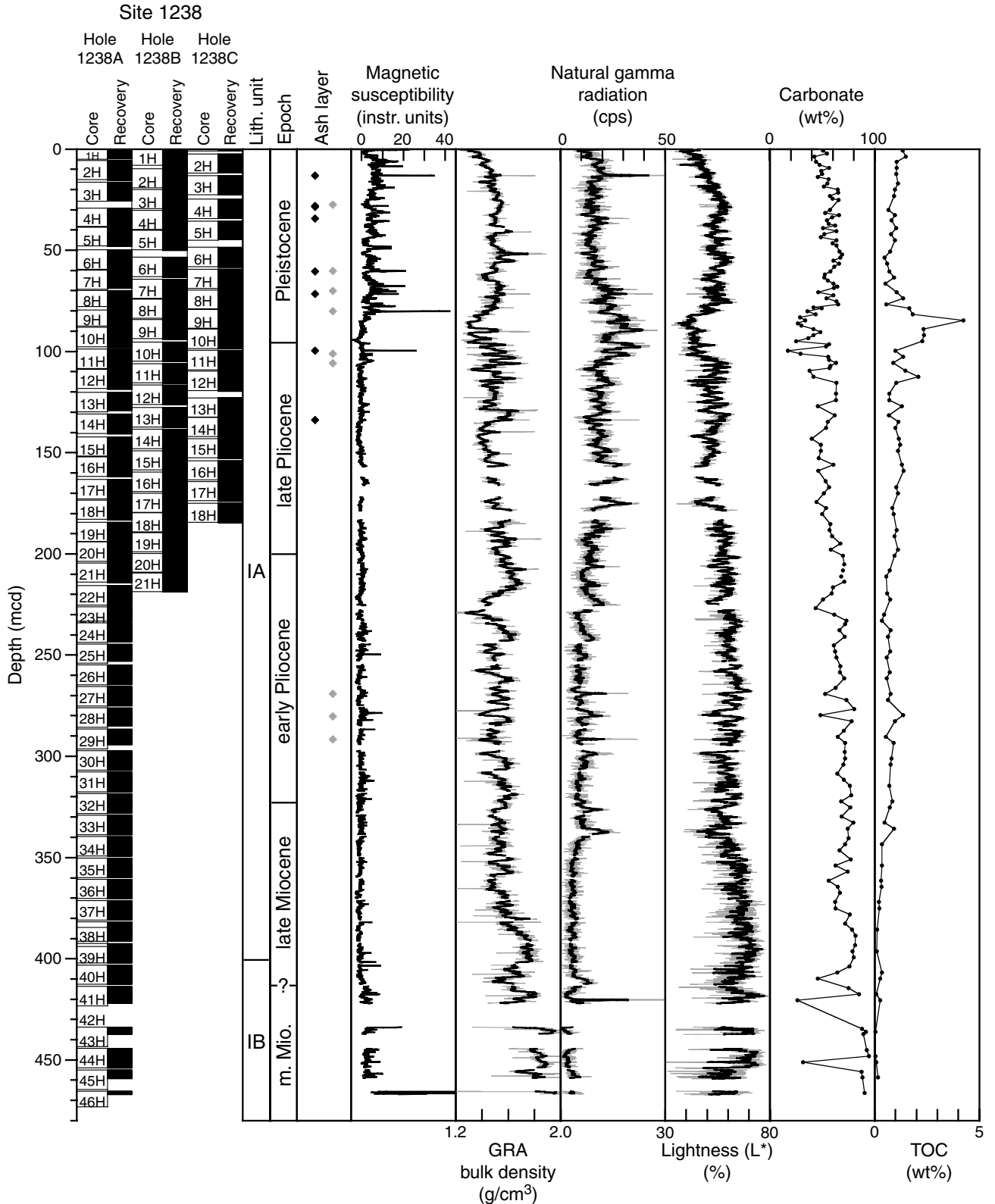


Figure F15. Major siliciclastic, biogenic, and authigenic components observed in Hole 1238 smear slides. Rad. = radiolarians, silicof. = silicoflagellates. TOC = total organic carbon, MS = magnetic susceptibility.

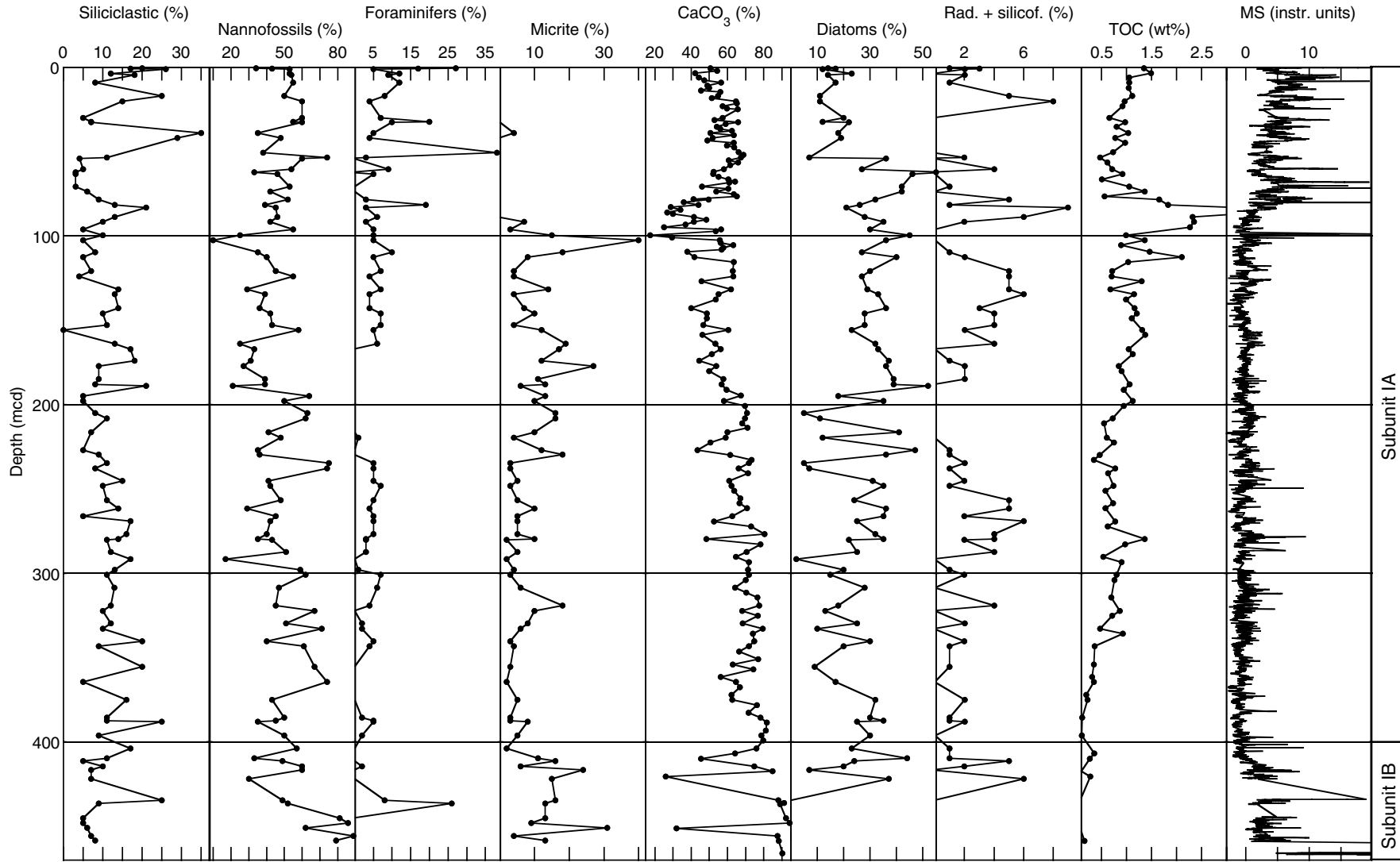


Figure F16. Vertical burrow in a bioturbated interval (202-1238A-20H-5, 54–75 cm).

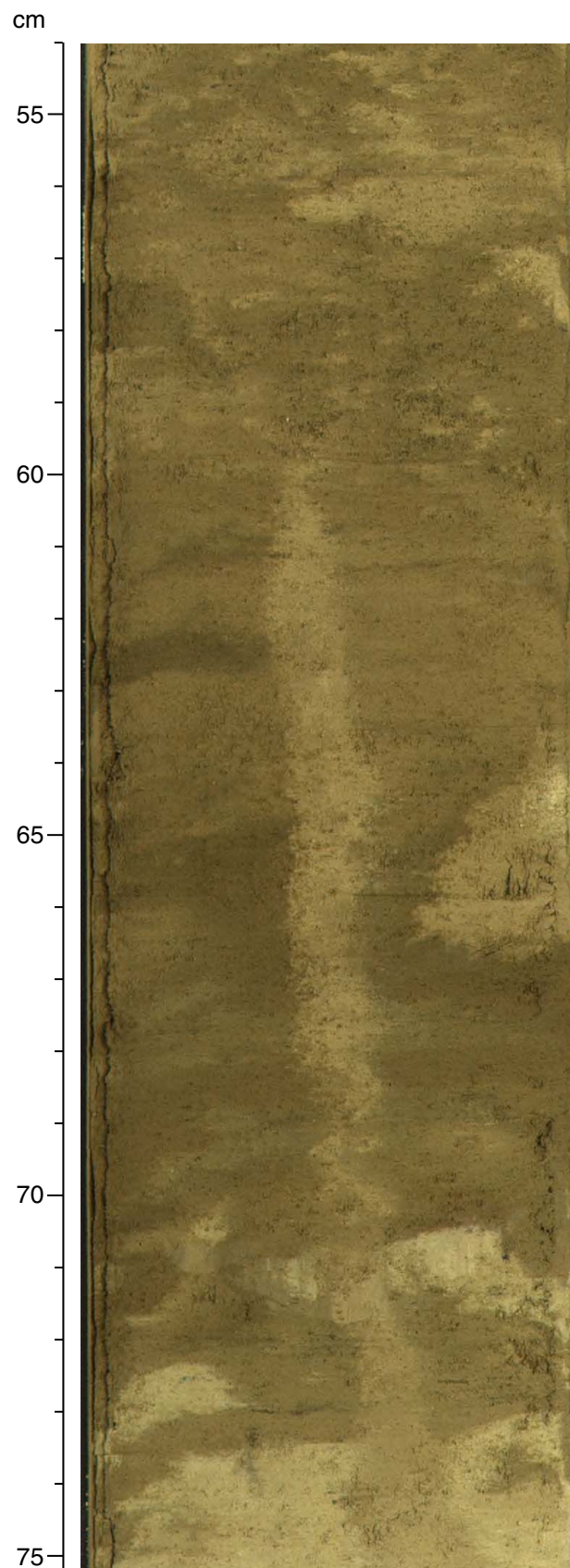


Figure F17. A. Photograph of dark and light banding in Core 202-1238A-28X (276–285 mcd). (Continued on next page.)

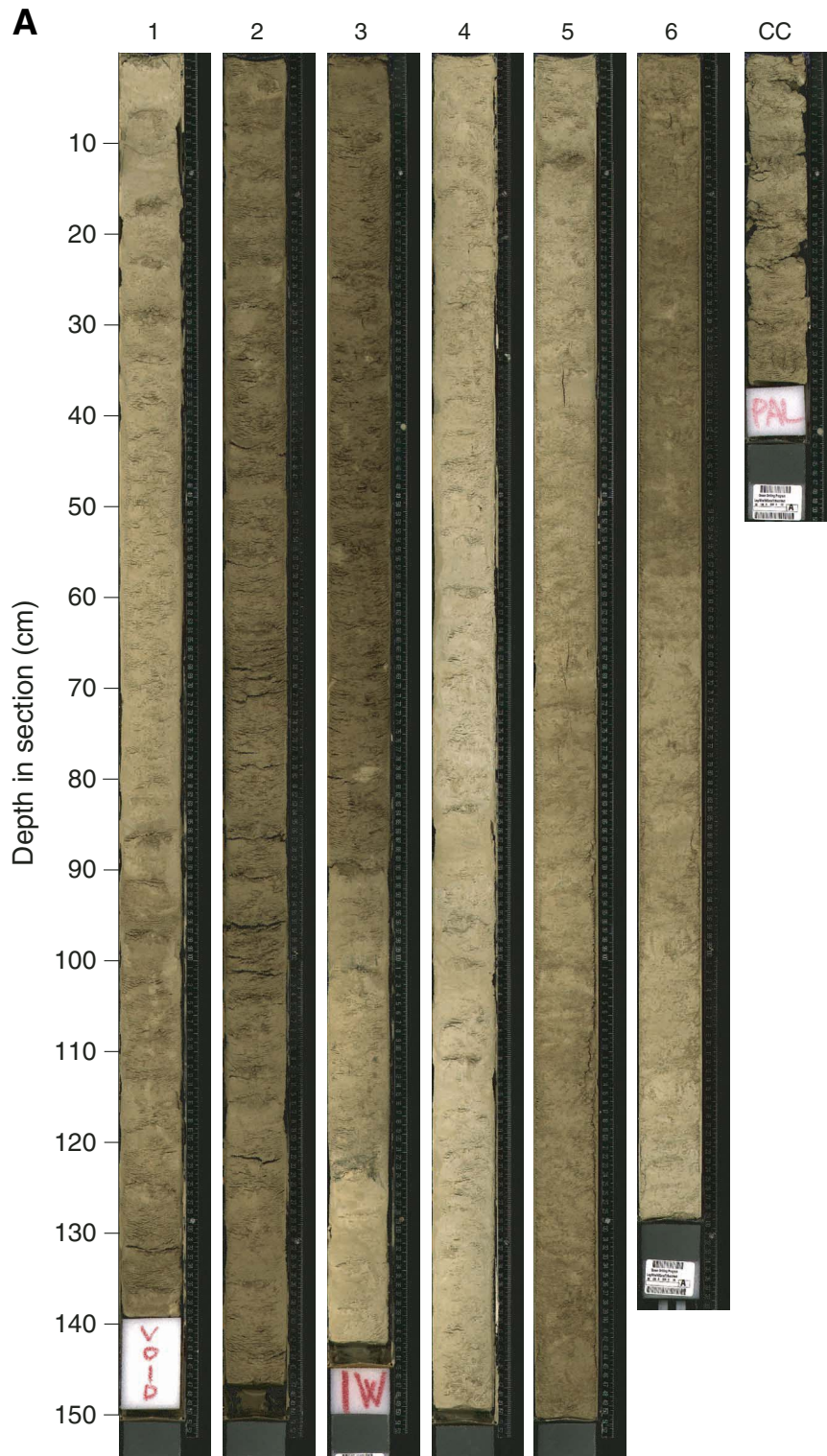


Figure F17 (continued). B. Corresponding physical properties and color measurements. Both dark and light banding show meter-scale cyclicity. GRA = gamma ray attenuation.

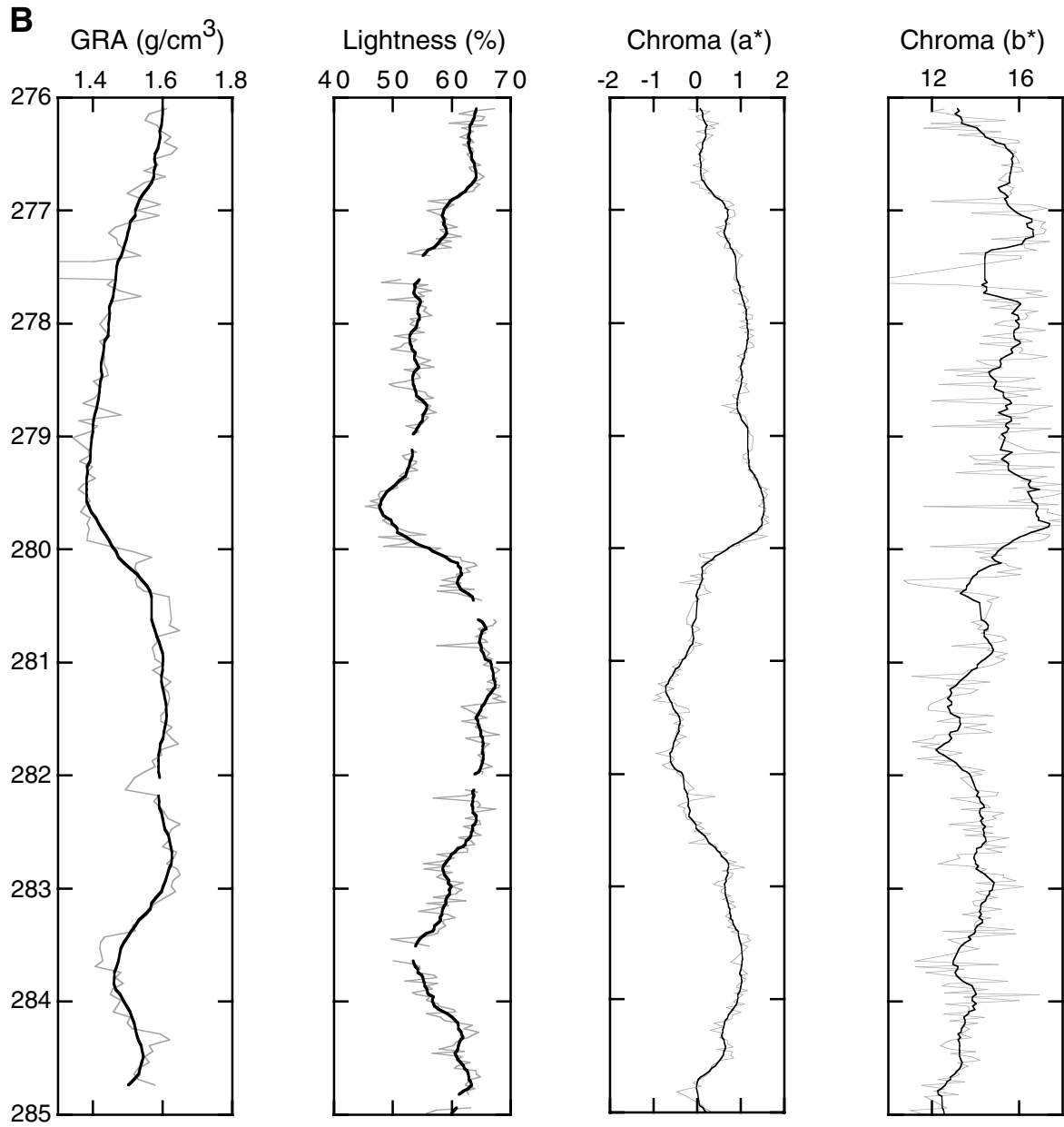


Figure F18. Proposed ash layer L (interval 202-1238B-2H-3, 22–43 cm).

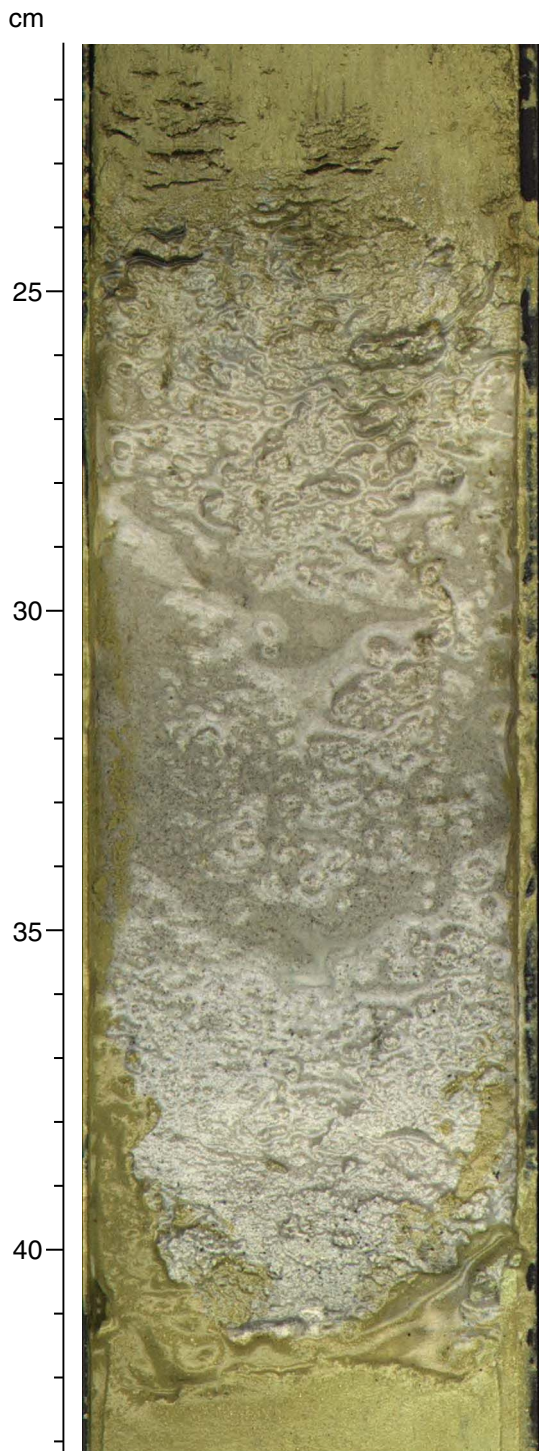


Figure F19. Physical properties measurements for Site 1238. A. Gamma ray attenuation (GRA) and moisture and density (MAD) bulk densities (BD) plotted with depth. B. Correlation between interpolated GRA and discretely measured MAD bulk density measurements. C. Porosity plotted with depth. D. Correlation between MAD bulk density and porosity. E. Grain density plotted with depth. F. Correlation between CaCO_3 and grain density.

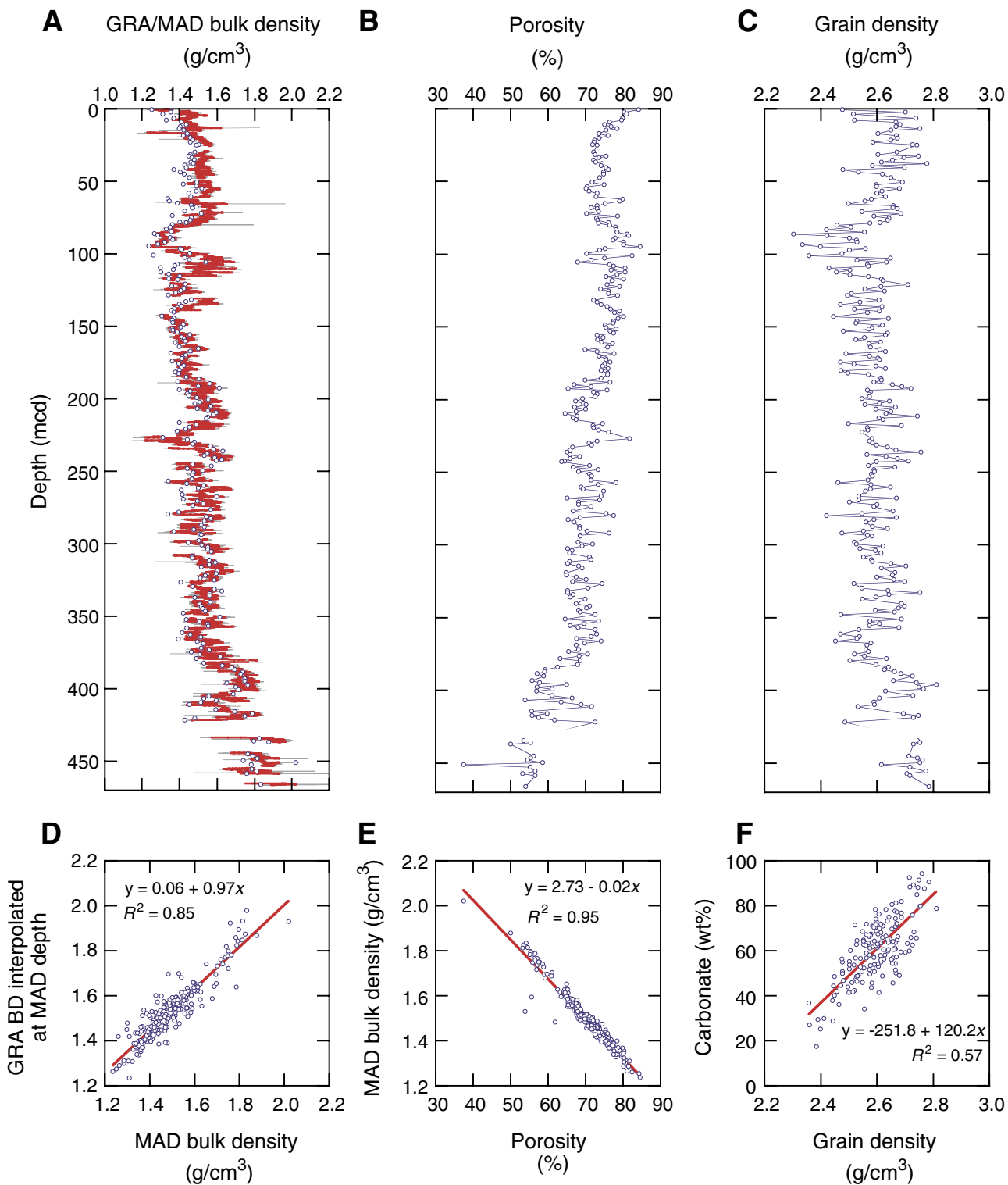


Figure F20. Color reflectance measurements for Site 1238. A. Chroma (a^*) plotted with depth. B. Chroma (b^*) plotted with depth. C. Color reflectance measurements from the entire sequence plotted in the a^* - b^* color plane. D. Color measurements from the dark interval from 80 to 102 mcd plotted in the a^* - b^* color plane.

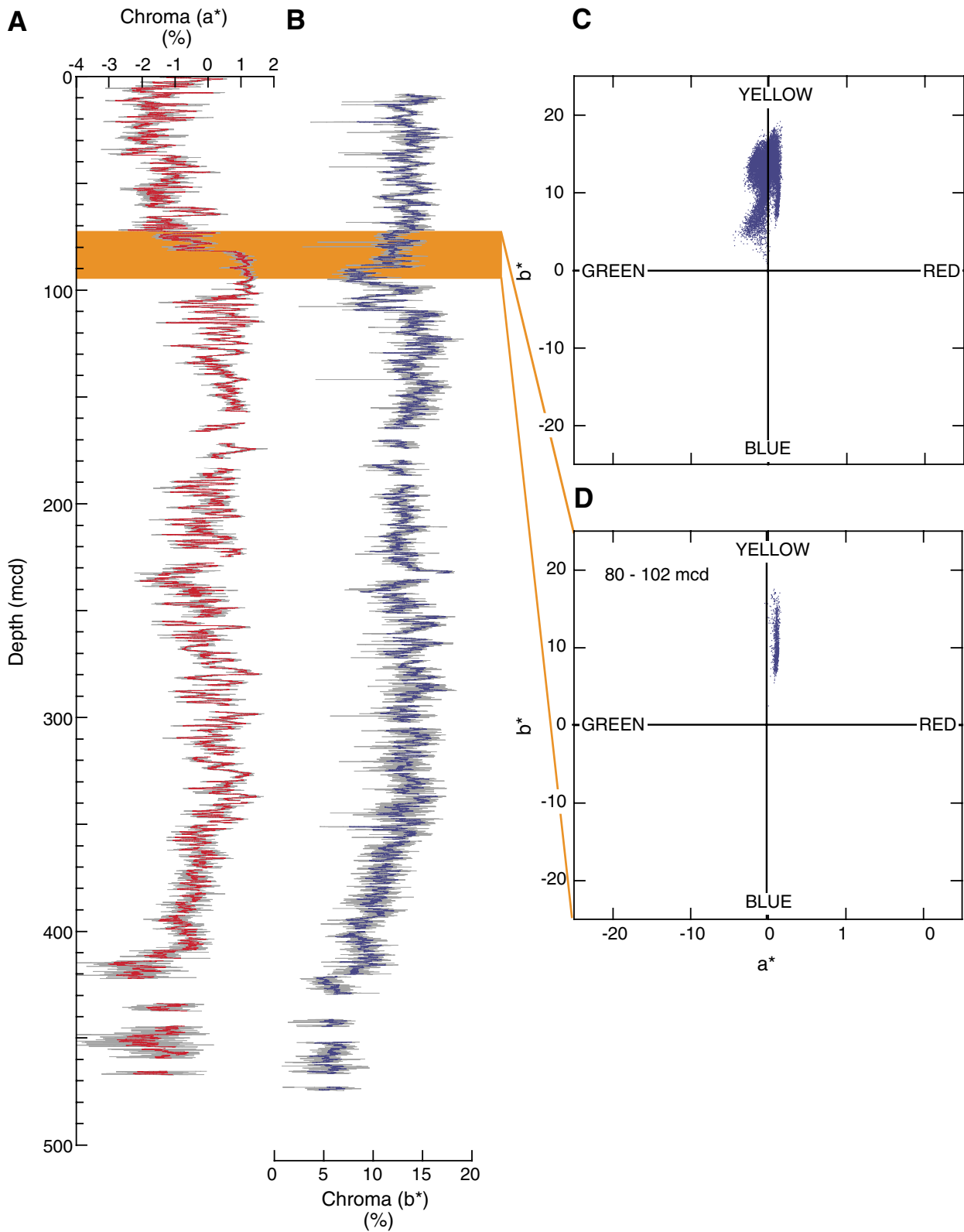


Figure F21. A. Sequential depth plot of raw reflectance spectra for Site 1238. Cool colors (blue) indicate low values, and warm colors (red) indicate high values. B. First derivatives of raw reflectance data with respect to wavelength. C. A representative reflectance spectrum exhibits absorption features typical of organic pigments at 410, 510, 560, and 650 nm. D. Inflection points of the first derivative of the reflectance spectrum indicate the location of the same absorption features and are easily distinguishable on the sequential plot of the first derivatives. E. The normalized absorption feature at 650 nm, relative to reflectances at 630 and 700 nm and normalized to a measure of the general slope of the spectrum (i.e., $\text{Depth}_{650} = \{R_{630} + [3/7 \times (R_{700} - R_{630}) - R_{650}]\} / [R_{700} - R_{400}]$), is plotted with depth as a proxy for abundance of chlorins.

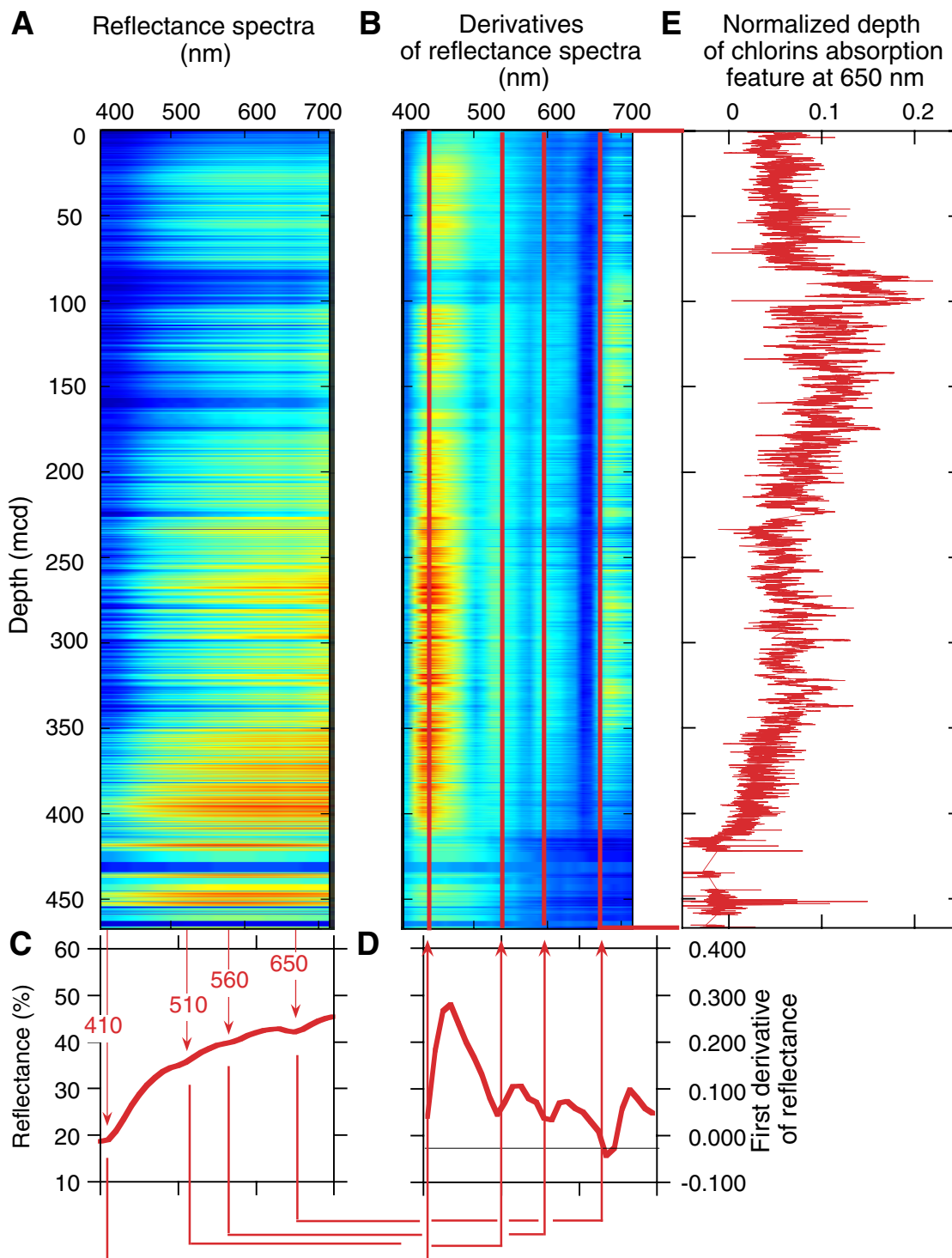


Figure F22. A. Close-up photograph of chalk (interval 202-1238A-42X-1, 0–34 cm). B. Diffractogram from XRD measurement of a chalk sample (Sample 202-1238B-42X-1, 23–24 cm). The major peaks correspond to calcite, biogenic opal, and quartz.

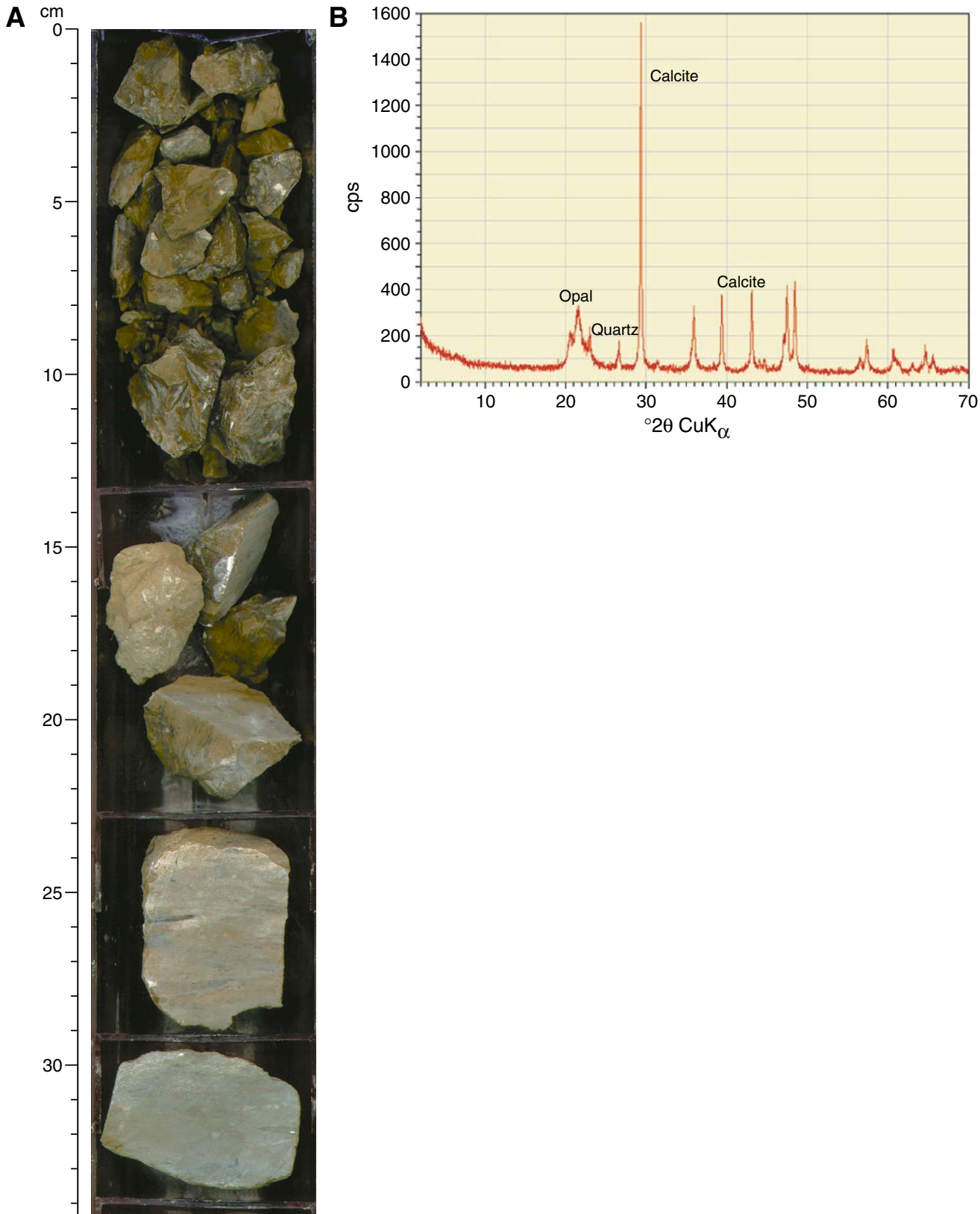


Figure F23. Close-up photograph of chalk interbedded with chert horizons (at 60–62 and 65–67 cm) from interval 202-1238-46X-1, 50–75 cm.

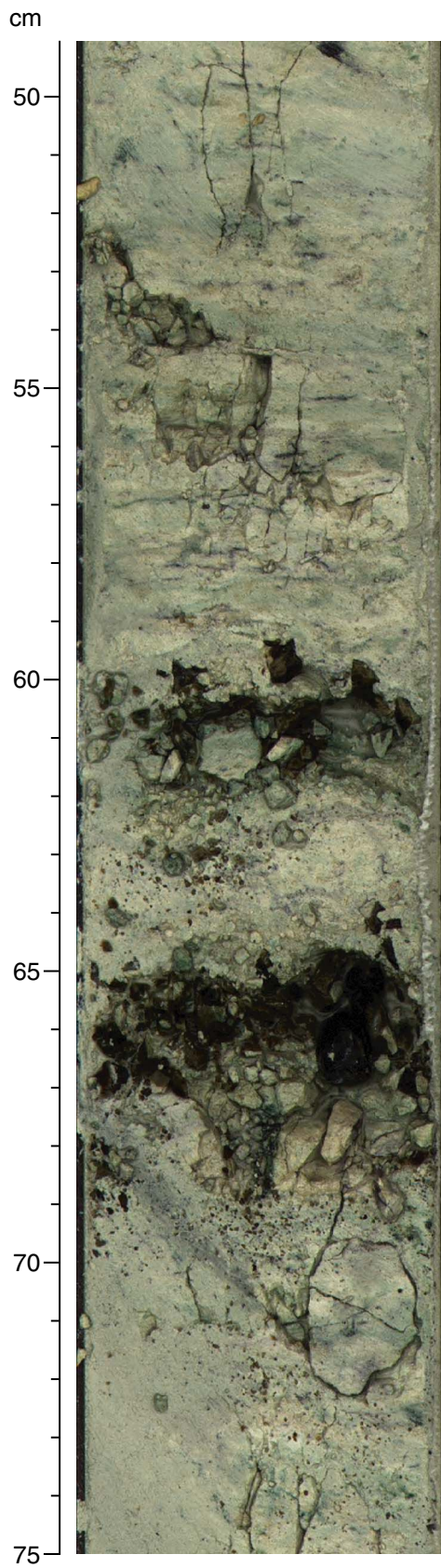


Figure F24. Preliminary time series analysis results from Site 1238 based on the biostratigraphic age model. **A, B.** Time series and corresponding spectra from 0 to 1 Ma (assuming a linear sedimentation rate between 0.0 and 58.2 mcd, as inferred from one biostratigraphic datum in this interval) of gamma ray attenuation (GRA) bulk density. **C, D.** Magnetic susceptibility. **E, F.** Lightness. The concentration of variance near the known orbital frequencies suggests that meter-scale lithologic banding is associated with orbital-scale climate variability. Gray bands = orbital frequencies.

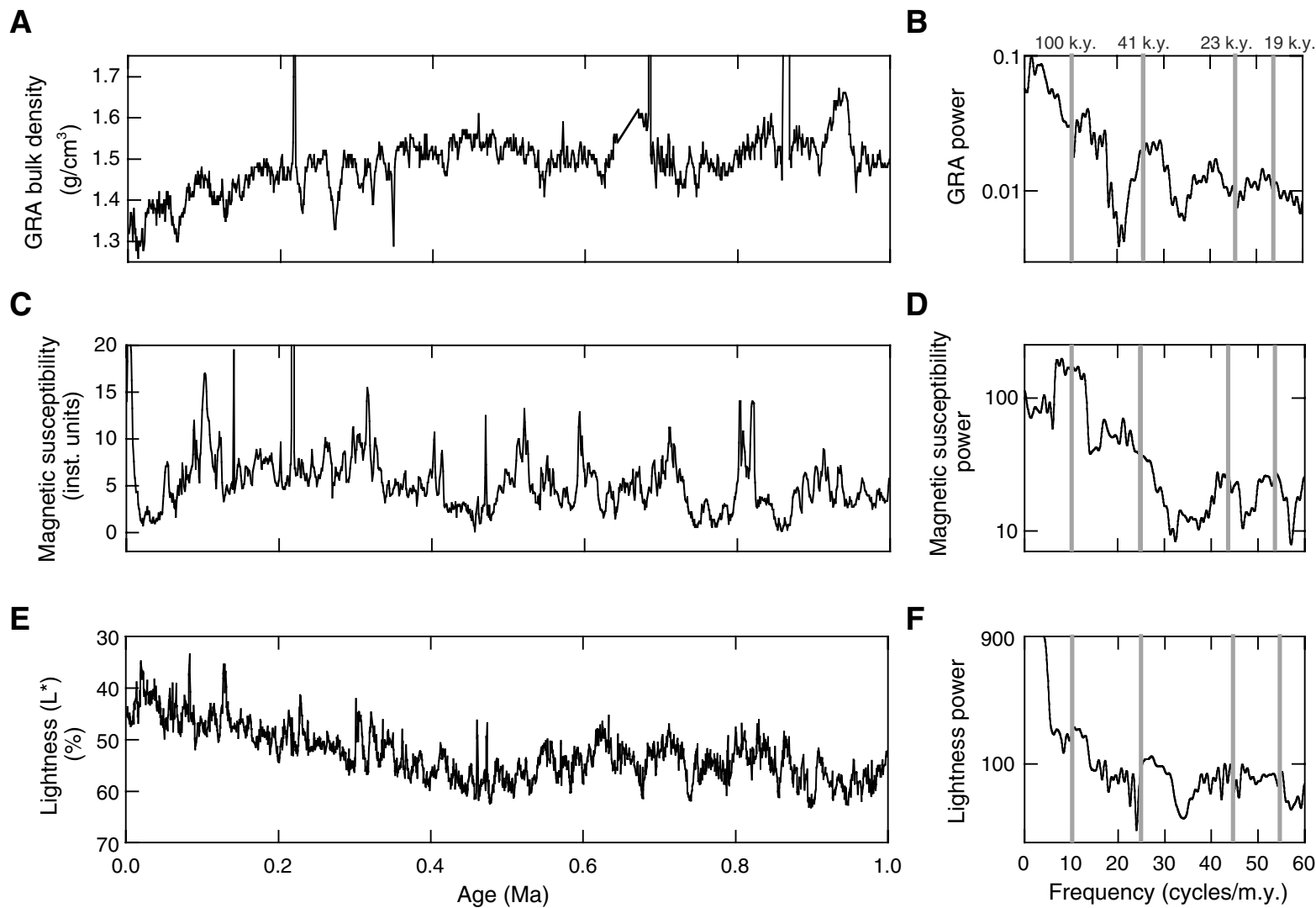


Figure F25. Core recovery, calcareous nannofossils and foraminifer abundance, benthic foraminifer percentage of total foraminifers, and diatom abundance at Hole 1238A (smoothed lines). R = rare, F = few, C = common, A = abundant, VA = very abundant.

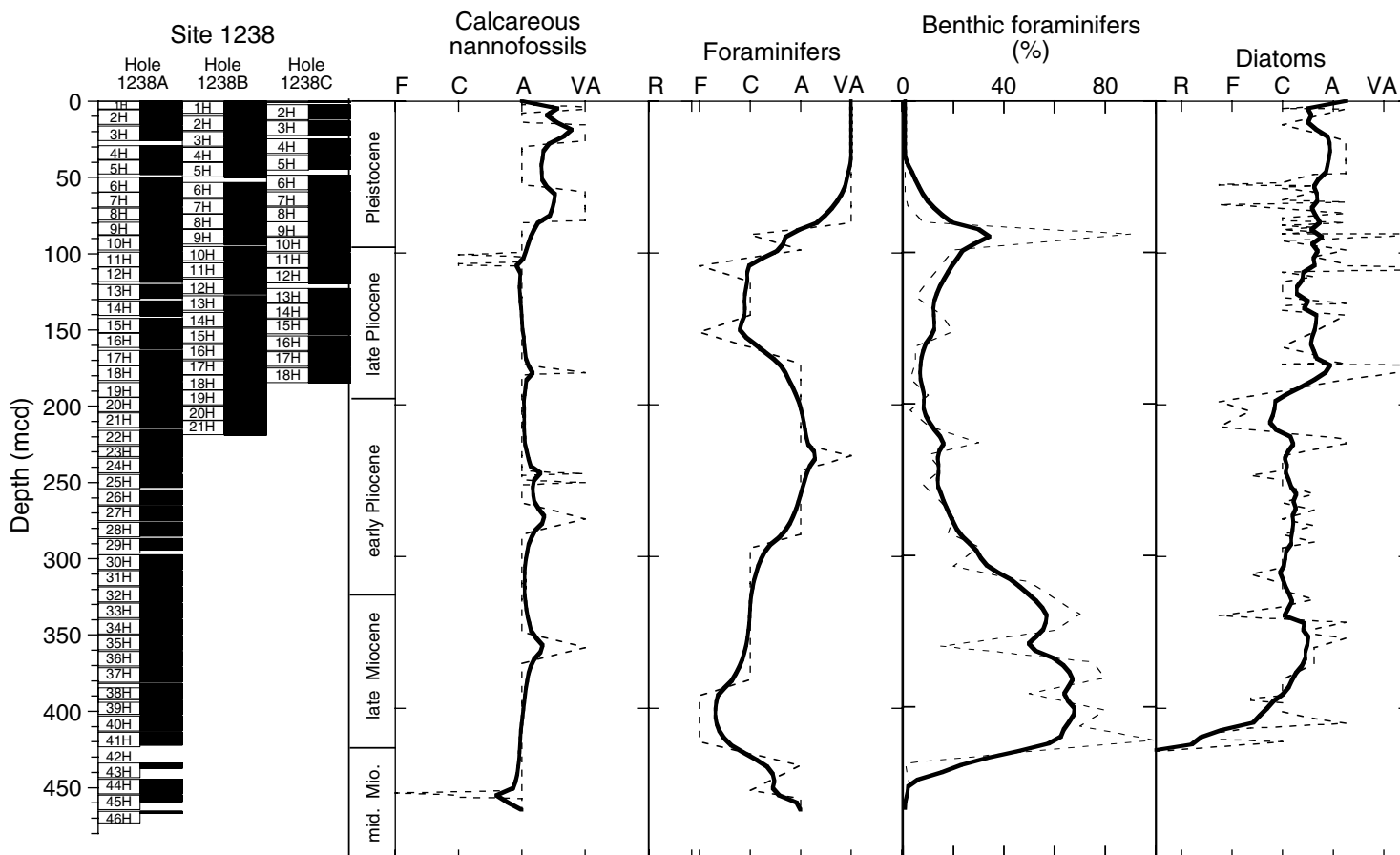


Figure F26. Natural remanent magnetization (NRM) intensity before (top) and after AF demagnetization at 25 mT (bottom) for Hole 1238A. Notice the greater variability below 200 mcd where drilling changed from advanced piston corer (APC) to extended core barrel (XCB) coring.

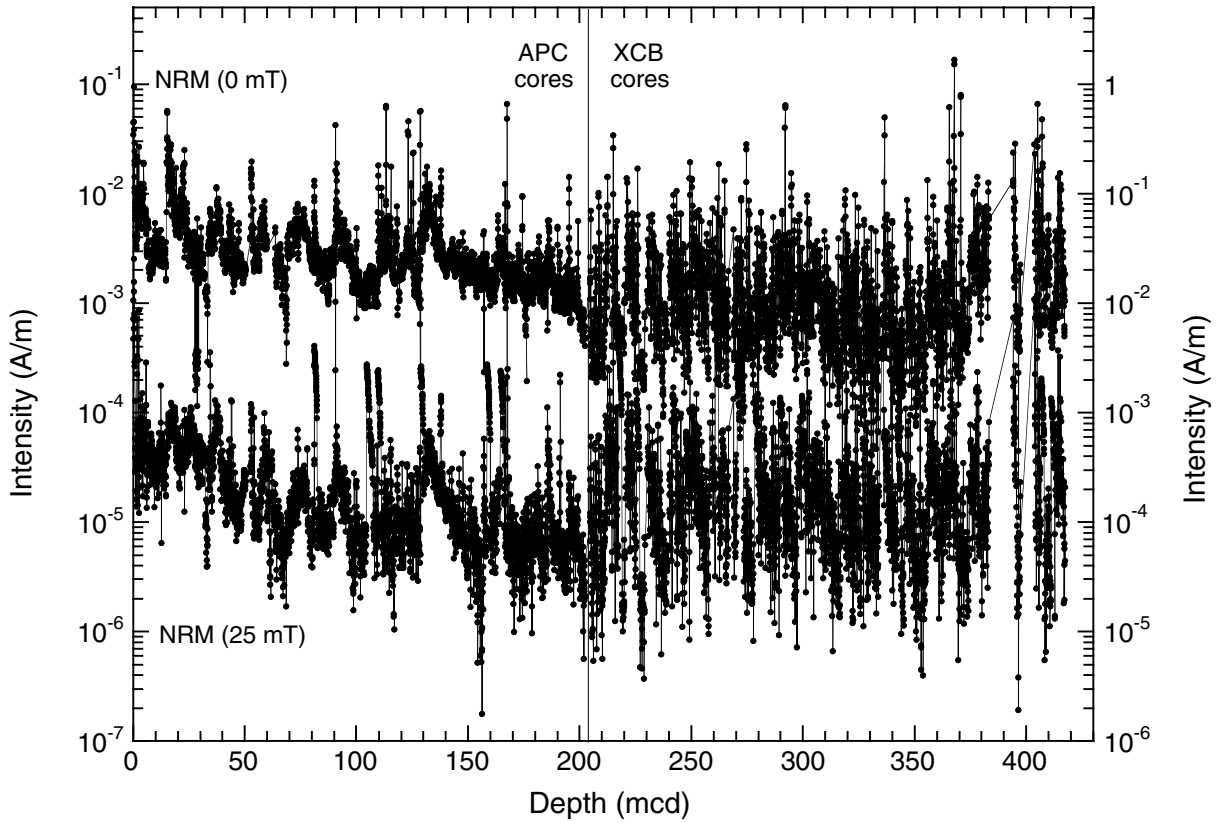


Figure F27. Hole 1238A inclinations and declinations after AF demagnetization at 25 mT. Inclinations are near the expected axial dipole expected values (-3.7°), and declinations show within core correlation only in the uppermost 40 mcd. No clear polarity stratigraphy can be discerned.

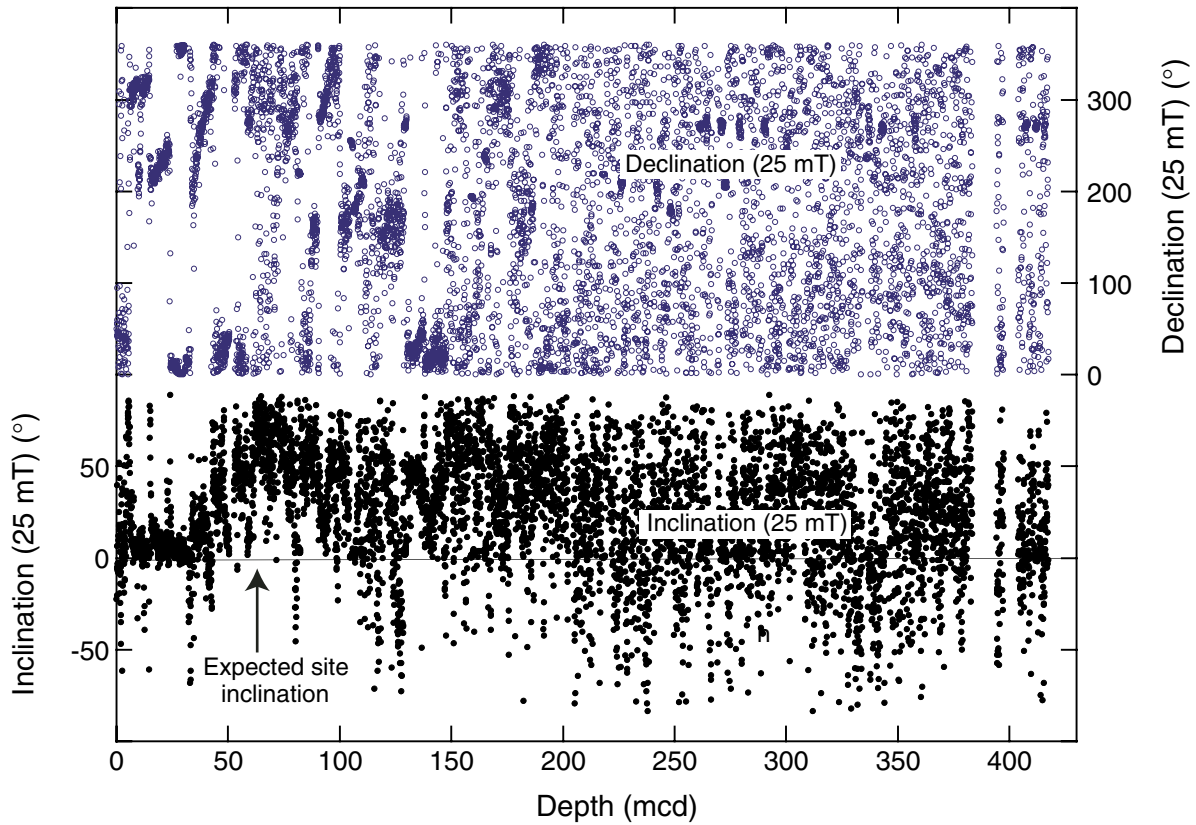


Figure F28. Inclination after AF demagnetization at 25 mT and NRM intensity for the uppermost 70 mcd of Hole 1238A. Dashed lines indicate the boundaries between individual cores.

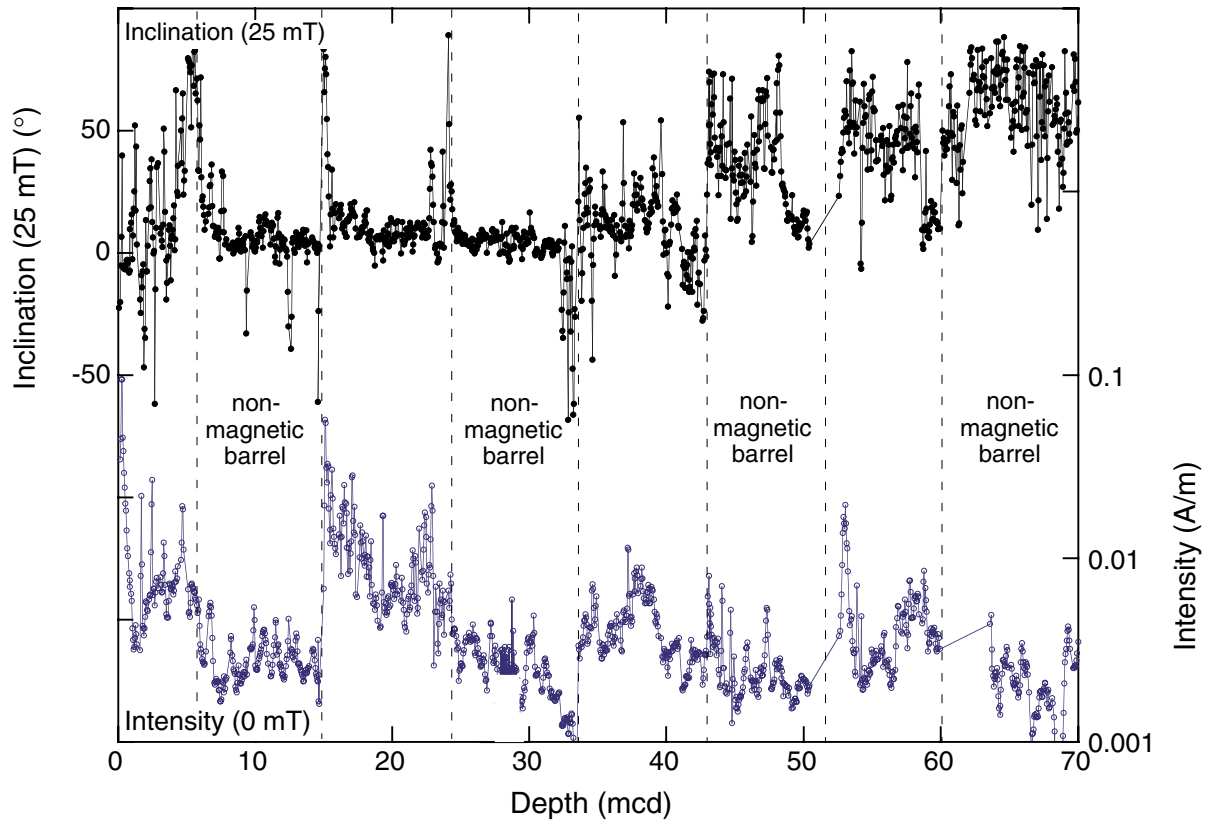


Figure F29. Natural remanent magnetization (NRM) intensity before (top) and after AF demagnetization at 25 mT (bottom) for the upper 10 mcd of Hole 1238A. Notice the large decrease in intensity with the first meter.

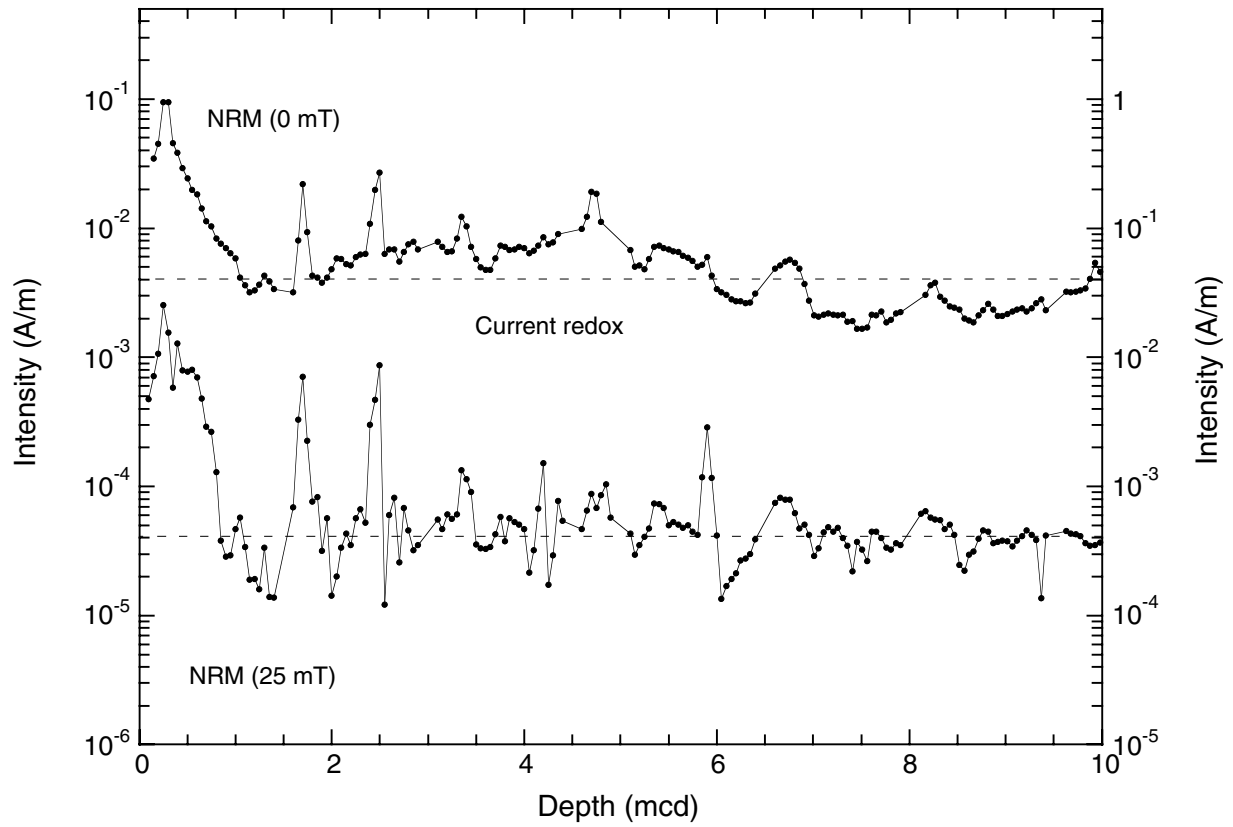


Figure F30. Headspace methane (C_1) concentrations and C_1/C_2 ratios in sediments vs. depth for Hole 1238A.

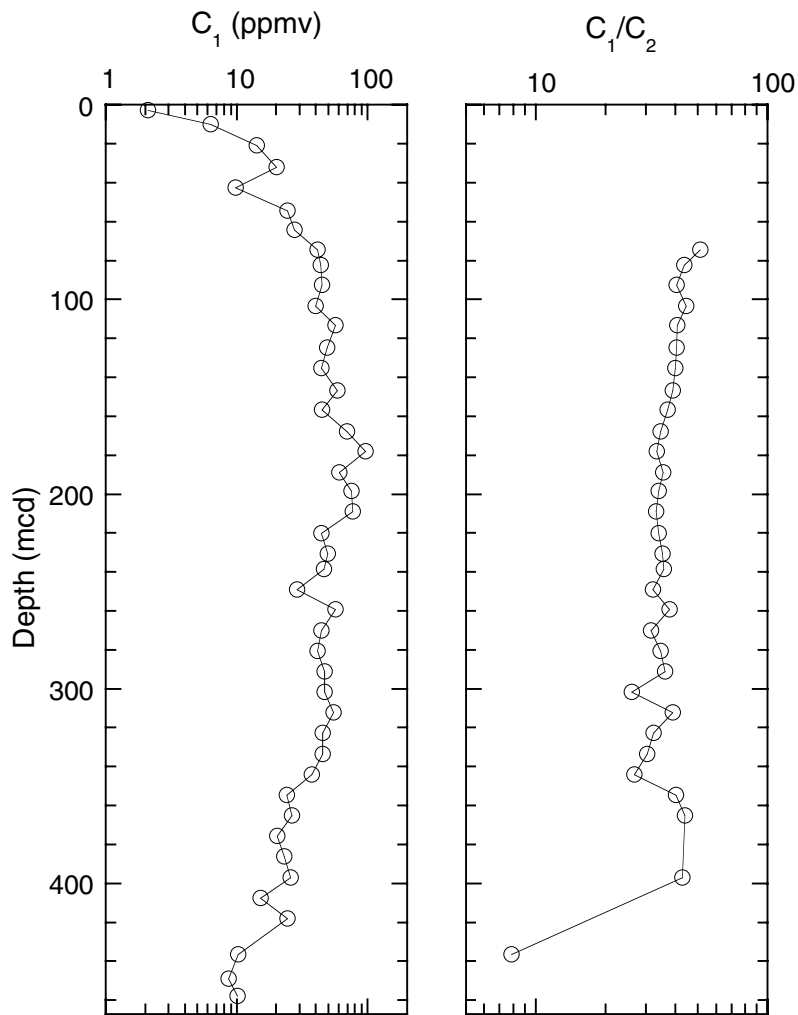


Figure F31. Interstitial water geochemical data for Site 1238. Open squares = calcium concentrations. The horizontal line indicates the lithologic subunit boundary (see "Lithostratigraphy," p. 6). Values below the detection limit (0.01 μM for manganese, 0.2 μM for iron, 1 μM for phosphate, and 0.4 mM for ammonium) are plotted at zero. Note that the blank correction for barium (0.9 μM) was significant compared to total measured concentrations, so this profile should be interpreted with caution.

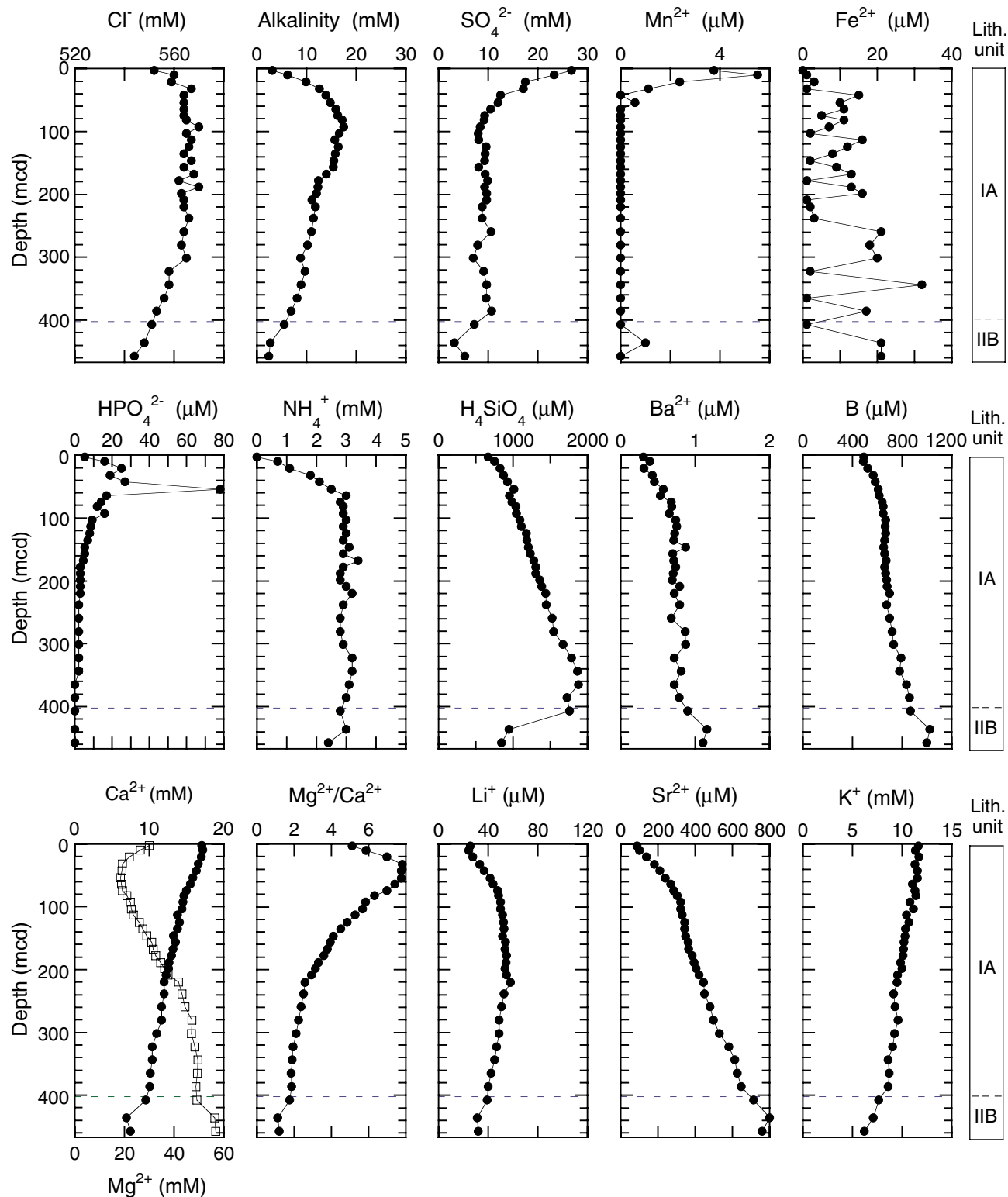


Figure F32. Calcium carbonate (CaCO_3), total organic carbon (TOC), and total nitrogen (TN) concentrations, and TOC/TN ratios in sediments vs. depth for Hole 1238A.

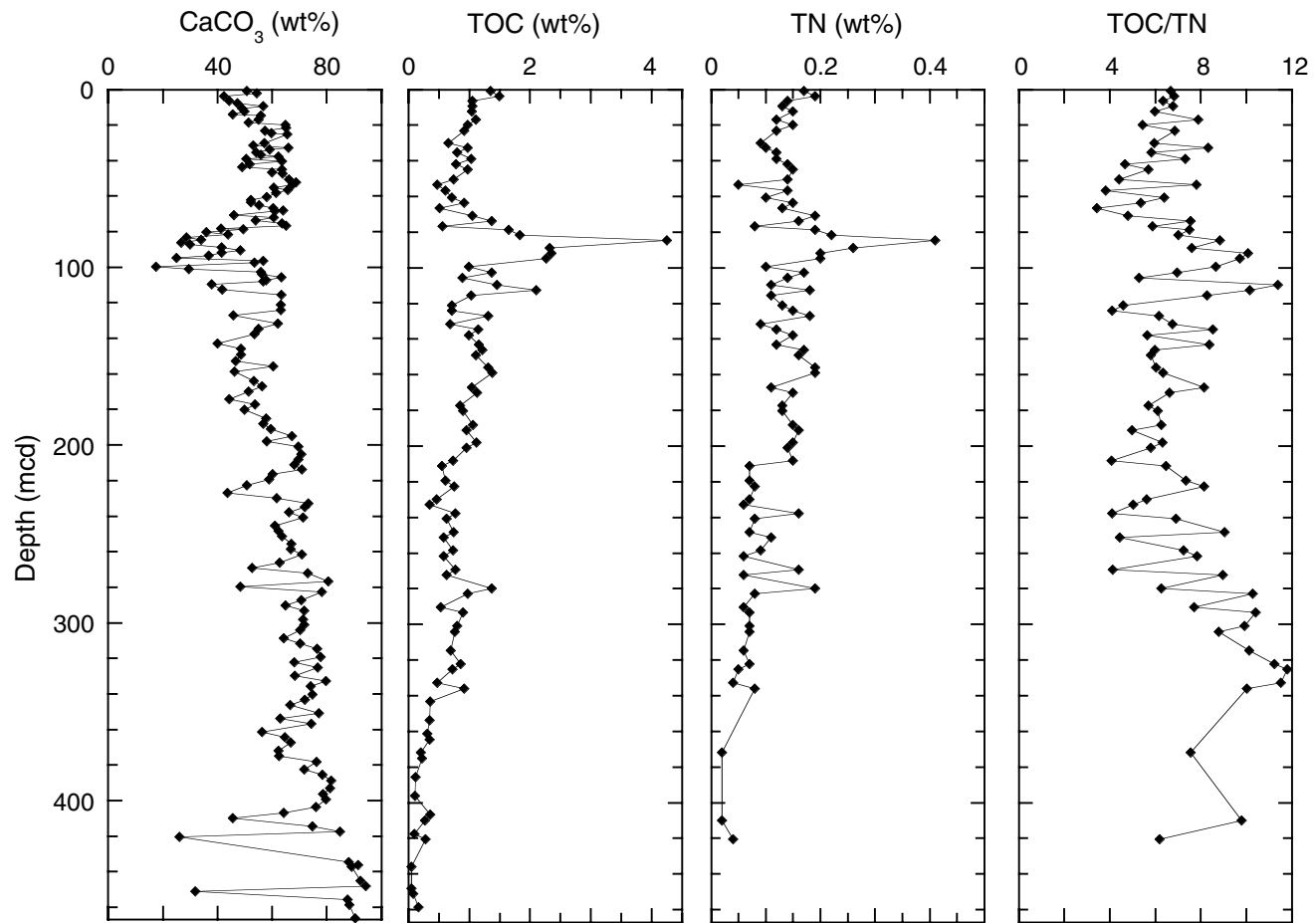


Figure F33. Calcium carbonate (CaCO_3) vs. total organic carbon (TOC) concentrations, and total nitrogen (TN) vs. TOC contents in sediments of Hole 1238B.

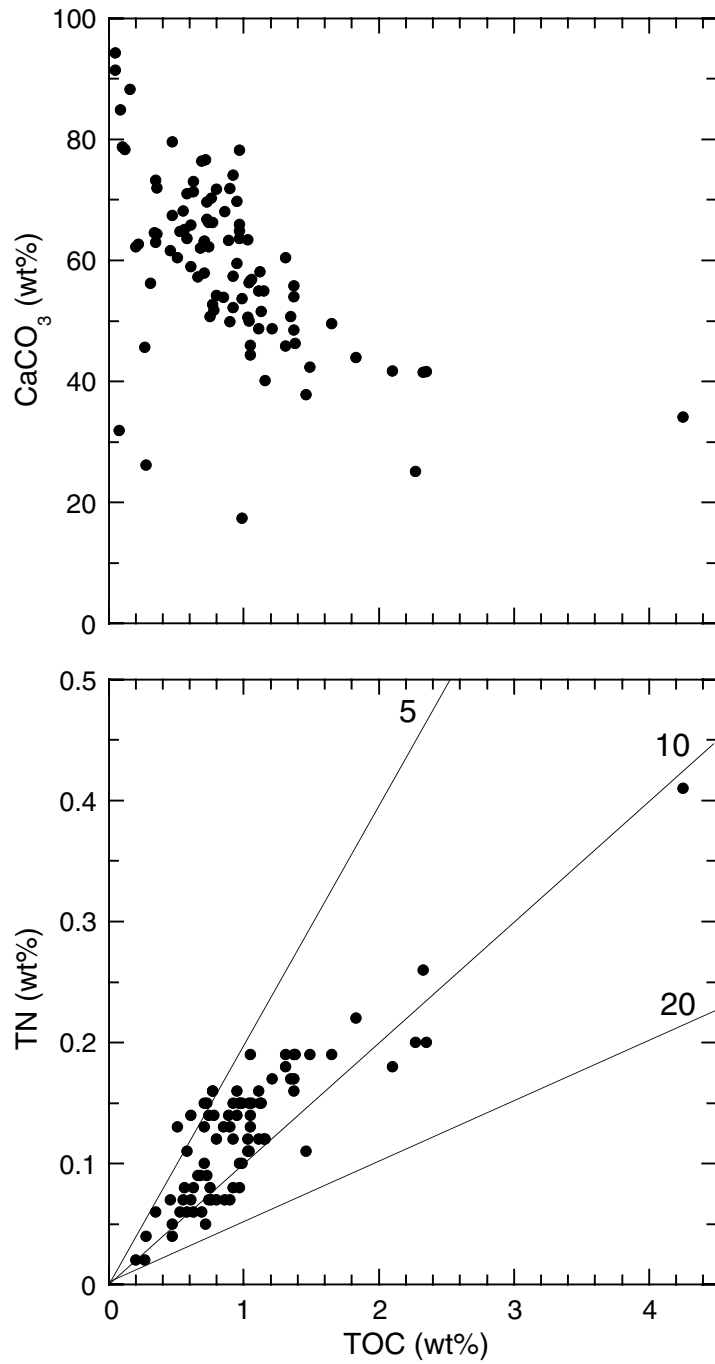


Figure F34. Details of the logging tool string deployments in Hole 1238A. Triple combo = triple combination tool, MGT = Multi-Sensor Spectral Gamma Ray Tool, FMS = Formation MicroScanner.

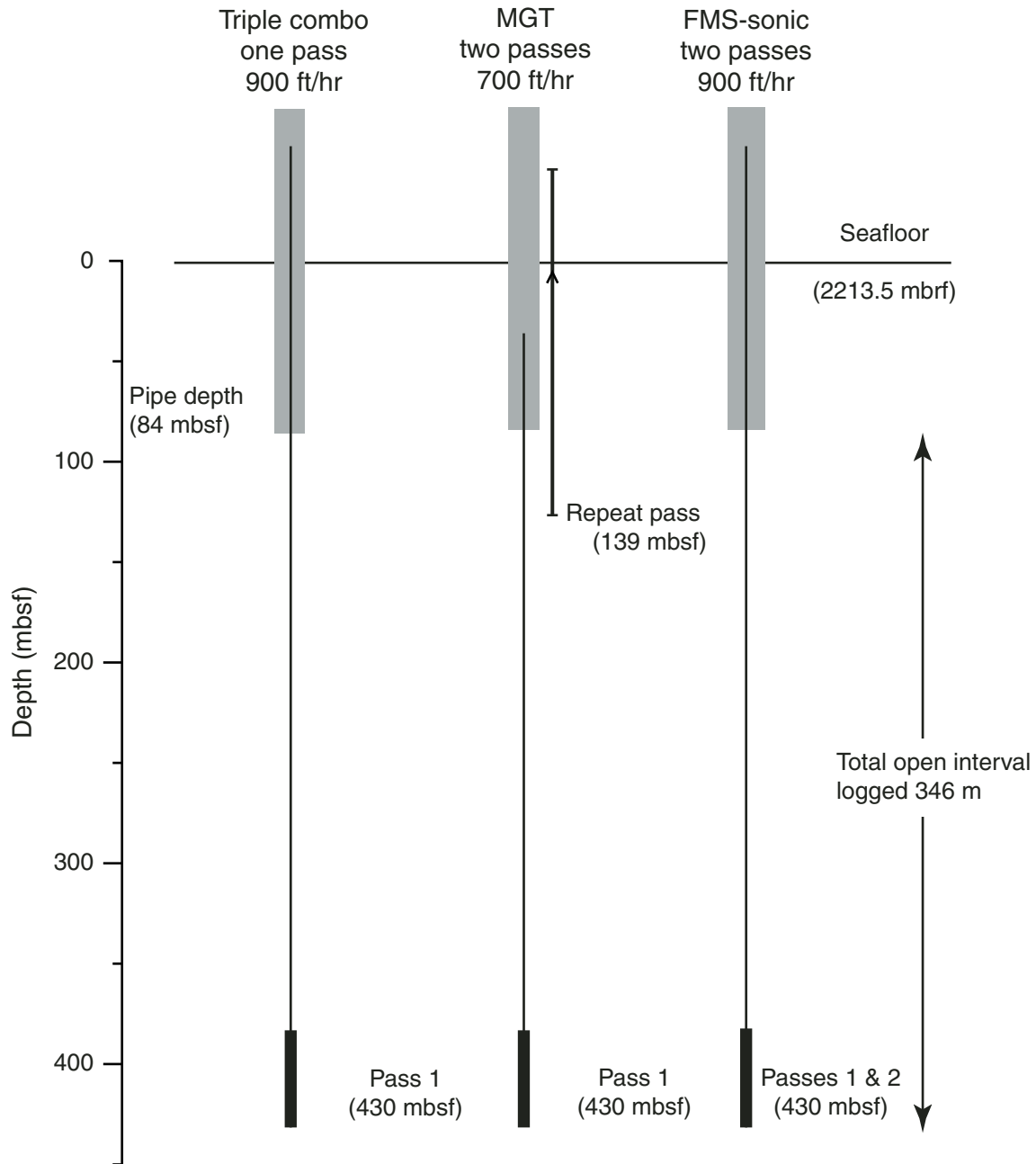


Figure F35. Caliper, deviation, gamma ray, and high-resolution gamma ray records for Hole 1238A. MGT = Multi-Sensor Spectral Gamma Ray Tool, gAPI = American Petroleum Institute gamma ray units.

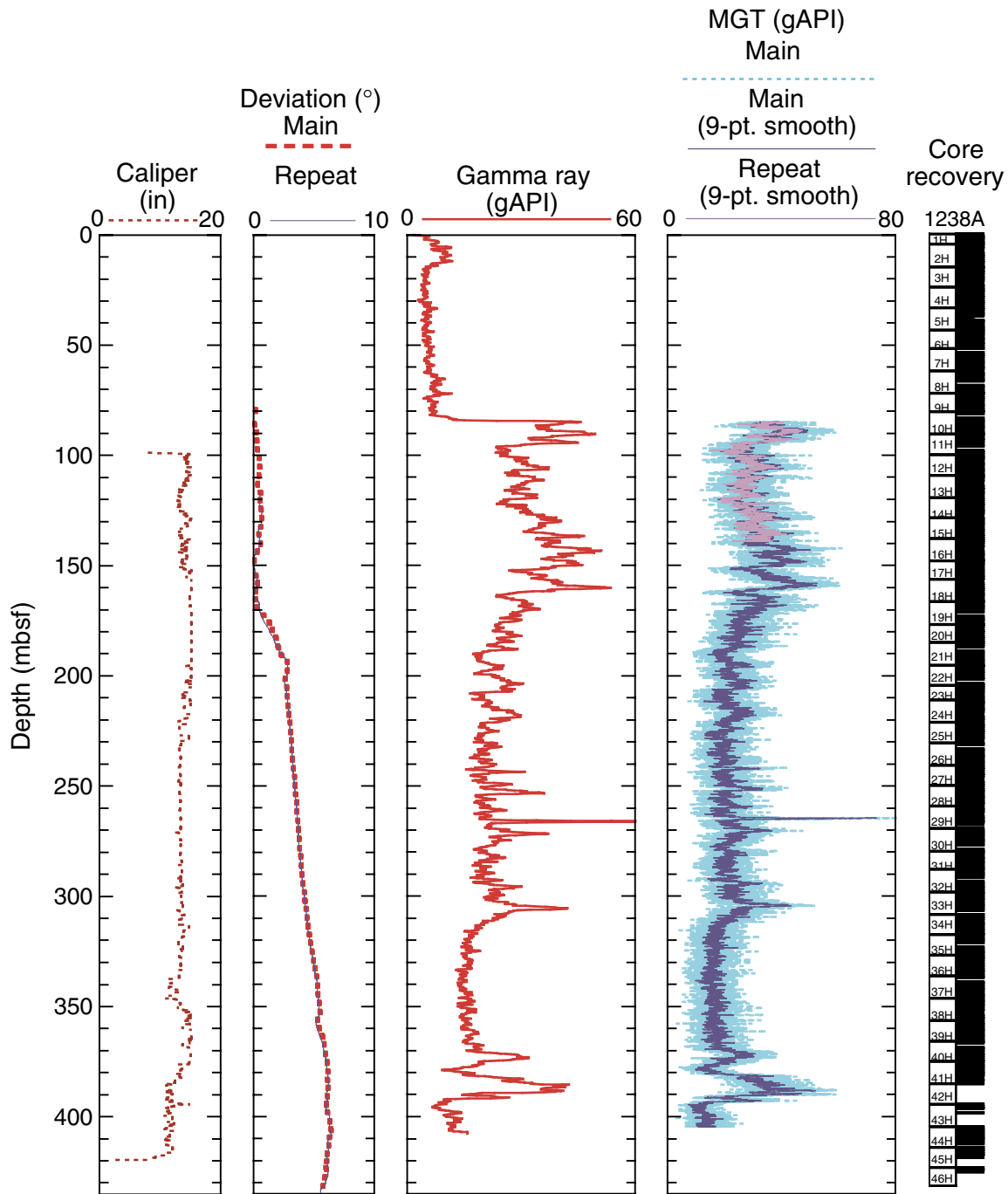


Figure F36. Density, porosity, sonic velocity, and resistivity data for Hole 1238A. Orange dashed lines = logging unit boundaries.

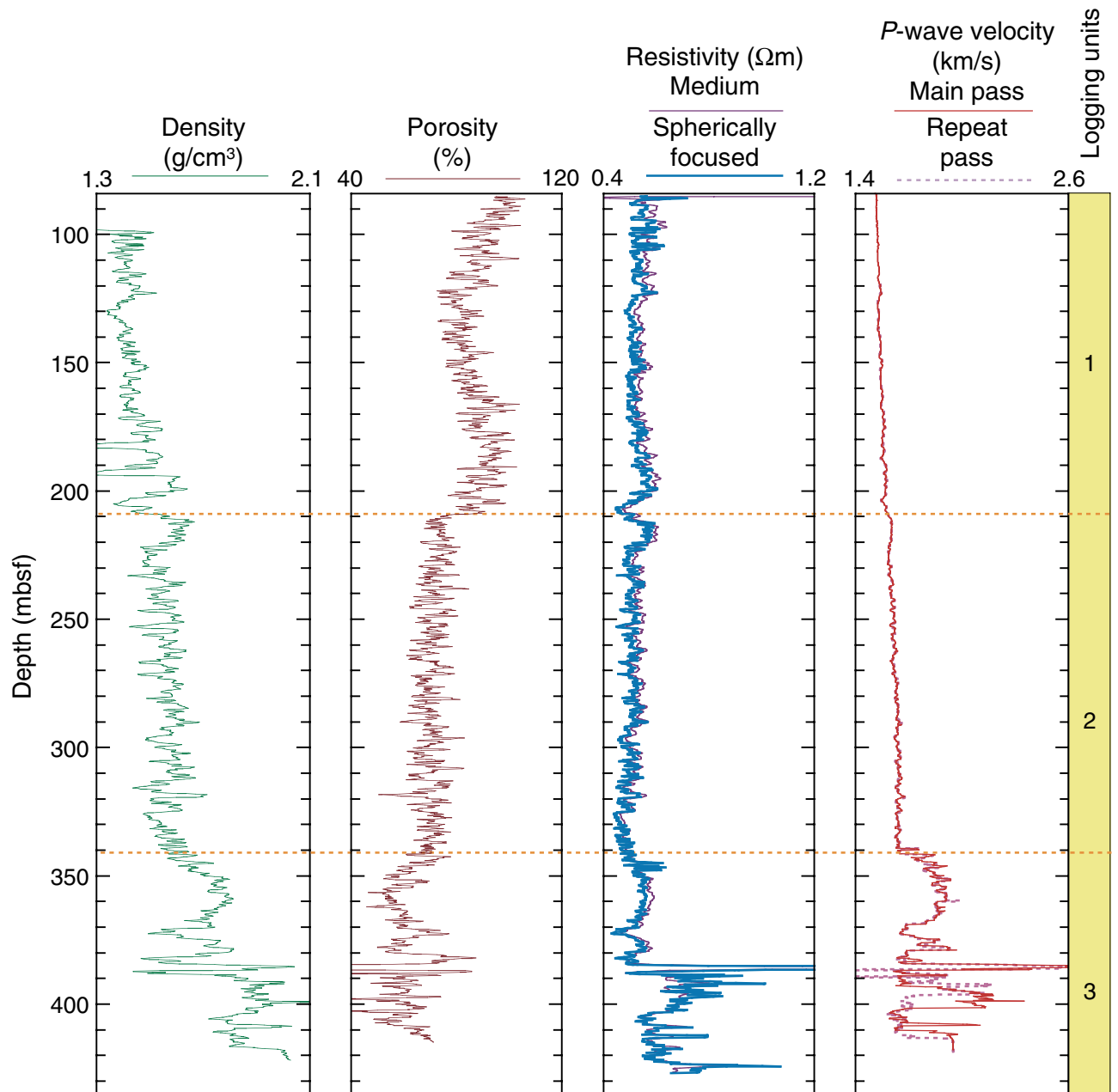


Figure F37. Total gamma ray and spectral gamma ray data for Hole 1238A. HCGR = computed gamma ray headspace, HSGR = total spectral gamma ray, gAPI = American Petroleum Institute gamma ray units.

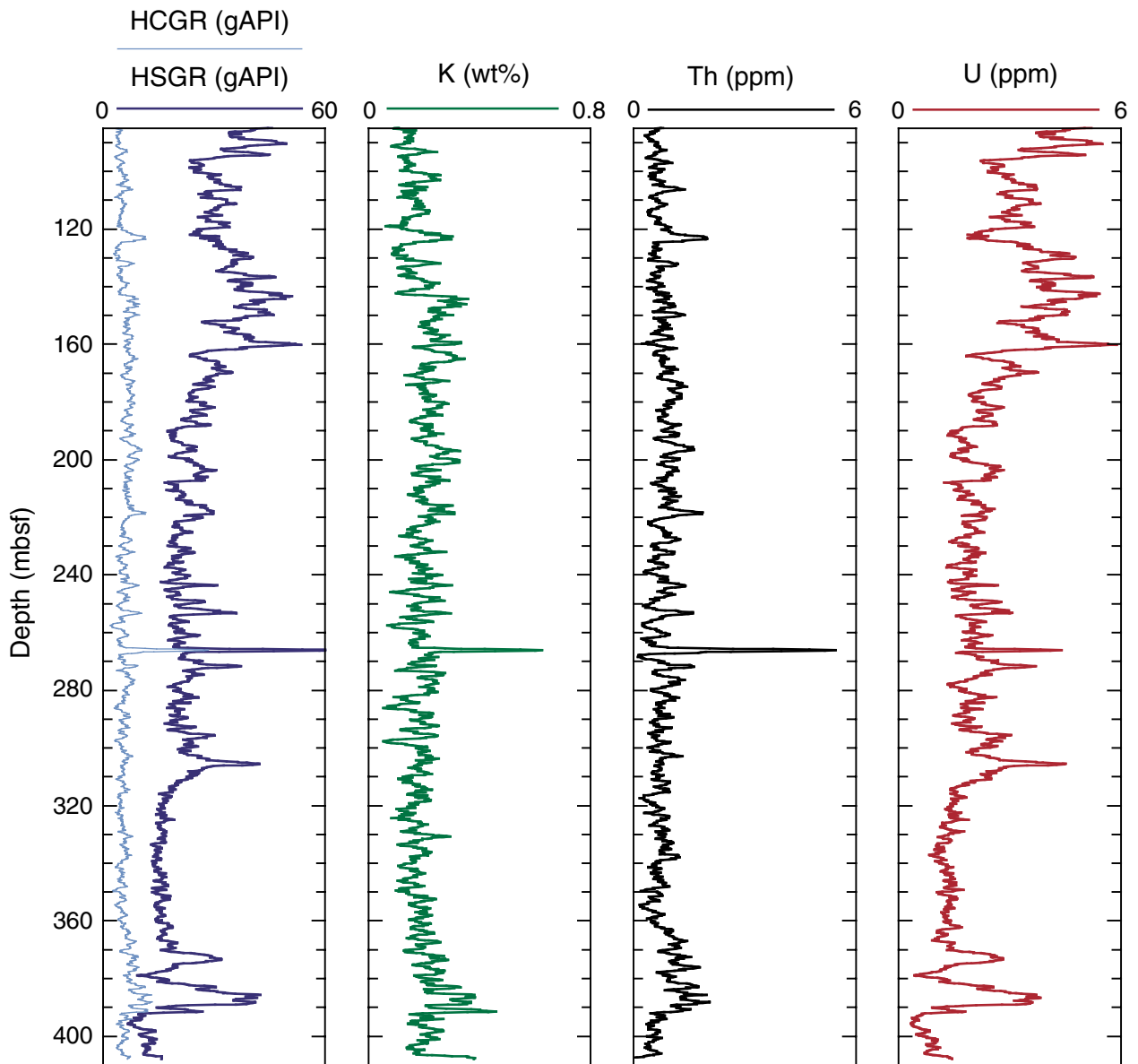


Figure F38. Downhole natural gamma ray activity and core natural gamma ray activity plotted against the Sagan-derived equivalent log depth (eld) for Hole 1238A. A. Total interval cored and logged. B. Interval 110–180 m (eld) C. Interval 180–300 mbsf. Core logging data are in counts per second (cps); downhole logging data are in American Petroleum Institute (gAPI) units. MGT = Multi-Sensor Spectral Gamma Ray Tool.

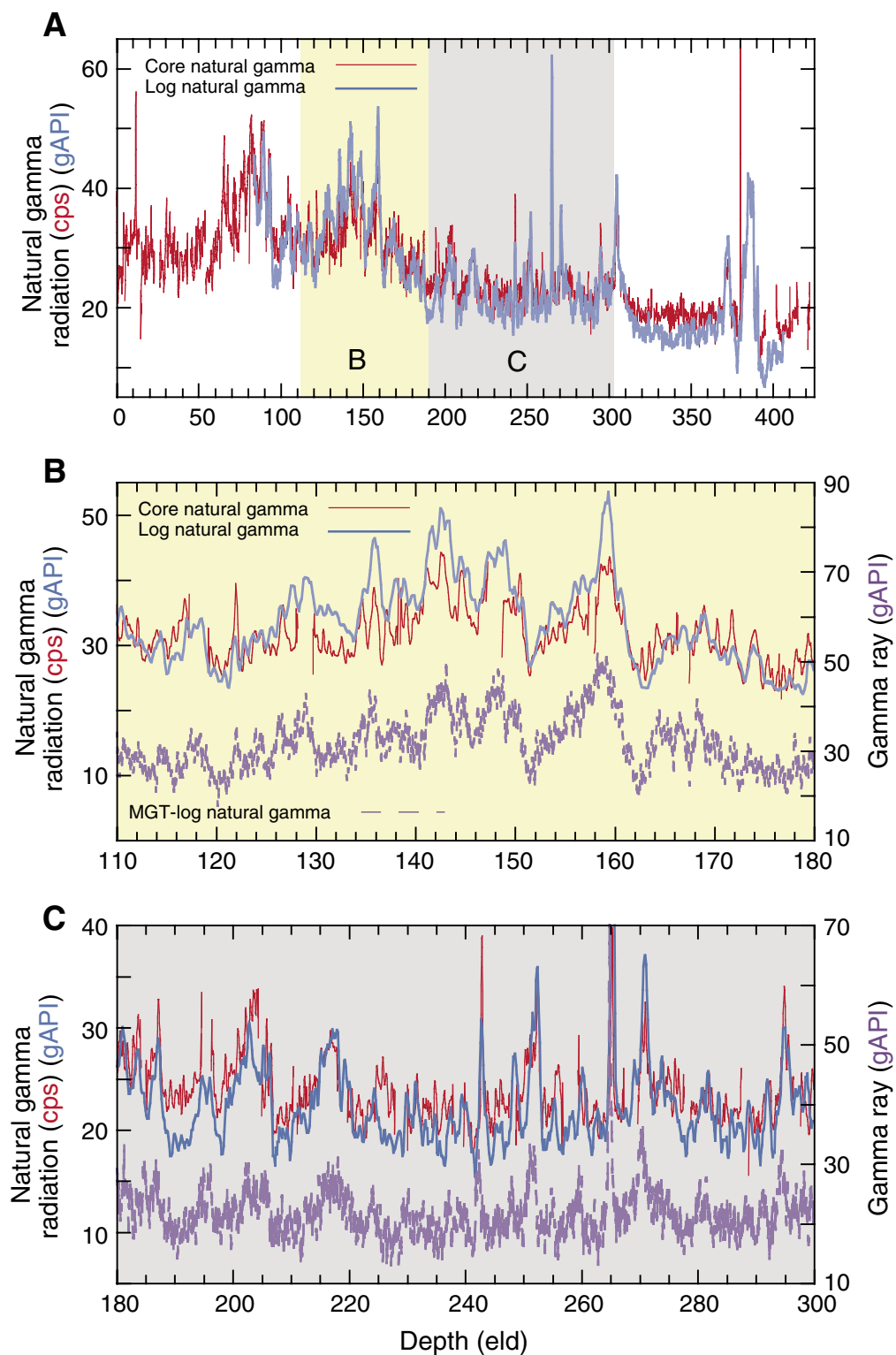


Figure F39. Dynamically normalized FMS image of the borehole illustrating the meter-scale banding characteristic of logging Units 1 and 2. FMS = Formation MicroScanner.

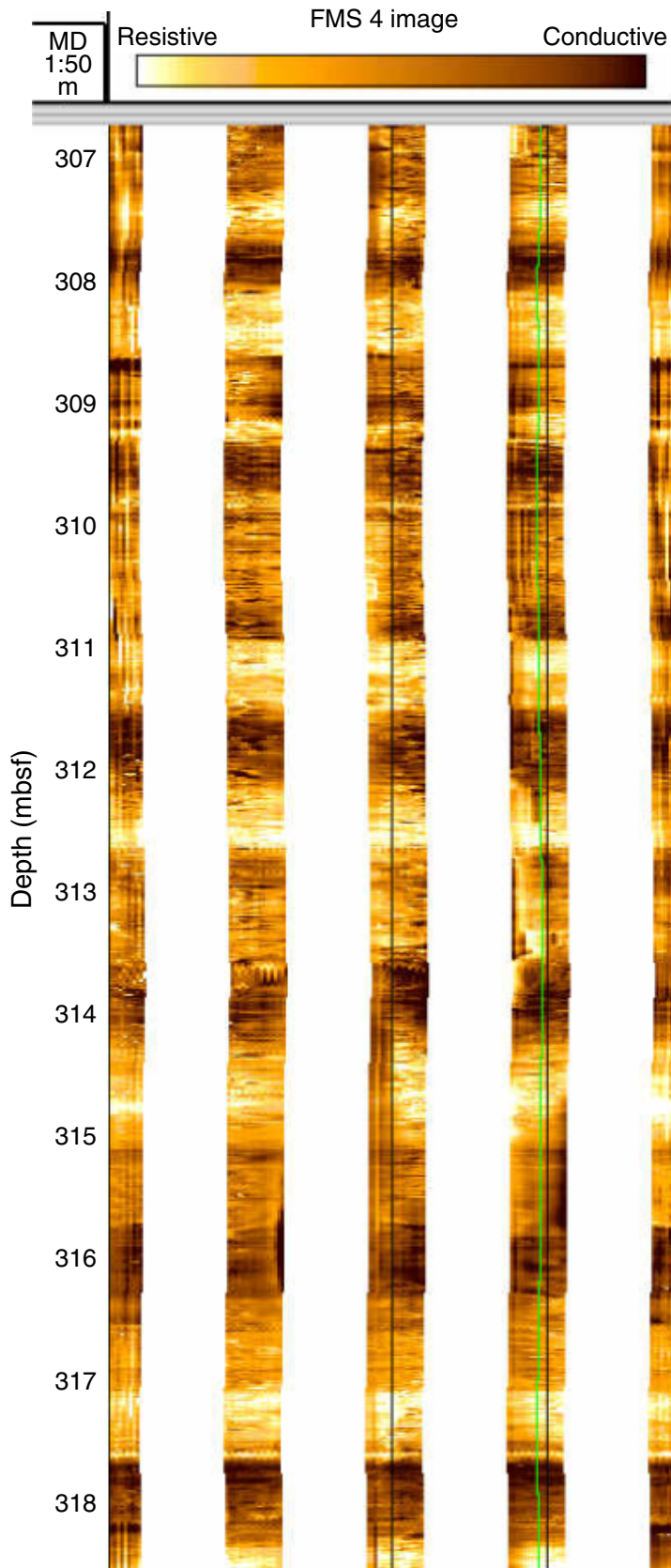


Figure F40. Statically normalized Formation MicroScanner (FMS) image of the borehole showing the resistive (white), well-lithified beds in logging Unit 3, where Core 202-1238A-42X recovered only 34 cm of chalk (see "Lithostratigraphy," p. 6).

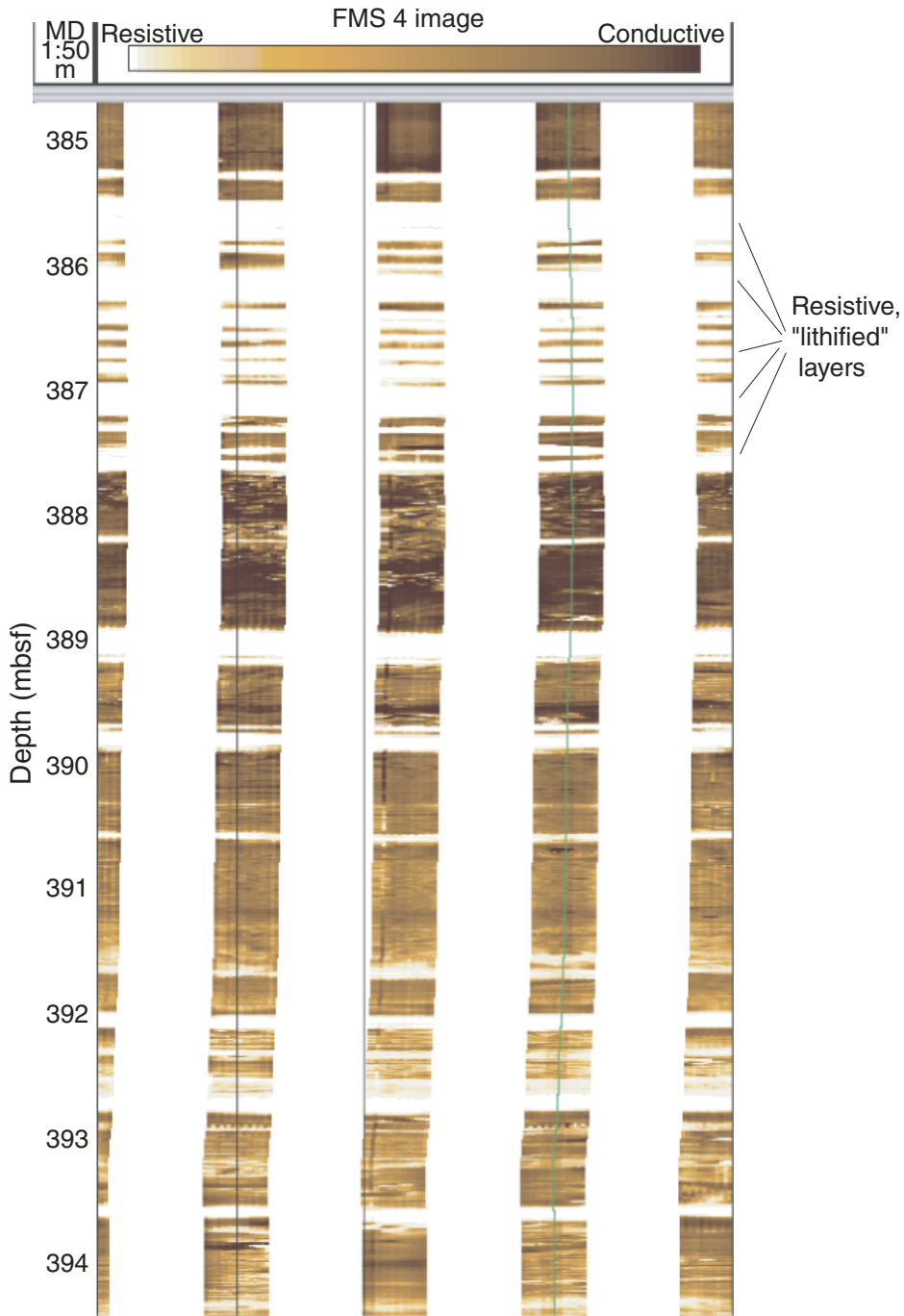


Figure F41. Downhole density plotted with core density against the Sagan-derived equivalent log depth (eld) for Hole 1238A.

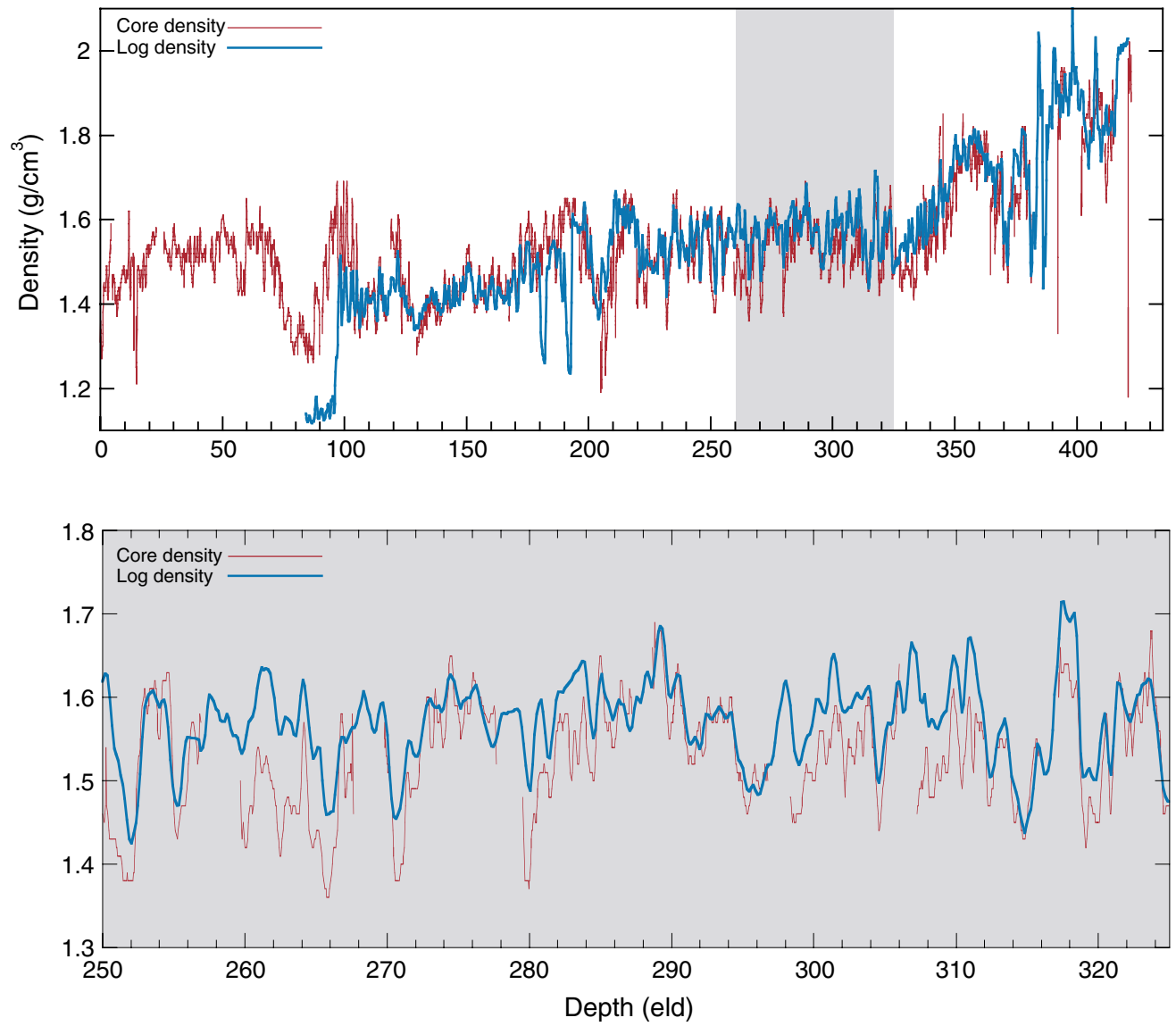


Figure F42. Downhole spectral gamma ray U log plotted with total organic carbon (TOC) values for Hole 1238A.

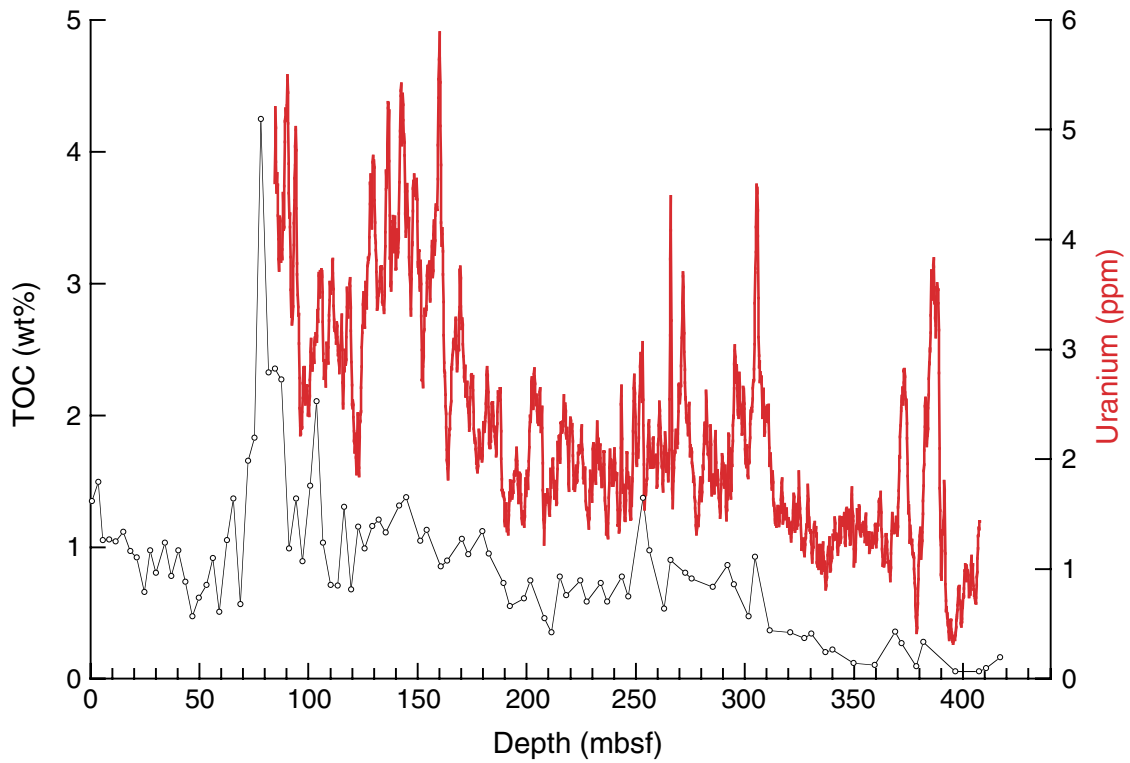


Figure F43. A. Shipboard biostratigraphic and magnetostratigraphic datums and age-depth model. B. Corrected linear sedimentation rates (LSRs), total mass accumulation rates (MARs), and carbonate mass accumulation rates calculated from the smooth age model, average dry density, and calcium carbonate concentrations at 1-m.y. intervals. FO = first occurrence, LO = last occurrence.

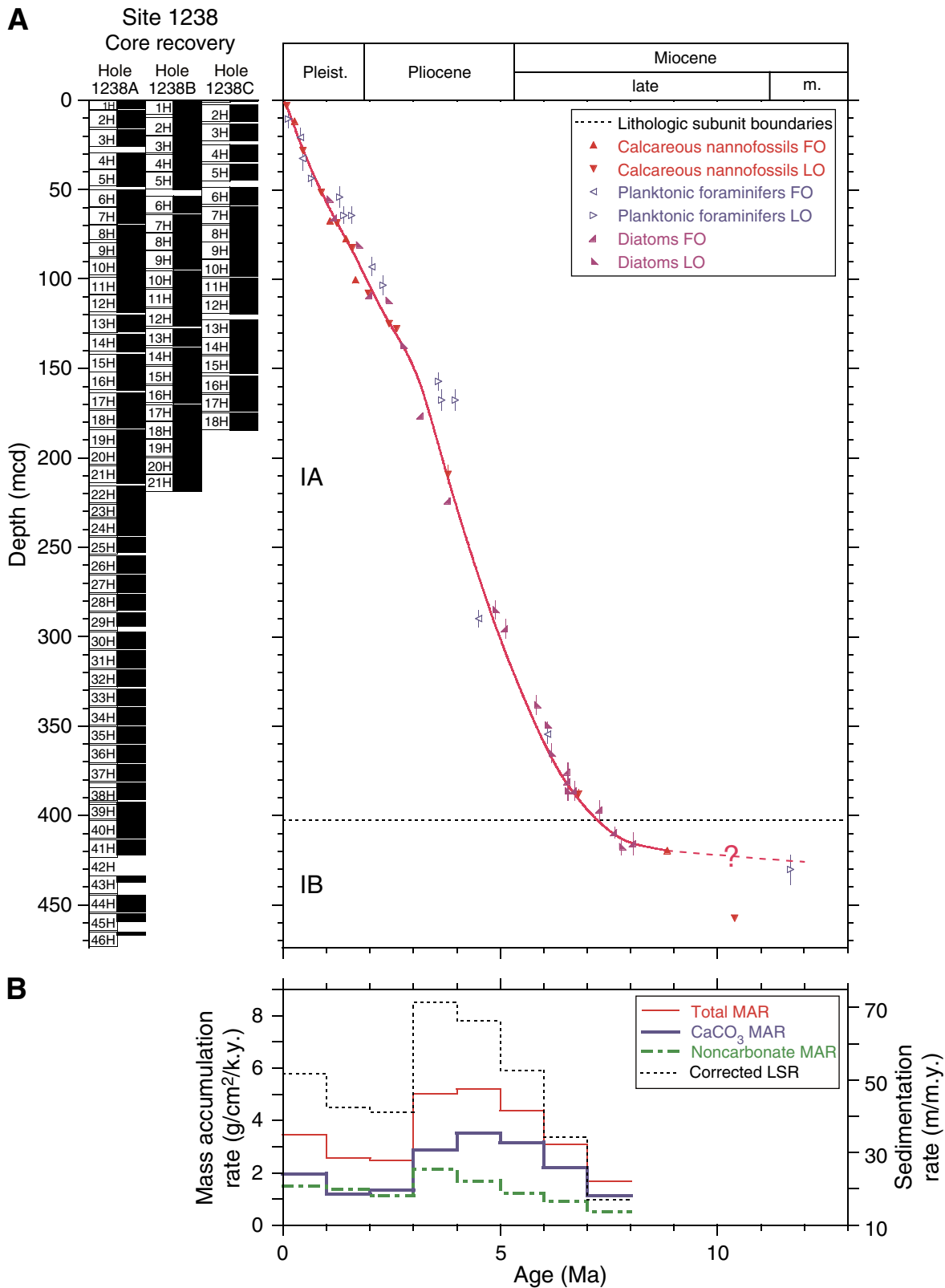


Table T1. Operations summary, Site 1238. (See table notes. Continued on next page.)

Core	Date (May 2002)	Local time (hr)	Depth (mbsf)		Length (m)		Recovery (%)	APCT	Orientation	NMCB
			Top	Bottom	Cored	Recovered				
202-1238A-										
1H	6	0205	0.0	5.0	5.0	5.06	101.2			
2H	6	0300	5.0	14.5	9.5	9.95	104.7			X
3H	6	0350	14.5	24.0	9.5	9.50	100.0		Tensor	
4H	6	0455	24.0	33.5	9.5	9.54	100.4	X	Tensor	X
5H	6	0540	33.5	43.0	9.5	9.96	104.8		Tensor	
6H	6	0640	43.0	52.5	9.5	9.91	104.3	X	Tensor	X
7H	6	0825	52.5	62.0	9.5	9.14	96.2		Tensor	
8H	6	0935	62.0	71.5	9.5	10.03	105.6	X	Tensor	X
9H	6	1020	71.5	81.0	9.5	9.96	104.8		Tensor	
10H	6	1125	81.0	90.5	9.5	10.04	105.7	X	Tensor	X
11H	6	1215	90.5	100.0	9.5	9.80	103.2		Tensor	
12H	6	1255	100.0	109.5	9.5	10.02	105.5		Tensor	X
13H	6	1355	109.5	119.0	9.5	9.09	95.7		Tensor	
14H	6	1505	119.0	128.5	9.5	9.95	104.7		Tensor	
15H	6	1610	128.5	138.0	9.5	9.89	104.1	X	Tensor	
16H	6	1705	138.0	147.5	9.5	9.95	104.7		Tensor	
17H	6	1745	147.5	157.0	9.5	9.96	104.8		Tensor	
18H	6	1845	157.0	166.5	9.5	9.97	105.0		Tensor	
19H	6	1945	166.5	176.0	9.5	10.01	105.4		Tensor	
20H	6	2035	176.0	185.5	9.5	9.97	105.0		Tensor	
21H	6	2120	185.5	195.0	9.5	10.02	105.5		Tensor	
22H	6	2335	195.0	204.5	9.5	9.98	105.1		Tensor*	
23X	7	0050	204.5	211.4	6.9	7.35	106.5			
24X	7	0135	211.4	221.0	9.6	9.42	98.1			
25X	7	0220	221.0	230.3	9.3	8.67	93.2			
26X	7	0305	230.3	240.0	9.7	9.78	100.8			
27X	7	0350	240.0	249.6	9.6	9.74	101.5			
28X	7	0440	249.6	259.2	9.6	9.21	95.9			
29X	7	0520	259.2	268.9	9.7	7.84	80.8			
30X	7	0610	268.9	278.5	9.6	9.79	102.0			
31X	7	0655	278.5	288.2	9.7	9.80	101.0			
32X	7	0735	288.2	297.9	9.7	9.80	101.0			
33X	7	0825	297.9	307.5	9.6	9.83	102.4			
34X	7	0905	307.5	317.1	9.6	9.80	102.1			
35X	7	0945	317.1	326.7	9.6	9.79	102.0			
36X	7	1030	326.7	336.3	9.6	9.77	101.8			
37X	7	1120	336.3	345.9	9.6	9.71	101.2			
38X	7	1210	345.9	355.6	9.7	9.64	99.4			
39X	7	1300	355.6	365.2	9.6	9.81	102.2			
40X	7	1345	365.2	374.9	9.7	9.82	101.2			
41X	7	1440	374.9	384.5	9.6	8.49	88.4			
42X	7	1600	384.5	394.1	9.6	0.34	3.5			
43X	7	1715	394.1	403.7	9.6	3.63	37.8			
44X	7	1759	403.7	413.3	9.6	9.79	102.0			
45X	7	1850	413.3	422.9	9.6	4.47	46.6			
46X	7	2110	422.9	430.6	7.7	1.78	23.1			
			Cored totals:		430.6	409.77	95.2			
202-1238B-										
1H	8	2150	0.0	8.0	8.0	9.85	123.1	X		X
2H	8	2230	8.0	17.5	9.5	9.95	104.7			
3H	8	2310	17.5	27.0	9.5	9.94	104.6		Tensor	X
4H	8	2355	27.0	36.5	9.5	9.86	103.8		Tensor	
5H	9	40	36.5	46.0	9.5	9.99	105.2		Tensor	X
6H	9	120	49.0	58.5	9.5	10.00	105.3		Tensor	
7H	9	210	58.5	68.0	9.5	9.97	105.0		Tensor	X
8H	9	255	68.0	77.5	9.5	10.08	106.1		Tensor	
9H	9	340	77.5	87.0	9.5	9.95	104.7		Tensor	X
10H	9	420	87.0	96.5	9.5	9.98	105.1		Tensor	
11H	9	505	96.5	106.0	9.5	10.10	106.3		Tensor	X
12H	9	550	106.0	115.5	9.5	9.83	103.5		Tensor	
13H	9	640	115.5	125.0	9.5	10.01	105.4		Tensor*	
14H	9	725	125.0	134.5	9.5	9.98	105.1		Tensor*	
15H	9	820	134.5	144.0	9.5	10.08	106.1		Tensor*	
16H	9	900	144.0	153.5	9.5	9.92	104.4		Tensor*	
17H	9	1005	153.5	163.0	9.5	10.03	105.6		Tensor*	
18H	9	1115	163.0	172.5	9.5	9.99	105.2		Tensor*	

Table T1 (continued).

Core	Date (May 2002)	Local time (hr)	Depth (mbsf)		Length (m)		Recovery (%)	APCT	Orientation	NMCB
			Top	Bottom	Cored	Recovered				
19H	9	1210	172.5	182.0	9.5	10.00	105.3		Tensor*	
20H	9	1310	182.0	191.5	9.5	10.02	105.5		Tensor*	
21H	9	1445	191.5	201.0	9.5	9.97	105.0		Tensor*	
Cored totals:					198.0	209.50	105.8			
202-1238C-										
1H	9	1700	0.0	1.0	1.0	1.04	104.0			
2H	9	1740	1.0	10.5	9.5	9.39	98.8			X
3H	9	1815	10.5	20.0	9.5	9.81	103.3			
4H	9	1900	20.0	29.5	9.5	9.87	103.9		Tensor*	X
5H	9	1945	29.5	39.0	9.5	9.15	96.3		Tensor	
6H	9	2025	42.0	51.5	9.5	9.95	104.7		Tensor	X
7H	9	2105	51.5	61.0	9.5	9.98	105.1		Tensor	
8H	9	2145	61.0	70.5	9.5	8.99	94.6		Tensor	X
9H	9	2230	70.5	80.0	9.5	10.04	105.7		Tensor	
10H	9	2305	80.0	89.5	9.5	9.75	102.6		Tensor	X
11H	9	2350	89.5	99.0	9.5	9.99	105.2		Tensor	
12H	10	30	99.0	108.5	9.5	10.05	105.8		Tensor	X
13H	10	125	110.5	120.0	9.5	10.06	105.9		Tensor	
14H	10	230	120.0	129.5	9.5	10.02	105.5		Tensor*	X
15H	10	325	129.5	139.0	9.5	10.02	105.5		Tensor*	
16H	10	410	139.0	148.5	9.5	9.95	104.7		Tensor*	
17H	10	500	148.5	158.0	9.5	9.91	104.3		Tensor*	
18H	10	615	158.0	167.5	9.5	9.88	104.0		Tensor*	
Cored totals:					162.5	167.85	103.3			
Site totals:					791.1	787.12	99.5			

Notes: APCT = advanced piston corer temperature tool (stainless-steel housing is cutting shoe). NMCB = nonmagnetic core barrel, including cutting shoe (made from monel). X = APCT or NMCB was used. Tensor = brand name for core-barrel orientation tool. * = tensor measurement attempted but problem occurred, resulting in bad or no data.

Table T2. Composite depth scale, Site 1238. (See table notes. Continued on next page.)

Core	Depth of core top		Depth offset		Translation to cmcd	
	Drillers (mbsf)	Composite (mcd)	Cumulative (m)	Differential (m)	Growth factor*	Depth (cmcd)†
202-1238A-						
1H	0.0	0.00	0.00	0.00	1.10	0.00
2H	5.0	5.60	0.60	0.60	1.10	5.09
3H	14.5	16.35	1.85	1.25	1.10	14.86
4H	24.0	29.30	5.30	3.45	1.10	26.64
5H	33.5	38.30	4.80	-0.50	1.10	34.82
6H	43.0	49.85	6.85	2.05	1.10	45.32
7H	52.5	59.80	7.30	0.45	1.10	54.36
8H	62.0	70.00	8.00	0.70	1.10	63.64
9H	71.5	77.90	6.40	-1.60	1.10	70.82
10H	81.0	88.15	7.15	0.75	1.10	80.14
11H	90.5	98.90	8.40	1.25	1.10	89.91
12H	100.0	108.85	8.85	0.45	1.10	98.95
13H	109.5	120.25	10.75	1.90	1.10	109.32
14H	119.0	130.95	11.95	1.20	1.10	119.05
15H	128.5	142.25	13.75	1.80	1.10	129.32
16H	138.0	152.10	14.10	0.35	1.10	138.27
17H	147.5	163.35	15.85	1.75	1.10	148.50
18H	157.0	173.50	16.50	0.65	1.10	157.73
19H	166.5	184.40	17.90	1.40	1.10	167.64
20H	176.0	194.15	18.15	0.25	1.10	176.50
21H	185.5	204.45	18.95	0.80	1.10	185.86
22H	195.0	215.75	20.75	1.80	1.10	196.14
23X	204.5	226.20	21.70	0.95	1.10	205.64
24X	211.4	234.05	22.65	0.95	1.10	212.77
25X	221.0	244.60	23.60	0.95	1.10	222.36
26X	230.3	254.85	24.55	0.95	1.10	231.68
27X	240.0	265.50	25.50	0.95	1.10	241.36
28X	249.6	276.05	26.45	0.95	1.10	250.95
29X	259.2	286.60	27.40	0.95	1.10	260.55
30X	268.9	297.25	28.35	0.95	1.10	270.23
31X	278.5	307.80	29.30	0.95	1.10	279.82
32X	288.2	318.45	30.25	0.95	1.10	289.50
33X	297.9	329.10	31.20	0.95	1.10	299.18
34X	307.5	339.65	32.15	0.95	1.10	308.77
35X	317.1	350.20	33.10	0.95	1.10	318.36
36X	326.7	360.75	34.05	0.95	1.10	327.95
37X	336.3	371.30	35.00	0.95	1.10	337.55
38X	345.9	381.85	35.95	0.95	1.10	347.14
39X	355.6	392.50	36.90	0.95	1.10	356.82
40X	365.2	403.05	37.85	0.95	1.10	366.41
41X	374.9	413.70	38.80	0.95	1.10	376.09
42X	384.5	424.25	39.75	0.95	1.10	385.68
43X	394.1	434.80	40.70	0.95	1.10	395.27
44X	403.7	445.35	41.65	0.95	1.10	404.86
45X	413.3	455.90	42.60	0.95	1.10	414.45
46X	422.9	466.45	43.55	0.95	1.10	424.05
202-1238B-						
1H	0.0	0.00	0.00	0.00	1.10	0.00
2H	8.0	9.75	1.75	1.75	1.10	8.86
3H	17.5	20.00	2.50	0.75	1.10	18.18
4H	27.0	30.30	3.30	0.80	1.10	27.55
5H	36.5	40.20	3.70	0.40	1.10	36.55
6H	49.0	53.45	4.45	0.75	1.10	48.59
7H	58.5	64.30	5.80	1.35	1.10	58.45
8H	68.0	74.10	6.10	0.30	1.10	67.36
9H	77.5	84.25	6.75	0.65	1.10	76.59
10H	87.0	95.25	8.25	1.50	1.10	86.59
11H	96.5	105.95	9.45	1.20	1.10	96.32
12H	106.0	116.65	10.65	1.20	1.10	106.05
13H	115.5	127.70	12.20	1.55	1.10	116.09
14H	125.0	138.45	13.45	1.25	1.10	125.86
15H	134.5	149.00	14.50	1.05	1.10	135.45
16H	144.0	159.60	15.60	1.10	1.10	145.09
17H	153.5	170.05	16.55	0.95	1.10	154.59
18H	163.0	179.60	16.60	0.05	1.10	163.27

Table T2 (continued).

Core	Depth of core top		Depth offset		Translation to cmcd	
	Drillers (mbsf)	Composite (mcd)	Cumulative (m)	Differential (m)	Growth factor*	Depth (cmcd)†
19H	172.5	189.55	17.05	0.45	1.10	172.32
20H	182.0	199.85	17.85	0.80	1.10	181.68
21H	191.5	209.10	17.60	-0.25	1.10	190.09
202-1238C-						
1H	0.0	0.00	0.00	0.00	1.10	0.00
2H	1.0	2.45	1.45	1.45	1.10	2.23
3H	10.5	13.05	2.55	1.10	1.10	11.86
4H	20.0	24.75	4.75	2.20	1.10	22.50
5H	29.5	35.60	6.10	1.35	1.10	32.36
6H	42.0	48.55	6.55	0.45	1.10	44.14
7H	51.5	59.35	7.85	1.30	1.10	53.95
8H	61.0	69.65	8.65	0.80	1.10	63.32
9H	70.5	79.00	8.50	-0.15	1.10	71.82
10H	80.0	89.00	9.00	0.50	1.10	80.91
11H	89.5	99.50	10.00	1.00	1.10	90.45
12H	99.0	109.75	10.75	0.75	1.10	99.77
13H	110.5	122.90	12.40	1.65	1.10	111.73
14H	120.0	132.60	12.60	0.20	1.10	120.55
15H	129.5	143.10	13.60	1.00	1.10	130.09
16H	139.0	153.95	14.95	1.35	1.10	139.95
17H	148.5	164.30	15.80	0.85	1.10	149.36
18H	158.0	174.90	16.90	1.10	1.10	159.00

Notes: * = calculated based on mbsf-mcd relationship for splice shown in Figure F11, p. 42. † = within the splice, the following equations apply: cmcd = mcd/growth factor; mcd = mbsf + cumulative depth offset, mcd = cmcd × growth factor, mbsf = cmcd × growth factor – cumulative offset. The growth factor in XCB cores is extrapolated from the APC section. This table is also available in ASCII.

Table T3. Splice tie points, Site 1238.

Hole, core, section, interval (cm)	Depth			Tie to	Hole, core, section, interval (cm)	Depth		
	(mbsf)	(mcd)	(cmcd)			(mbsf)	(mcd)	(cmcd)
202-					202-			
1238B-1H-5, 140.0	7.40	7.40	6.73	Tie to	1238A-2H-2, 30.0	6.80	7.40	6.73
1238A-2H-5, 105.0	12.05	12.65	11.5	Tie to	1238B-2H-2, 140.0	10.90	12.65	11.5
1238B-2H-6, 80.0	16.30	18.05	16.41	Tie to	1238A-3H-2, 20.0	16.20	18.05	16.41
1238A-3H-5, 60.0	21.10	22.95	20.86	Tie to	1238B-3H-2, 145.0	20.45	22.95	20.86
1238B-3H-6, 115.0	26.15	28.65	26.05	Tie to	1238C-4H-3, 90.0	23.90	28.65	26.05
1238C-4H-6, 10.0	27.60	32.35	29.41	Tie to	1238B-4H-2, 55.0	29.05	32.35	29.41
1238B-4H-5, 125.0	34.25	37.55	34.14	Tie to	1238C-5H-2, 45.0	31.45	37.55	34.14
1238C-5H-5, 105.0	36.55	42.65	38.77	Tie to	1238B-5H-2, 95.0	38.95	42.65	38.77
1238B-5H-7, 15.0	45.65	49.35	44.86	Tie to	1238C-6H-1, 80.0	42.80	49.35	44.86
1238C-6H-5, 120.0	49.20	55.75	50.68	Tie to	1238B-6H-2, 80.0	51.30	55.75	50.68
1238B-6H-6, 35.0	56.85	61.30	55.73	Tie to	1238C-7H-2, 45.0	53.45	61.3	55.73
1238C-7H-6, 140.0	60.40	68.25	62.05	Tie to	1238B-7H-3, 95.0	62.45	68.25	62.05
1238B-7H-5, 40.0	64.90	70.70	64.27	Tie to	1238C-8H-1, 105.0	62.05	70.7	64.27
1238C-8H-6, 50.0	69.00	77.65	70.59	Tie to	1238B-8H-3, 55.0	71.55	77.65	70.59
1238B-8H-6, 110.0	76.60	82.70	75.18	Tie to	1238C-9H-3, 70.0	74.20	82.7	75.18
1238C-9H-5, 20.0	76.70	85.20	77.45	Tie to	1238B-9H-1, 95.0	78.45	85.2	77.45
1238B-9H-4, 120.0	83.20	89.95	81.77	Tie to	1238C-10H-1, 95.0	80.95	89.95	81.77
1238C-10H-5, 130.0	87.30	96.30	87.55	Tie to	1238B-10H-1, 105.0	88.05	96.3	87.55
1238B-10H-5, 25.0	93.25	101.50	92.27	Tie to	1238C-11H-2, 50.0	91.50	101.5	92.27
1238C-11H-5, 130.0	96.80	106.80	97.09	Tie to	1238B-11H-1, 85.0	97.35	106.8	97.09
1238B-11H-5, 130.0	103.80	113.25	102.95	Tie to	1238C-12H-3, 50.0	102.50	113.25	102.95
1238C-12H-6, 20.0	106.70	117.45	106.77	Tie to	1238B-12H-1, 80.0	106.80	117.45	106.77
1238B-12H-6, 140.0	114.90	125.55	114.14	Tie to	1238C-13H-2, 115.0	113.15	125.55	114.14
1238C-13H-5, 50.0	117.00	129.40	117.64	Tie to	1238B-13H-2, 20.0	117.20	129.4	117.64
1238B-13H-5, 20.0	121.70	133.90	121.73	Tie to	1238C-14H-1, 130.0	121.30	133.9	121.73
1238C-14H-5, 120.0	127.20	139.80	127.09	Tie to	1238B-14H-1, 135.0	126.35	139.8	127.09
1238B-14H-5, 55.0	131.55	145.00	131.82	Tie to	1238C-15H-2, 40.0	131.40	145	131.82
1238C-15H-5, 75.0	136.25	149.85	136.23	Tie to	1238B-15H-1, 85.0	135.35	149.85	136.23
1238B-15H-6, 40.0	142.40	156.90	142.64	Tie to	1238C-16H-2, 145.0	141.95	156.9	142.64
1238C-16H-6, 80.0	147.30	162.25	147.5	Tie to	1238B-16H-2, 115.0	146.65	162.25	147.5
1238B-16H-5, 50.0	150.50	166.10	151	Tie to	1238C-17H-2, 30.0	150.30	166.1	151
1238C-17H-6, 5.0	156.05	171.85	156.23	Tie to	1238B-17H-2, 30.0	155.30	171.85	156.23
1238B-17H-6, 120.0	162.20	178.75	162.5	Tie to	1238C-18H-3, 85.0	161.85	178.75	162.5
1238C-18H-6, 95.0	166.45	183.35	166.68	Tie to	1238B-18H-3, 75.0	166.75	183.35	166.68
1238B-18H-6, 100.0	171.50	188.10	171	Tie to	1238A-19H-3, 70.0	170.20	188.1	171
1238A-19H-6, 60.0	174.60	192.50	175	Tie to	1238B-19H-2, 145.0	175.45	192.5	175
1238B-19H-6, 25.0	180.25	197.30	179.36	Tie to	1238A-20H-3, 15.0	179.15	197.3	179.36
1238A-20H-6, 105.0	184.55	202.70	184.27	Tie to	1238B-20H-2, 135.0	184.85	202.7	184.27
1238B-20H-6, 85.0	190.35	208.20	189.27	Tie to	1238A-21H-3, 75.0	189.25	208.2	189.27
1238A-21H-6, 20.0	193.20	212.15	192.86	Tie to	1238B-21H-3, 5.0	194.55	212.15	192.86
1238B-21H-6, 135.0	200.35	217.95	198.14	Tie to	1238A-22H-2, 70.0	197.20	217.95	198.14
1238A-22H-7, 65.0	204.65	225.40	204.91					

Note: This table is also available in [ASCII](#).

Table T4. OSUS-MS measurements, Hole 1238A.

Core, section, interval (cm)	Depth		Magnetic susceptibility (instrument units)	Run number	Depth from top of core (cm)
	(mbsf)	(mcd)			
202-1238A-					
1H-1, 5	0.05	0.05	8.2	1146	5
1H-1, 10	0.10	0.10	10.1	1146	10
1H-1, 15	0.15	0.15	11.4	1146	15
1H-1, 20	0.20	0.20	11.9	1146	20
1H-1, 25	0.25	0.25	12.0	1146	25
1H-1, 30	0.30	0.30	12.6	1146	30
1H-1, 35	0.35	0.35	12.3	1146	35
1H-1, 40	0.40	0.40	10.9	1146	40
1H-1, 45	0.45	0.45	9.0	1146	45
1H-1, 50	0.50	0.50	7.9	1146	50
1H-1, 55	0.55	0.55	5.6	1146	55
1H-1, 60	0.60	0.60	5.4	1146	60
1H-1, 65	0.65	0.65	5.2	1146	65
1H-1, 70	0.70	0.70	4.1	1146	70
1H-1, 75	0.75	0.75	3.4	1146	75
1H-1, 80	0.80	0.80	2.9	1146	80
1H-1, 85	0.85	0.85	2.6	1146	85
1H-1, 90	0.90	0.90	2.4	1146	90
1H-1, 95	0.95	0.95	2.0	1146	95
1H-1, 100	1.00	1.00	1.9	1146	100
1H-1, 105	1.05	1.05	1.4	1146	105
1H-1, 110	1.10	1.10	1.3	1146	110
1H-1, 115	1.15	1.15	1.1	1146	115
1H-1, 120	1.20	1.20	1.0	1146	120
1H-1, 125	1.25	1.25	1.0	1146	125
1H-1, 130	1.30	1.30	1.2	1146	130
1H-1, 135	1.35	1.35	1.4	1146	135
1H-1, 140	1.40	1.40	1.4	1146	140
1H-1, 145	1.45	1.45	1.3	1146	145
1H-2, 5	1.55	1.55	2.2	1147	155
1H-2, 10	1.60	1.60	2.2	1147	160
1H-2, 15	1.65	1.65	2.4	1147	165
1H-2, 20	1.70	1.70	2.8	1147	170
1H-2, 25	1.75	1.75	2.4	1147	175
1H-2, 30	1.80	1.80	2.1	1147	180
1H-2, 35	1.85	1.85	1.9	1147	185
1H-2, 40	1.90	1.90	2.0	1147	190
1H-2, 45	1.95	1.95	2.0	1147	195
1H-2, 50	2.00	2.00	2.0	1147	200
1H-2, 55	2.05	2.05	2.0	1147	205
1H-2, 60	2.10	2.10	2.1	1147	210
1H-2, 65	2.15	2.15	2.1	1147	215
1H-2, 70	2.20	2.20	2.3	1147	220
1H-2, 75	2.25	2.25	2.4	1147	225
1H-2, 80	2.30	2.30	2.4	1147	230
1H-2, 85	2.35	2.35	2.4	1147	235
1H-2, 90	2.40	2.40	2.7	1147	240
1H-2, 95	2.45	2.45	2.6	1147	245
1H-2, 100	2.50	2.50	2.6	1147	250
1H-2, 105	2.55	2.55	2.6	1147	255
1H-2, 110	2.60	2.60	2.7	1147	260
1H-2, 115	2.65	2.65	2.8	1147	265
1H-2, 120	2.70	2.70	2.9	1147	270
1H-2, 125	2.75	2.75	3.4	1147	275
1H-2, 130	2.80	2.80	3.9	1147	280
1H-2, 135	2.85	2.85	4.0	1147	285
1H-2, 140	2.90	2.90	3.6	1147	290
1H-3, 5	3.05	3.05	4.4	1148	300
1H-3, 10	3.10	3.10	4.5	1148	305
1H-3, 15	3.15	3.15	3.7	1148	310
1H-3, 20	3.20	3.20	3.1	1148	315
1H-3, 25	3.25	3.25	2.6	1148	320
1H-3, 30	3.30	3.30	2.5	1148	325

Note: Only a portion of this table appears here. The complete table is available in [ASCII](#).

Table T5. OSUS-MS measurements, Hole 1238B.

Core, section, interval (cm)	Depth		Magnetic susceptibility (instrument units)	Run number	Depth from top of core (cm)
	(mbsf)	(mcd)			
202-1238B-					
1H-1, 5	0.05	0.05	8.1	1318	5
1H-1, 10	0.10	0.10	10.9	1318	10
1H-1, 15	0.15	0.15	12.6	1318	15
1H-1, 20	0.20	0.20	12.3	1318	20
1H-1, 25	0.25	0.25	12.5	1318	25
1H-1, 30	0.30	0.30	11.9	1318	30
1H-1, 35	0.35	0.35	11.5	1318	35
1H-1, 40	0.40	0.40	10.4	1318	40
1H-1, 45	0.45	0.45	8.8	1318	45
1H-1, 50	0.50	0.50	7.2	1318	50
1H-1, 55	0.55	0.55	5.3	1318	55
1H-1, 60	0.60	0.60	4.3	1318	60
1H-1, 65	0.65	0.65	3.5	1318	65
1H-1, 70	0.70	0.70	3.3	1318	70
1H-1, 75	0.75	0.75	3.0	1318	75
1H-1, 80	0.80	0.80	2.7	1318	80
1H-1, 85	0.85	0.85	2.3	1318	85
1H-1, 90	0.90	0.90	2.0	1318	90
1H-1, 95	0.95	0.95	1.8	1318	95
1H-1, 100	1.00	1.00	1.5	1318	100
1H-1, 105	1.05	1.05	1.4	1318	105
1H-1, 110	1.10	1.10	1.1	1318	110
1H-1, 115	1.15	1.15	0.8	1318	115
1H-1, 120	1.20	1.20	0.8	1318	120
1H-1, 125	1.25	1.25	0.7	1318	125
1H-1, 130	1.30	1.30	0.7	1318	130
1H-1, 135	1.35	1.35	0.8	1318	135
1H-1, 140	1.40	1.40	1.0	1318	140
1H-1, 145	1.45	1.45	1.0	1318	145
1H-2, 5	1.55	1.55	2.0	1319	154
1H-2, 10	1.60	1.60	2.1	1319	159
1H-2, 15	1.65	1.65	2.2	1319	164
1H-2, 20	1.70	1.70	2.1	1319	169
1H-2, 25	1.75	1.75	2.1	1319	174
1H-2, 30	1.80	1.80	2.1	1319	179
1H-2, 35	1.85	1.85	2.0	1319	184
1H-2, 40	1.90	1.90	1.9	1319	189
1H-2, 45	1.95	1.95	1.7	1319	194
1H-2, 50	2.00	2.00	1.8	1319	199
1H-2, 55	2.05	2.05	1.8	1319	204
1H-2, 60	2.10	2.10	1.8	1319	209
1H-2, 65	2.15	2.15	1.7	1319	214
1H-2, 70	2.20	2.20	1.7	1319	219
1H-2, 75	2.25	2.25	1.8	1319	224
1H-2, 80	2.30	2.30	1.9	1319	229
1H-2, 85	2.35	2.35	2.0	1319	234
1H-2, 90	2.40	2.40	2.1	1319	239
1H-2, 95	2.45	2.45	2.0	1319	244
1H-2, 100	2.50	2.50	2.1	1319	249
1H-2, 105	2.55	2.55	2.1	1319	254
1H-2, 110	2.60	2.60	2.1	1319	259
1H-2, 115	2.65	2.65	2.0	1319	264
1H-2, 120	2.70	2.70	2.3	1319	269
1H-2, 125	2.75	2.75	2.3	1319	274
1H-2, 130	2.80	2.80	2.3	1319	279
1H-2, 135	2.85	2.85	2.6	1319	284
1H-2, 140	2.90	2.90	3.0	1319	289
1H-2, 145	2.95	2.95	3.0	1319	294
1H-3, 5	3.06	3.06	3.8	1320	304
1H-3, 10	3.11	3.11	4.1	1320	309
1H-3, 15	3.16	3.16	4.0	1320	314
1H-3, 20	3.21	3.21	4.2	1320	319
1H-3, 25	3.26	3.26	4.3	1320	324

Note: Only a portion of this table appears here. The complete table is available in [ASCII](#).

Table T6. OSUS-MS measurements, Hole 1238C.

Core, section, interval (cm)	Depth		Magnetic susceptibility (instrument units)	Run number	Depth from top of core (cm)
	(mbsf)	(mcd)			
202-1238C-					
1H-1, 5	1.35	0.40	52.4	1766	5
1H-1, 10	1.40	0.45	16.9	1766	10
1H-1, 15	1.45	0.50	6.3	1766	15
1H-1, 20	1.50	0.55	4.7	1766	20
1H-1, 25	1.55	0.60	4.6	1766	25
1H-1, 30	1.60	0.65	4.0	1766	30
1H-1, 35	1.65	0.70	3.6	1766	35
1H-1, 40	1.70	0.75	3.5	1766	40
1H-1, 45	1.75	0.80	3.2	1766	45
1H-1, 50	1.80	0.85	3.1	1766	50
1H-1, 55	1.85	0.90	3.3	1766	55
1H-1, 60	1.90	0.95	3.2	1766	60
1H-1, 65	1.95	1.00	3.5	1766	65
1H-1, 70	2.00	1.05	3.6	1766	70
1H-1, 75	2.05	1.10	3.7	1766	75
1H-1, 80	2.10	1.15	4.0	1766	80
1H-1, 85	2.15	1.20	4.4	1766	85
1H-1, 90	2.20	1.25	4.4	1766	90
1H-1, 95	2.25	1.30	4.8	1766	95
1H-1, 100	2.30	1.35	5.1	1766	100
1H-1, 105	2.35	1.40	5.3	1766	105
1H-1, 110	2.40	1.45	5.6	1766	110
1H-1, 115	2.45	1.50	5.7	1766	115
1H-1, 120	2.50	1.55	6.2	1766	120
1H-1, 125	2.55	1.60	7.8	1766	125
1H-1, 130	2.60	1.65	5.2	1766	130
1H-1, 135	2.65	1.70	5.0	1766	135
1H-1, 140	2.70	1.75	5.1	1766	140
1H-1, 145	2.75	1.80	4.5	1766	145
1H-2, 5	2.86	1.91	5.8	1767	155
1H-2, 10	2.91	1.96	6.5	1767	160
1H-2, 15	2.96	2.01	6.8	1767	165
1H-2, 20	3.01	2.06	7.0	1767	170
1H-2, 25	3.06	2.11	7.2	1767	175
1H-2, 30	3.11	2.16	7.5	1767	180
1H-2, 35	3.16	2.21	8.9	1767	185
1H-2, 40	3.21	2.26	9.6	1767	190
1H-2, 45	3.26	2.31	9.9	1767	195
1H-2, 50	3.31	2.36	9.8	1767	200
1H-2, 55	3.36	2.41	9.5	1767	205
1H-2, 60	3.41	2.46	9.9	1767	210
1H-2, 65	3.46	2.51	13.4	1767	215
1H-2, 70	3.51	2.56	19.8	1767	220
1H-2, 75	3.56	2.61	22.9	1767	225
1H-2, 80	3.61	2.66	23.5	1767	230
1H-2, 85	3.66	2.71	27.5	1767	235
1H-2, 90	3.71	2.76	31.2	1767	240
1H-2, 95	3.76	2.81	29.8	1767	245
1H-2, 100	3.81	2.86	24.4	1767	250
1H-2, 105	3.86	2.91	17.2	1767	255
1H-2, 110	3.91	2.96	11.8	1767	260
1H-2, 115	3.96	3.01	9.6	1767	265
1H-2, 120	4.01	3.06	8.8	1767	270
1H-2, 125	4.06	3.11	9.1	1767	275
1H-2, 130	4.11	3.16	8.4	1767	280
1H-2, 135	4.16	3.21	8.0	1767	285
1H-2, 140	4.21	3.26	9.5	1767	290
1H-2, 145	4.26	3.31	9.6	1767	295
1H-3, 5	4.37	3.42	9.3	1788	305
1H-3, 10	4.42	3.47	8.8	1788	310
1H-3, 15	4.47	3.52	8.1	1788	315
1H-3, 20	4.52	3.57	7.3	1788	320
1H-3, 25	4.57	3.62	6.6	1788	325

Note: Only a portion of this table appears here. The complete table is available in [ASCII](#).

Table T7. Lithologic Unit I, Site 1238.

Unit/ Subunit	Top			Base			Description	Interpretation
	Hole, core, section, interval (cm)	Depth (mbsf) (mcd)		Hole, core, section, interval (cm)	Depth (mbsf) (mcd)			
	202-			202-				
IA	1238A-1H-1, 0	0.0	0.0	1238A-39X-CC, 34	365.5	402.4	Interbedded nannofossil ooze, diatom nannofossil ooze, and nannofossil diatom ooze with minor contributions from clay and foraminifers, 17 ash layers, meter-scale light/dark banding	Pelagic setting with moderate to high productivity, alternating between carbonate and siliceous oozes, possibly on orbital timescales
	1238B-1H-1, 0	0.0	0.0	1238B-21H-CC, 30	201.5	219.1		
	1238C-1H-1, 0	0.0	0.0	1238C-18H-CC, 21	168.0	184.9		
IB	1238A-40X-1, 0	365.2	403.1	1238A-46X-CC, 36	424.7	467.3	Diatom ooze, partially lithified nannofossil ooze with micrite, chalk, and chert	Lithification and diagenesis

Table T8. Ash layers, Site 1238.

Number	Core, section, interval (cm)	Top (mcd)	Bottom depth		Core, section, interval (cm)	Top (mcd)	Bottom depth		Core, section, interval (cm)	Top (mcd)	Bottom depth	
			(mcd)	(mbsf)			(mcd)	(mbsf)			(mcd)	(mbsf)
1	202-1238A-2H-5/6, (5)138-(6)7	13.02	13.21	12.61	202-1238B-2H-3, 25-40	13.00	13.15	11.40	202-1238C-3H-1, 0-20	13.05	13.25	10.70
2	Core gap				3H-6, 8-10	27.62	27.64	25.14	NF			
3	Core gap				3H-6, 70-73	28.24	28.27	25.77	4H-3, 45-50	28.20	28.25	23.50
4	Core gap				3H-6, 95-98	28.49	28.52	26.02	4H-3, 70-71	28.45	28.46	23.71
5	4H-4, 97- 100	34.02	34.05	28.75	4H-3, 95-100	34.25	34.30	31.00	4H-7, 48-51	34.23	34.26	29.51
6	NF				6H-5, 79-80	60.28	60.29	55.84	Core gap			
7	NF				6H-5, 94-96	60.43	60.45	56.00	7H-1, 107-110	60.42	60.45	52.60
8	Core gap				7H-4, 137-142	70.21	70.26	64.46	Core gap			
9	8H-2, 11- 15	71.62	71.66	63.66	7H-5, 62-65	70.97	71.00	65.20	8H-2, 41-46	71.56	71.61	62.96
10	9H-2, 83- 84	80.24	80.25	73.85	NF				9H-1, 117-121	80.17	80.21	71.71
11	11H-1, 71- 73	99.61	99.63	91.23	10H-3, 136-140	99.63	99.67	91.42	11H-1, 2-16	99.52	99.66	89.66
12	11H-2, 82- 82	101.22	101.22	92.82	NF				NF			
13	NF								11H-5, 22-23	105.72	105.73	95.73
14	14H-2, 144-150	133.90	133.96	122.01	13H-5, 24-29	133.98	134.03	121.83	14H-1, 134-137	133.94	133.97	137.00
15	27X-3, 45- 80	268.96	269.31	243.81								
16	28X-3, 122- 124	280.29	280.31	253.86								
17	29X-4, 43- 46	291.55	291.58	264.18								

Notes: Ash layers that could be correlated between holes are located in the same row and printed in bold type. There are a total of 17 ash layers at Site 1238, 10 of which are correlative between holes. NF = not found.

Table T9. Age-depth control points, Hole 1238A. (See table notes. Continued on next page.)

Datum	Source	Age (Ma)		Top sample (FO presence/LO absence)		Bottom sample (LO presence/FO absence)		Age (Ma)		Depth		
		Minimum	Maximum	Core, section, interval (cm)	Depth (mbsf)	Core, section, interval (cm)	Depth (mbsf)	Average	Uncertainty (±)	Average (mbsf)	Average (mcd)	Uncertainty (±m)
		202-1238A-										
Start of <i>Emiliana huxleyi</i> acme	CN	0.08	0.08	1H-2, 75	2.25	1H-3, 75	3.75	0.08	0.00	3.00	3.00	0.75
LO <i>Globigerinoides ruber</i> pink	PF	0.12	0.12	1H-CC, 9	5.01	2H-CC, 23	14.96	0.12	0.00	9.99	10.29	4.98
FO <i>Emiliana huxleyi</i>	CN	0.26	0.26	2H-4, 75	10.28	2H-5, 75	11.79	0.26	0.00	11.04	11.64	0.76
FO <i>Globigerinoides ruber</i> pink	PF	0.40	0.40	2H-CC, 23	14.96	3H-CC, 14	24.01	0.40	0.00	19.49	20.71	4.53
FO <i>Globorotalia hirsuta</i>	PF	0.45	0.45	3H-CC, 14	24.01	4H-CC, 17	33.54	0.45	0.00	28.78	32.35	4.77
LO <i>Pseudoemiliana lacunosa</i>	CN	0.46	0.46	3H-CC, 14	24.01	4H-1, 75	24.75	0.46	0.00	24.38	27.96	0.37
LO <i>Globorotalia tosaensis</i>	PF	0.65	0.65	4H-CC, 17	33.54	5H-CC, 19	43.44	0.65	0.00	38.49	43.54	4.95
LO <i>Reticulofenestra asanoi</i>	CN	0.88	0.88	6H-1, 75	43.75	6H-2, 75	45.26	0.88	0.00	44.51	51.36	0.76
LO <i>Rhizosolenia matuyamai</i>	D	1.05	1.05	6H-4, 75	48.28	6H-4, 100	48.53	1.05	0.00	48.41	55.26	0.13
FO <i>Reticulofenestra asanoi</i>	CN	1.08	1.08	7H-5, 75	59.28	7H-6, 75	60.79	1.08	0.00	60.04	67.34	0.75
FO <i>Rhizosolenia matuyamai</i>	D	1.18	1.18	7H-4, 75	57.77	7H-5, 75	59.28	1.18	0.00	58.53	65.83	0.75
LO <i>Gephyrocapsa</i> (large)	CN	1.24	1.24	7H-6, 75	60.79	7H-CC, 1	61.66	1.24	0.00	61.23	68.53	0.44
LO <i>Globigerinoides obliquus</i>	PF	1.30	1.30	5H-CC, 19	43.44	6H-CC, 32	52.93	1.30	0.00	48.19	54.01	4.75
LO <i>Pulleniatina finalis</i>	PF	1.40	1.40	6H-CC, 32	52.93	7H-CC, 0	61.65	1.40	0.00	57.29	64.37	4.36
FO <i>Gephyrocapsa</i> (large)	CN	1.45	1.45	8H-5, 75	68.79	8H-6, 75	70.30	1.45	0.00	69.55	77.55	0.75
LO <i>Neogloboquadrina acostaensis</i>	PF	1.58	1.58	6H-CC, 32	52.93	7H-CC, 0	61.65	1.58	0.00	57.29	64.37	4.36
LO <i>Calcidiscus macintyre</i>	CN	1.59	1.59	9H-3, 75	75.27	9H-4, 75	76.79	1.59	0.00	76.03	82.43	0.76
FO <i>Gephyrocapsa</i> (medium)	CN	1.67	1.67	11H-1, 75	91.25	11H-2, 75	92.75	1.67	0.00	92.00	100.40	0.75
LO <i>Rhizosolenia praebergonii</i> v. <i>robusta</i>	D	1.73	1.73	9H-2, 75	73.76	9H-3, 75	75.27	1.73	0.00	74.52	80.92	0.75
FO <i>Fragilariopsis doliolus</i>	D	2.00	2.00	11H-CC, 10	100.28	12H-1, 75	100.75	1.89	0.11	100.52	109.14	0.23
LO <i>Discoaster brouweri</i>	CN	1.96	1.96	11H-6, 75	98.78	11H-7, 40	99.93	1.96	0.00	99.36	107.76	0.58
FO <i>Pulleniatina finalis</i>	PF	2.04	2.04	9H-CC, 20	81.49	10H-CC, 33	91.05	2.04	0.00	86.27	93.05	4.78
LO <i>Globorotalia pseudomiocenic</i>	PF	2.30	2.30	10H-CC, 33	91.05	11H-CC, 10	100.28	2.30	0.00	95.67	103.44	4.62
LO <i>Thalassiosira convexa</i> s.l.	D	2.41	2.41	12H-2, 75	102.26	12H-3, 75	103.77	2.41	0.00	103.02	111.87	0.75
LO <i>Discoaster pentaradiatus</i>	CN	2.44	2.44	13H-3, 75	113.27	13H-4, 75	114.78	2.44	0.00	114.03	124.78	0.76
LO <i>Discoaster surculus</i>	CN	2.61	2.61	13H-5, 75	116.29	13H-6, 75	117.80	2.61	0.00	117.05	127.80	0.75
LO <i>Nitzschia jouseae</i>	D	2.77	2.77	14H-4, 75	124.28	14H-5, 75	125.78	2.77	0.00	125.03	136.98	0.75
FO <i>Rhizosolenia praebergonii</i> s.l.	D	3.17	3.17	18H-2, 75	159.25	18H-3, 75	160.76	3.17	0.00	160.01	176.51	0.75
LO <i>Globorotalia margaritae</i>	PF	3.58	3.58	15H-CC, 21	138.40	16H-CC, 20	148.00	3.58	0.00	143.20	157.13	4.80
LO <i>Pulleniatina primalis</i>	PF	3.65	3.65	16H-CC, 20	148.00	17H-CC, 25	157.44	3.65	0.00	152.72	167.70	4.72
LO <i>Reticulofenestra pseudoubilicus</i>	CN	3.80	3.80	20H-CC, 1	185.99	21H-CC, 1	195.26	3.80	0.00	190.63	209.09	4.63
FO <i>Thalassiosira convexa</i> v. <i>convexa</i>	D	3.81	3.81	22H-5, 75	201.80	22H-CC, 1	205.01	3.81	0.00	203.41	224.04	1.60
LO <i>Globorotalia margaritae</i> common	PF	3.96	3.96	16H-CC, 20	148.00	17H-CC, 25	157.44	3.96	0.00	152.72	167.70	4.72
FO <i>Globorotalia puncticulata</i>	PF	4.50	4.50	28X-CC, 37	258.81	29X-CC, 24	267.03	4.50	0.00	262.92	289.85	4.11
LO <i>Nitzschia cylindrica</i>	D	4.88	4.88	28X-3, 75	253.37	29X-3, 75	262.97	4.88	0.00	258.17	285.10	4.80
FO <i>Nitzschia jouseae</i>	D	5.12	5.12	29X-3, 75	262.97	30X-3, 75	272.67	5.12	0.00	267.82	295.70	4.85
LO <i>Thalassiosira miocenic</i>	D	5.84	5.84	33X-3, 75	301.67	34X-3, 75	311.27	5.84	0.00	306.47	338.15	4.80
LO <i>Nitzschia miocenic</i> s.s.	D	6.08	6.08	34X-6, 75	315.80	35X-1, 75	317.85	6.08	0.00	316.83	349.45	1.02
FO <i>Globorotalia margaritae</i>	PF	6.09	6.09	34X-CC, 31	317.33	35X-CC, 25	326.86	6.09	0.00	322.10	354.72	4.77
LO <i>Thalassiosira praeconvexa</i>	D	6.18	6.18	35X-CC, 25	326.86	36X-CC, 28	336.47	6.18	0.00	331.67	365.24	4.81
LO <i>Rosielia praepaleasea</i>	D	6.54	6.54	37X-CC, 18	345.99	38X-CC, 31	355.56	6.54	0.00	350.78	386.25	4.78
FO <i>Thalassiosira miocenic</i>	D	6.55	6.55	36X-CC, 28	336.47	37X-CC, 18	345.99	6.55	0.00	341.23	375.76	4.76
FO <i>Thalassiosira convexa</i> v. <i>aspinosa</i>	D	6.57	6.57	36X-CC, 28	336.47	38X-CC, 31	355.56	6.57	0.00	346.02	381.02	9.54
FO <i>Thalassiosira praeconvexa</i>	D	6.71	6.71	37X-CC, 18	345.99	38X-CC, 31	355.56	6.71	0.00	350.78	386.25	4.78
LO absence interval <i>Reticulofenestra pseudoubilicus</i> >7 μm	CN	6.80	6.80	38X-3, 75	349.67	38X-6, 75	354.20	6.80	0.00	351.94	387.89	2.26
FO <i>Nitzschia miocenic</i> s.l.	D	7.30	7.30	38X-CC, 31	355.56	39X-CC, 29	365.41	7.30	0.00	360.49	396.91	4.93

Table T9 (continued).

Datum	Source	Age (Ma)		Top sample (FO presence/LO absence)		Bottom sample (LO presence/FO absence)		Age (Ma)		Depth		
		Minimum	Maximum	Core, section, interval (cm)	Depth (mbsf)	Core, section, interval (cm)	Depth (mbsf)	Average	Uncertainty (±)	Average (mbsf)	Average (mcd)	Uncertainty (±m)
FO <i>Nitzschia reinholdii</i>	D	7.64	7.64	40X-3, 75	368.97	40X-CC, 1	375.00	7.64	0.00	371.99	409.69	3.01
LO <i>Actinocyclus ellipticus</i> v. <i>javanicus</i>	D	7.79	7.79	40X-CC, 30	375.00	41X-CC, 1	383.37	7.79	0.00	379.19	417.51	4.19
FO <i>Nitzschia cylindrica</i>	D	8.07	8.07	40X-5, 75	371.97	41X-CC, 1	383.37	8.07	0.00	377.67	416.00	5.70
FO Absence interval <i>Reticulofenestra pseudumbilicus</i> >7 µm	CN	8.85	8.85	41X-4, 75	380.16	41X-5, 75	381.67	8.85	0.00	380.92	419.72	0.75
LO <i>Coccolithus miopelagicus</i>	CN	10.40	10.40	45X-1, 75	414.05	45X-2, 75	415.55	10.40	0.00	414.80	456.45	0.75
LO <i>Globorotalia fohsi</i> s.l.	PF	11.68	11.68	41X-CC, 1	383.37	43X-CC, 24	397.69	11.68	0.00	390.53	429.81	7.16

Notes: FO = first occurrence, LO = last occurrence. CN = calcareous nannofossils, PF = planktonic foraminifers, D = diatoms.

Table T10. Distribution of calcareous nannofossils, Hole 1238A. (See table notes. Continued on next page.)

Core, section, interval (cm)	Depth (mbsf)	Depth (mcd)	Preservation	Abundance	<i>Amaurolithus primus/delicatus</i>	<i>Calcidiscus macintyreii</i>	<i>Ceratolithus</i> spp.	<i>Coccolithus miopelagicus</i>	<i>Discoaster bellus</i>	<i>Discoaster brouweri</i>	<i>Discoaster calcaris/neohamatus</i>	<i>Discoaster loeblichii</i>	<i>Discoaster neorectus</i>	<i>Discoaster pentaradiatus</i>	<i>Discoaster quinqueramus/berggrenii</i>	<i>Discoaster surculus</i>	<i>Discoaster tamalis</i>	<i>Discoaster variabilis</i> gr.	<i>Emiliana huxleyi</i>	<i>Gephyrocapsa</i> spp. (large)	<i>Gephyrocapsa</i> spp. (medium)	<i>Gephyrocapsa</i> spp. (small)	<i>Helicosphaera sellii</i>	<i>Pseudoemiliana lacunosa</i>	<i>Reticulolenestra asanoi</i>	<i>Reticulolenestra pseudoumbilicus</i> >7 µm	<i>Reticulolenestra</i> <7 µm	<i>Reticulolenestra rotaria</i>	<i>Reticulolenestra</i> (small)	<i>Sphenolithus abies/neoabies</i>	
202-1238A-1H-1, 0	0.00	0.00	G	A															F	C											
1H-2, 75	2.25	2.25	G	A															D	C	C										
1H-3, 75	3.75	3.75	G	VA															F	A	F										
1H-CC, 9	5.01	5.01	G	VA															R	F	A										
2H-2, 75	7.26	7.86	G	A															R	C	C										
2H-3, 75	8.77	9.37	G	A															R	C	D										
2H-4, 75	10.28	10.88	G	A															R	C	D										
2H-5, 75	11.79	12.39	G	A															R	C	D										
2H-6, 75	13.29	13.89	G	A															R	D											
2H-CC, 23	14.96	15.56	G	VA															A	A											
3H-CC, 14	24.01	25.86	G	VA															A	A											
4H-1, 75	24.75	30.05	G	A															C	A	A			F							
4H-2, 75	26.26	31.56	G	A															A	A			F								
4H-3, 70	27.72	33.02	G	A															A	A			F								
4H-CC, 17	33.54	38.84	G	A															A	A			F								
5H-CC, 19	43.44	48.24	G	A															A	A			F								
6H-1, 75	43.75	50.60	G	A															A	A			R								
6H-2, 75	45.26	52.11	G	A															A	A			R			F					
6H-4, 75	48.28	55.13	G	A															A	A			R			F					
6H-CC, 32	52.93	59.78	G	VA															A	A			R			F					
7H-2, 75	54.76	62.06	G	VA															A	A			R			F					
7H-4, 75	57.77	65.07	G	VA															A	A			R			F					
7H-5, 75	59.28	66.58	G	VA															A	A			R			F					
7H-6, 75	60.79	68.09	G	VA															A	A			R			F					
7H-CC, 0	61.65	68.95	G	VA															C	A			R			F					
8H-1, 75	62.75	70.75	G	VA															C	A			R			F					
8H-3, 75	65.77	73.77	G	VA															C	A			R			F					
8H-5, 75	68.79	76.79	G	VA															C	A			R			F					
8H-6, 75	70.30	78.30	G	VA															C	A			R			F					
8H-CC, 33	72.04	80.04	G	VA															C	A			R			F					
9H-1, 75	72.25	78.65	M	A															A	F			R			F					
9H-2, 70	73.71	80.11	M	A															A	F			R			F					
9H-3, 76	75.28	81.68	M	A															C				R			F					
9H-4, 75	76.79	83.19	M	A															F				R			F					
9H-CC, 20	81.49	87.89	M	A															F				R			F					
10H-CC, 33	91.05	98.20	M	A															F	A			R			F					
11H-1, 75	91.25	99.65	G	A						R									F	A			R			F					
11H-2, 75	92.75	101.15	G	C						R									F	C			R			F					
11H-3, 75	94.26	102.66	G	A						F									C	F			R			F					
11H-4, 75	95.77	104.17	G	A						F									C	F			R			F					
11H-5, 75	97.28	105.68	G	A						R									C	F			R			F					
11H-6, 75	98.78	107.18	G	C						R									C	F			R			F					
11H-7, 40	99.93	108.33	G	C						R									C	F			R			F					
11H-CC, 10	100.28	108.68	M	A						F									C	C			R			F					
12H-CC, 28	110.01	118.86	M	A						R									F				R			F					
13H-3, 75	113.27	124.02	M	A						F				R					F	A			R			F					
13H-4, 75	114.78	125.53	M	A						R									F	F			R			F					
13H-5, 75	116.29	127.04	G	A						R									F	F			R			F					
13H-6, 75	117.80	128.55	G	A						R				R					F	F			R			F					
13H-CC, 17	118.59	129.34	M	A						R									F				R			F					
14H-CC, 19	128.94	140.89	M	A						F													R			F					
15H-CC, 21	138.40	152.15	M	A						R													R			F					
16H-CC, 20	148.00	162.10	G	A																			R			F					
17H-CC, 25	157.44	173.29	G	A						F													R			F					
18H-4, 75	162.26	178.76	G	VA						R													R			F					
18H-5, 75	163.77	180.27	G	A						R				R									R			F					

Table T12 (continued).

Core, section, interval (cm)	Depth (mbsf)	Depth (mcd)	Identification	Method	Abundance	Preservation						Remarks
44X-1, 75	404.45	446.10	Toothpick	S	B							
44X-2, 75	405.96	447.61	Toothpick	S	B							
44X-3, 75	407.47	449.12	Toothpick	S	B							
44X-4, 75	408.98	450.63	Toothpick	S	B							
44X-5, 75	410.49	452.09	Toothpick	S	B							
44X-5, 69	410.43	452.63	Toothpick	S	B							
44X-CC, 36	413.49	455.14	PAL	S	B							
45X-1, 75	414.05	456.65	Toothpick	S	B							
45X-2, 75	415.55	458.15	Toothpick	S	B							
45X-3, 50	416.80	459.40	Toothpick	S	B							
45X-CC, 35	417.71	460.31	PAL	S	B							
46X-1, 75	423.65	467.20	Toothpick	S	B							
							<i>Actinocyclus ellipticus</i>					
							<i>Actinocyclus ellipticus</i> v. <i>lanceolata</i>					
							<i>Actinocyclus</i> spp.					
							<i>Actinoptychus senarius</i>					
							<i>Asteromphalus elegans</i>					
							<i>Asteromphalus</i> spp.					
							<i>Azpeitia nodulifer</i>					
							<i>Chaetoceros</i> spp. (resting spores)					
							<i>Coscinodiscus</i> spp.					
							<i>Diploneis bombus</i>					
							<i>Hemidiscus cuneiformis</i>					
							<i>Nitzschia cylindrica</i>					
							<i>Nitzschia marina</i>					
							<i>Nitzschia miocenica</i>					
							<i>Nitzschia porteri</i>					
							<i>Nitzschia reinholdii</i>					
							<i>Nitzschia fossilis</i>					
							<i>Nitzschia jouseae</i>					
							<i>Paralia sulcata</i>					
							<i>Pseudoeunotia doliolus</i>					
							<i>Rhizosolenia</i> spp.					
							<i>Rhizosolenia matuyama</i>					
							<i>Rhizosolenia praebergonii robusta</i>					
							<i>Rhizosolenia praebergonii</i>					
							<i>Roselia praepaleacea</i>					
							<i>Stephanopyxis</i> spp.					
							<i>Thalassionema nitzschioides</i>					
							<i>Thalassiosira</i> spp.					
							<i>Thalassiosira burckliana</i>					
							<i>Thalassiosira convexa</i>					
							<i>Thalassiosira convexa aspinosa</i>					
							<i>Thalassiosira miocenica</i>					
							<i>Thalassiosira oestrupii</i>					
							<i>Thalassiosira praeconvexa</i>					
							<i>Thalassiothrix</i>					

Notes: PAL = paleontology sample. S = smear slide. Abundance: VA = abundant, A = abundant, C = common, F = few, R = rare, T = trace, B = barren. Preservation: G = good, M = moderate, P = poor.

Table T13. Headspace gas concentrations and C_1/C_2 ratios in sediments, Hole 1238A.

Core, section, interval (cm)	Depth		C_1 (ppmv)	C_2 (ppmv)	$C_2=$ (ppmv)	C_1/C_2
	(mbsf)	(mcd)				
202-1238A-						
1H-3, 0-5	3.00	3.00	2.1	0.0	0.0	
2H-4, 0-5	9.53	10.13	6.3	0.0	0.0	
3H-4, 0-5	19.04	20.89	14.2	0.0	0.0	
4H-3, 0-5	27.02	32.32	20.1	0.0	0.0	
5H-4, 0-5	38.02	42.82	9.8	0.0	0.0	
6H-4, 0-5	47.53	54.38	24.5	0.0	0.0	
7H-4, 0-5	57.02	64.32	27.7	0.0	0.0	
8H-4, 0-5	66.53	74.53	41.1	0.8	0.0	51.4
9H-4, 0-5	76.04	82.44	43.9	1.0	0.0	43.9
10H-4, 0-5	85.53	92.68	44.7	1.1	0.0	40.6
11H-4, 0-5	95.02	103.42	40.1	0.9	0.0	44.6
12H-4, 0-5	104.53	113.38	57.0	1.4	0.0	40.7
13H-4, 0-5	114.03	124.78	48.8	1.2	0.0	40.7
14H-4, 0-5	123.53	135.48	44.0	1.1	0.0	40.0
15H-4, 0-5	133.02	146.77	58.8	1.5	0.0	39.2
16H-4, 0-5	142.55	156.65	44.7	1.2	0.0	37.2
17H-4, 0-5	152.01	167.86	69.4	2.0	0.0	34.7
18H-4, 0-5	161.51	178.01	96.7	2.9	0.0	33.3
19H-4, 0-5	171.03	188.93	60.5	1.7	0.0	35.6
20H-4, 0-5	180.53	198.68	74.9	2.2	0.0	34.1
21H-4, 0-5	190.04	208.99	76.4	2.3	0.0	33.2
22H-4, 0-5	199.53	220.28	44.2	1.3	0.0	34.0
23X-4, 0-5	209.01	230.71	49.4	1.4	0.0	35.3
24X-4, 0-5	215.91	238.56	46.5	1.3	0.0	35.8
25X-4, 0-5	225.36	248.96	28.9	0.9	0.0	32.1
26X-4, 0-5	234.81	259.36	56.9	1.5	0.0	37.9
27X-4, 0-5	244.52	270.02	44.1	1.4	0.0	31.5
28X-4, 0-5	254.12	280.57	41.4	1.2	0.0	34.5
29X-4, 0-5	263.72	291.12	46.9	1.3	0.0	36.1
30X-4, 0-5	273.43	301.78	46.7	1.8	0.0	25.9
31X-4, 0-5	283.03	312.33	54.8	1.4	0.0	39.1
32X-4, 0-5	292.72	322.97	45.1	1.4	0.0	32.2
33X-4, 0-5	302.42	333.62	45.4	1.5	0.0	30.3
34X-4, 0-5	312.03	344.18	37.2	1.4	0.0	26.6
35X-4, 0-5	321.62	354.72	24.2	0.6	0.0	40.3
36X-4, 0-5	331.23	365.28	26.4	0.6	0.0	44.0
37X-4, 0-5	340.82	375.82	20.4	0.0	0.0	
38X-4, 0-5	350.43	386.38	23.0	0.0	0.0	
39X-4, 0-5	360.12	397.02	25.7	0.6	0.0	42.8
40X-4, 0-5	369.72	407.57	15.2	0.0	0.0	
41X-4, 0-5	379.41	418.21	24.4	0.0	0.0	
43X-3, 0-5	396.61	436.36	10.2	1.3	3.4	7.8
44X-4, 0-5	408.23	448.93	8.7	0.0	0.0	
45X-3, 0-5	416.30	457.95	10.1	0.0	0.0	

Table T14. Interstitial water geochemical data, Hole 1238A.

Core, section, interval (cm)	Depth		pH	Alkalinity (mM)	Salinity	Cl ⁻ (mM)	Na ⁺ (mM)	SO ₄ ²⁻ (mM)	HPO ₄ ²⁻ (μM)	NH ₄ ⁺ (mM)	H ₂ SiO ₄ (μM)	Mn ²⁺ (μM)	Fe ²⁺ (μM)	Ca ²⁺ (mM)	Mg ²⁺ (mM)	B (μM)	Sr ²⁺ (μM)	Ba ²⁺ (μM)	Li ⁺ (μM)	K ⁺ (mM)	
	(mbsf)	(mcd)																			
202-1238A-																					
1H-2, 145-150	2.95	2.95	7.55	3.1	34.0	552	475	26.8	5.2	BDL	668	3.8	BDL	10.0	51.2	490	87	0.3	26	11.7	
2H-3, 145-150	9.47	10.07	7.53	6.2	34.0	560	480	23.3	16.0	0.7	751	5.5	1.7	8.8	51.7	488	100	0.4	24	11.4	
3H-3, 145-150	18.98	20.83	7.50	9.9	34.0	559	476	17.5	25.0	1.1	828	2.4	3.7	7.3	51.0	525	137	0.3	28	11.7	
4H-2, 145-150	26.96	32.26	7.51	12.6	34.0	567	490	17.1	19.0	1.8	872	1.1	1.1	6.4	49.9	566	182	0.4	33	11.3	
5H-3, 145-150	37.97	42.77	7.53	13.8	35.0	564	480	12.5	27.0	2.1	928	BDL	15.0	6.3	49.1	585	210	0.4	37	11.6	
6H-3, 145-150	47.47	54.32	7.19	14.8	34.0	564	484	12.0	78.0	2.5	1016	0.6	10.8	6.1	47.6	608	240	0.6	41	11.6	
7H-3, 145-150	56.96	64.26	7.14	15.9	35.0	564	484	10.5	17.0	3.0	955	BDL	11.9	6.3	46.6	617	268	0.5	44	11.0	
8H-3, 145-150	66.47	74.47	7.42	16.3	34.0	564	485	9.3	14.0	2.8	988	BDL	5.0	6.4	45.0	638	284	0.7	48	11.3	
9H-3, 145-150	75.97	82.37	7.44	17.2	34.0	565	487	9.2	12.0	2.9	1038	BDL	11.0	7.0	44.1	647	303	0.7	48	11.4	
10H-3, 145-150	85.47	92.62	7.37	17.5	34.0	570	491	8.3	16.0	2.9	1044	BDL	7.8	7.5	43.7	647	322	0.7	50	10.8	
11H-3, 145-150	94.96	103.36	7.33	16.6	34.0	565	484	8.0	9.3	3.0	1093	BDL	2.8	7.6	43.3	666	322	0.7	50	11.1	
12H-3, 145-150	104.47	113.32	7.34	15.7	34.0	567	490	8.1	8.5	2.9	1115	BDL	16.0	7.9	41.5	665	330	0.8	52	10.4	
13H-3, 145-150	113.97	124.72	7.24	16.4	34.0	566	489	9.6	8.1	3.0	1182	BDL	12.0	8.7	42.2	667	343	0.7	53	10.7	
14H-3, 145-150	123.47	135.42	7.25	15.8	34.0	564	487	9.4	6.8	2.9	1187	BDL	8.9	9.2	41.4	659	344	0.7	53	10.3	
15H-3, 145-150	132.96	146.71	7.26	15.5	34.0	567	492	9.3	5.2	3.1	1204	BDL	2.0	9.7	39.8	652	349	0.9	52	10.3	
16H-3, 145-150	142.48	156.58	7.34	15.4	34.0	564	483	8.1	5.2	2.9	1231	BDL	9.6	10.3	40.7	658	361	0.7	54	10.2	
17H-3, 145-150	151.96	167.81	7.28	14.0	34.0	568	490	9.4	4.4	3.4	1281	BDL	13.5	10.5	39.7	673	365	0.7	53	10.2	
18H-3, 145-150	161.46	177.96	7.25	12.3	33.0	562	484	9.8	3.0	2.9	1309	BDL	1.0	10.9	39.1	660	384	0.7	55	10.1	
19H-3, 145-150	170.97	188.87	6.89	12.3	33.0	570	492	9.3	3.0	2.8	1309	BDL	13.1	11.5	38.1	669	394	0.7	54	9.8	
20H-3, 145-150	180.47	198.62	6.86	12.0	33.0	563	485	9.7	3.0	2.8	1358	BDL	16.0	12.1	37.9	676	405	0.7	54	10.0	
21H-3, 145-150	189.98	208.93	6.85	11.1	33.0	564	486	9.7	3.0	3.0	1386	BDL	1.2	12.6	36.8	680	422	0.8	55	9.6	
22H-3, 145-150	199.47	220.22	6.87	11.8	34.0	564	484	8.8	3.0	3.2	1436	BDL	2.3	13.9	36.1	698	445	0.7	58	9.5	
24X-3, 145-150	215.86	238.51	7.09	11.4	34.0	566	485	8.8	2.0	2.9	1447	BDL	3.4	14.4	36.1	677	450	0.8	53	9.2	
26X-3, 145-150	234.76	259.31	7.16	10.9	34.0	564	487	10.6	2.0	2.8	1524	BDL	21.6	14.8	35.0	700	480	0.7	51	9.3	
28X-3, 145-150	254.07	280.52	7.12	10.2	34.0	563	478	7.9	2.0	2.8	1546	BDL	18.4	15.7	35.1	720	498	0.9	49	9.6	
30X-3, 145-150	273.37	301.72	6.90	8.8	34.0	565	481	7.0	2.0	2.9	1673	BDL	20.2	15.7	33.0	732	531	0.9	49	9.3	
32X-3, 145-150	292.67	322.92	6.85	9.7	34.0	558	482	9.1	2.0	3.2	1789	BDL	2.6	16.1	31.3	790	582	0.7	47	9.1	
34X-3, 145-150	311.97	344.12	6.91	8.9	34.0	558	482	9.7	2.0	3.2	1866	BDL	32.5	16.6	31.3	782	614	0.8	45	8.6	
36X-3, 145-150	331.17	365.22	6.90	8.1	33.0	556	481	9.6	BDL	3.1	1877	BDL	1.6	16.5	30.4	836	627	0.7	42	8.7	
38X-3, 140-150	350.32	386.27	7.19	6.9	33.0	553	480	10.7	BDL	3.0	1728	BDL	17.4	16.3	30.3	860	648	0.8	40	8.6	
40X-3, 140-150	369.62	407.47	7.35	5.5	33.0	551	473	7.2	BDL	2.8	1756	BDL	1.5	16.4	28.7	866	714	0.9	39	7.7	
43X-2, 90-100	396.51	436.26	7.23	2.7	32.0	548	471	3.2	BDL	3.0	944	1.0	21.5	18.8	20.8	1023	799	1.2	31	7.1	
45X-2, 140-150	416.20	457.85	7.37	2.3	32.0	544	468	5.3	BDL	2.4	845	BDL	21.6	18.9	22.4	998	759	1.1	32	6.2	

Note: BDL = below detection limit (HPO₄²⁻ = 1 μM, NH₄⁺ = 0.4 mM, Mn²⁺ = 0.01 μM, Fe²⁺ = 0.2 μM).

Table T15. Inorganic carbon, calcium carbonate, total carbon, total organic carbon, total nitrogen, and total sulfur analyses, and TOC/TN ratios, Hole 1238A. (See table note. Continued on next two pages.)

Core, section, interval (cm)	Depth		IC (wt%)	CaCO ₃ (wt%)	TC (wt%)	TOC (wt%)	TN (wt%)	TS (wt%)	TOC/TN (atomic)
	(mbsf)	(mcd)							
202-1238A-									
1H-1, 74-75	0.74	0.74	6.08	50.7	7.43	1.35	0.17	0.21	6.67
1H-2, 74-75	2.24	2.24	6.52	54.3					
1H-3, 74-75	3.74	3.74	5.08	42.3	6.57	1.49	0.19	0.37	6.83
2H-1, 74-75	5.74	6.34	5.32	44.3	6.37	1.05	0.14	0.23	6.34
2H-2, 74-75	7.25	7.85	5.68	47.3					
2H-3, 74-75	8.76	9.36	6.80	56.6	7.85	1.05	0.13	0.22	6.79
2H-4, 74-75	10.27	10.87	5.89	49.0					
2H-5, 74-75	11.78	12.38	5.99	49.9	7.03	1.04	0.15	0.31	5.99
2H-6, 74-75	13.28	13.88	5.46	45.5					
2H-7, 20-21	14.25	14.85	6.72	56.0					
3H-1, 74-75	15.24	17.09	6.60	55.0	7.71	1.11	0.12	0.52	7.88
3H-2, 74-75	16.76	18.61	6.18	51.5					
3H-3, 74-75	18.27	20.12	7.78	64.8	8.75	0.97	0.15	0.10	5.45
3H-4, 74-75	19.78	21.63	7.82	65.2					
3H-5, 74-75	21.29	23.14	6.89	57.4	7.81	0.92	0.12	0.39	6.86
3H-6, 74-75	22.79	24.64	7.17	59.7					
3H-7, 20-21	23.25	25.10	7.87	65.6					
4H-1, 74-75	24.74	30.04	6.87	57.2	7.53	0.66	0.09	0.17	5.95
4H-2, 74-75	26.25	31.55	6.36	53.0					
4H-3, 40-41	27.42	32.72	7.91	65.9	8.88	0.97	0.10	0.07	8.32
4H-4, 74-75	28.49	33.79	7.10	59.1					
4H-5, 74-75	30.00	35.30	6.51	54.2	7.31	0.80	0.12	0.30	5.82
4H-6, 74-75	31.51	36.81	6.72	56.0					
4H-7, 20-21	32.47	37.77	7.49	62.4					
5H-1, 74-75	34.24	39.04	6.08	50.6	7.11	1.03	0.12	0.27	7.32
5H-2, 74-75	35.75	40.55	7.63	63.6					
5H-3, 74-75	37.26	42.06	6.21	51.8	6.99	0.78	0.14	0.30	4.66
5H-4, 74-75	38.76	43.56	5.87	48.9					
5H-5, 74-75	40.27	45.07	7.63	63.6	8.60	0.97	0.15	0.25	5.69
5H-6, 74-75	41.77	46.57	7.19	59.9					
5H-7, 20-21	42.73	47.53	7.65	63.8					
6H-1, 74-75	43.74	50.59	7.95	66.3	8.69	0.74	0.14	0.27	4.41
6H-2, 74-75	45.25	52.10	8.26	68.8					
6H-3, 74-75	46.76	53.61	8.09	67.4	8.56	0.47	0.05	0.24	7.81
6H-4, 74-75	48.27	55.12	7.28	60.6					
6H-5, 74-75	49.78	56.63	7.91	65.9	8.52	0.61	0.14	0.12	3.81
6H-6, 74-75	51.29	58.14	7.37	61.4					
7H-1, 74-75	53.24	60.54	6.95	57.9	7.66	0.71	0.10	0.31	6.38
7H-2, 74-75	54.75	62.05	6.28	52.3					
7H-3, 74-75	56.25	63.55	6.26	52.1	7.18	0.92	0.15	0.22	5.37
7H-4, 74-75	57.76	65.06	6.62	55.2					
7H-5, 74-75	59.27	66.57	7.26	60.4	7.77	0.51	0.13	0.30	3.44
7H-6, 74-75	60.78	68.08	7.69	64.1					
7H-7, 20-21	61.25	68.55	7.33	61.1					
8H-1, 74-75	62.74	70.74	5.51	45.9	6.56	1.05	0.19	0.61	4.81
8H-2, 74-75	64.25	72.25	7.26	60.5					
8H-3, 74-75	65.76	73.76	6.48	53.9	7.85	1.37	0.16	0.61	7.55
8H-4, 74-75	67.27	75.27	7.63	63.6					
8H-5, 74-75	68.78	76.78	7.82	65.1	8.38	0.56	0.08		5.87
8H-6, 74-75	70.29	78.29	4.97	41.4					
9H-1, 74-75	72.24	78.64	5.95	49.5	7.60	1.65	0.19	0.73	7.49
9H-2, 74-75	73.75	80.15	4.32	36.0					
9H-3, 74-75	75.26	81.66	5.27	43.9	7.10	1.83	0.22	0.57	7.02
9H-4, 74-75	76.78	83.18	3.45	28.7					
9H-5, 74-75	78.29	84.69	4.09	34.0	8.34	4.25	0.41	1.40	8.82
9H-6, 74-75	79.80	86.20	3.22	26.8					
9H-7, 20-21	80.77	87.17	3.58	29.8					
10H-1, 74-75	81.74	88.89	4.98	41.5	7.31	2.33	0.26	0.79	7.61
10H-2, 74-75	83.25	90.40	5.82	48.5					
10H-3, 74-75	84.76	91.91	4.99	41.6	7.34	2.35	0.20	0.60	10.07
10H-4, 74-75	86.27	93.42	4.41	36.7					
10H-5, 74-75	87.77	94.92	3.01	25.1	5.28	2.27	0.20	0.62	9.72
10H-6, 74-75	89.28	96.43	6.80	56.6					
10H-7, 20-21	90.25	97.40	6.44	53.6					
11H-1, 74-75	91.24	99.64	2.09	17.4	3.08	0.99	0.10	0.31	8.66

Table T15 (continued).

Core, section, interval (cm)	Depth		IC (wt%)	CaCO ₃ (wt%)	TC (wt%)	TOC (wt%)	TN (wt%)	TS (wt%)	TOC/TN (atomic)
	(mbsf)	(mcd)							
11H-2, 74-75	92.74	101.14	3.53	29.4					
11H-3, 74-75	94.25	102.65	6.70	55.8	8.07	1.37	0.17		6.96
11H-4, 74-75	95.76	104.16	6.77	56.4					
11H-5, 74-75	97.27	105.67	7.60	63.3	8.49	0.89	0.14	0.43	5.29
11H-6, 74-75	98.77	107.17	6.95	57.9					
11H-7, 20-21	99.73	108.13	6.82	56.8					
12H-1, 74-75	100.74	109.59	4.57	37.8	6.03	1.46	0.11	0.44	11.38
12H-3, 74-75	103.76	112.61	5.02	41.7	7.12	2.10	0.18		10.13
12H-5, 74-75	106.78	115.63	7.61	63.4	8.64	1.03	0.11	0.40	8.27
13H-1, 74-75	110.24	120.99	7.57	63.1	8.28	0.71	0.13	0.39	4.60
13H-3, 74-75	113.26	124.01	7.58	63.2	8.29	0.71	0.15	0.31	4.11
13H-5, 74-75	116.28	127.03	5.50	45.8	6.81	1.31	0.18	0.54	6.15
14H-1, 74-75	119.74	131.69	7.45	62.1	8.13	0.68	0.09	0.22	6.76
14H-3, 74-75	122.76	134.71	6.60	55.0	7.75	1.15	0.12		8.53
14H-5, 74-75	125.77	137.72	6.44	53.6	7.43	0.99	0.15	0.33	5.64
15H-1, 74-75	129.24	142.99	4.81	40.1	5.97	1.16	0.12	0.33	8.36
15H-3, 74-75	132.25	146.00	5.84	48.6	7.05	1.21	0.17	0.63	5.98
15H-5, 74-75	135.27	149.02	5.84	48.7	6.95	1.11	0.16	0.19	5.80
16H-1, 74-75	138.74	152.84	5.60	46.7					
16H-3, 74-75	141.77	155.87	7.25	60.4	8.56	1.31	0.19	0.46	6.04
16H-5, 74-75	144.80	158.90	5.55	46.3	6.93	1.38	0.19		6.34
17H-1, 74-75	148.24	164.09	6.40	53.3					
17H-3, 74-75	151.25	167.10	6.75	56.3	7.79	1.04	0.11		8.13
17H-5, 74-75	154.25	170.10	6.18	51.5	7.31	1.13	0.15	0.26	6.61
18H-1, 74-75	157.74	174.24	5.33	44.4					
18H-3, 74-75	160.75	177.25	6.46	53.8	7.31	0.85	0.13		5.69
18H-5, 74-75	163.76	180.26	5.98	49.8	6.88	0.90	0.13		6.10
19H-1, 74-75	167.24	185.14	6.95	57.9					
19H-3, 74-75	170.26	188.16	6.82	56.8	7.88	1.06	0.15		6.27
19H-5, 74-75	173.28	191.18	7.14	59.4	8.09	0.95	0.16		4.97
20H-1, 74-75	176.74	194.89	8.08	67.3					
20H-3, 74-75	179.76	197.91	6.97	58.0	8.09	1.12	0.15		6.32
20H-5, 74-75	182.78	200.93	8.37	69.7	9.32	0.95	0.14		5.80
21H-1, 74-75	186.24	205.19	8.49	70.7					
21H-3, 74-75	189.27	208.22	8.36	69.6	9.09	0.73	0.15		4.07
21H-5, 74-75	192.29	211.24	8.19	68.2	8.74	0.55	0.07		6.47
21H-7, 20-21	194.78	213.73	8.52	71.0					
22H-1, 74-75	195.74	216.49	7.21	60.1					
22H-3, 74-75	198.76	219.51	7.08	58.9	7.69	0.61	0.07		7.33
22H-5, 74-75	201.79	222.54	6.09	50.7	6.84	0.75	0.08		8.13
23X-1, 74-75	205.24	226.94	5.23	43.6					
23X-3, 74-75	208.25	229.95	7.39	61.5	7.85	0.46	0.07		5.61
23X-5, 74-75	211.25	232.95	8.79	73.2	9.14	0.35	0.06		5.02
24X-1, 74-75	212.14	234.79	8.63	71.9					
24X-3, 74-75	215.15	237.80	7.96	66.3	8.74	0.77	0.16		4.10
24X-5, 74-75	218.15	240.80	8.56	71.3	9.19	0.63	0.08		6.92
25X-1, 74-75	221.74	245.34	7.34	61.1					
25X-3, 74-75	224.60	248.20	7.47	62.2	8.21	0.74	0.07		9.03
25X-5, 74-75	227.60	251.20	7.64	63.6	8.22	0.58	0.11		4.45
26X-1, 74-75	231.04	255.59	8.05	67.1					
26X-3, 74-75	234.05	258.60	8.01	66.7	8.74	0.73	0.09		7.24
26X-5, 74-75	237.06	261.61	8.52	71.0	9.10	0.58	0.06		7.84
27X-1, 74-75	240.74	266.24	7.54	62.8					
27X-3, 74-75	243.75	269.25	6.32	52.7	7.09	0.77	0.16		4.12
27X-5, 74-75	246.77	272.27	8.77	73.1	9.40	0.63	0.06		8.97
28X-1, 74-75	250.34	276.79	9.67	80.6					
28X-3, 74-75	253.36	279.81	5.82	48.5	7.19	1.37	0.19		6.28
28X-5, 74-75	256.37	282.82	9.38	78.2	10.35	0.97	0.08		10.28
29X-1, 74-75	259.94	287.34	8.49	70.7					
29X-3, 74-75	262.96	290.36	7.78	64.8	8.31	0.53	0.06		7.71
29X-5, 74-75	265.97	293.37	8.62	71.8	9.52	0.90	0.07		10.40
30X-1, 74-75	269.64	297.99	8.57	71.4					
30X-3, 74-75	272.66	301.01	8.61	71.8	9.41	0.80	0.07		9.91
30X-5, 74-75	275.68	304.03	8.43	70.2	9.19	0.76	0.07		8.79
31X-1, 74-75	279.24	308.54	7.72	64.3					
31X-3, 74-75	282.26	311.56	8.44	70.3					
31X-5, 74-75	285.28	314.58	9.17	76.4	9.86	0.69	0.06		10.12
32X-1, 74-75	288.94	319.19	9.32	77.6					
32X-3, 74-75	291.96	322.21	8.17	68.0	9.03	0.86	0.07		11.22

Table T15 (continued).

Core, section, interval (cm)	Depth		IC (wt%)	CaCO ₃ (wt%)	TC (wt%)	TOC (wt%)	TN (wt%)	TS (wt%)	TOC/TN (atomic)
	(mbsf)	(mcd)							
32X-5, 74-75	294.97	325.22	9.20	76.6	9.92	0.72	0.05		11.80
33X-1, 74-75	298.64	329.84	8.21	68.4					
33X-3, 74-75	301.66	332.86	9.55	79.5	10.02	0.47	0.04		11.50
33X-5, 74-75	304.67	335.87	8.90	74.1	9.83	0.92	0.08		10.01
34X-1, 74-75	308.24	340.39	8.98	74.8					
34X-3, 74-75	311.26	343.41	8.64	71.9	9.00	0.36			
34X-5, 74-75	314.28	346.43	7.99	66.5					
35X-1, 74-75	317.84	350.94	9.26	77.1					
35X-3, 74-75	320.86	353.96	7.55	62.9	7.90	0.35			
35X-5, 74-75	323.86	356.96	8.91	74.2					
36X-1, 74-75	327.44	361.49	6.75	56.2	7.06	0.31			
36X-3, 74-75	330.46	364.51	7.75	64.6	8.09	0.34			
36X-5, 74-75	333.48	367.53	8.02	66.8					
37X-1, 74-75	337.04	372.04	7.47	62.2	7.67	0.20	0.02		7.55
37X-3, 74-75	340.06	375.06	7.52	62.6	7.74	0.22			
37X-5, 74-75	343.07	378.07	9.16	76.3					
38X-1, 74-75	346.64	382.59	8.60	71.7					
38X-3, 74-75	349.66	385.61	9.40	78.3	9.52	0.12			
38X-5, 74-75	352.68	388.63	9.81	81.7					
39X-1, 74-75	356.34	393.24	9.75	81.2					
39X-3, 74-75	359.36	396.26	9.45	78.7	9.55	0.10			
39X-5, 74-75	362.37	399.27	9.58	79.8					
40X-1, 74-75	365.94	403.79	9.11	75.9					
40X-3, 74-75	368.96	406.81	7.72	64.3	8.08	0.36			
40X-5, 74-75	371.96	409.81	5.47	45.6	5.74	0.27	0.02		9.78
41X-1, 74-75	375.64	414.44	8.98	74.8					
41X-3, 74-75	378.65	417.45	10.19	84.9	10.28	0.09			
41X-5, 74-75	381.66	420.46	3.14	26.1	3.42	0.28	0.04		6.19
43X-1, 74-75	394.84	434.59	10.57	88.1					
43X-2, 74-75	396.35	436.10	10.97	91.4	11.03	0.05			
43X-3, 74-75	397.35	437.10	10.69	89.0					
44X-1, 74-75	404.44	445.14	11.09	92.4					
44X-3, 74-75	407.46	448.16	11.32	94.3	11.37	0.05			
44X-5, 74-75	410.48	451.18	3.82	31.9	3.90	0.08			
45X-1, 74-75	414.04	455.69	10.52	87.6					
45X-3, 74-75	417.04	458.69	10.59	88.2	10.75	0.16			
46X-1, 74-75	423.64	466.24	10.86	90.4					

Note: IC = inorganic carbon, TC = total carbon, TOC = total organic carbon, TN = total nitrogen, TS = total sulfur.

Table T16. Age-depth model, linear sedimentation rates, and mass accumulation rates, Site 1238.

Age (Ma)	Depth (mcd)	LSR (mcd/m.y.)	mcd growth factor	Corrected LSR (m/m.y.)	Dry density (g/cm ³)	CaCO ₃ average concentration (wt%)	TOC average concentration (wt%)	Total MAR (g/cm ² /k.y.)	CaCO ₃ MAR (g/cm ₂ /k.y.)	TOC MAR (g/cm ² /k.y.)	Noncarbonate MAR (g/cm ² /k.y.)
0.0	0.0										
1.0	57.0	57	1.10	52	0.67	57.1	0.44	3.4	2.0	0.015	1.5
2.0	103.9	47	1.10	43	0.60	46.8	0.71	2.6	1.2	0.018	1.4
3.0	149.3	45	1.10	41	0.60	53.9	0.89	2.5	1.3	0.022	1.1
4.0	227.9	79	1.10	71	0.70	57.2	0.60	5.0	2.9	0.030	2.1
5.0	301.0	73	1.10	66	0.78	67.4	0.49	5.2	3.5	0.026	1.7
6.0	358.9	58	1.10	53	0.83	72.1	0.32	4.4	3.2	0.014	1.2
7.0	396.6	38	1.10	34	0.91	70.9	0.12	3.1	2.2	0.004	0.9
8.0	415.2	19	1.10	17	0.98	68.1	0.13	1.7	1.1	0.002	0.5

Notes: LSR = linear sedimentation rate, MAR = mass accumulation rate. TOC = total organic carbon. This table is also available in [ASCII](#).